מכון ויצמן למדע
WEIZMANN INSTITUTE OF SCIENCE

Thesis for the degree
Master of Science

Submitted to the Scientific Council of the
Weizmann Institute of Science
Rehovot, Israel

עבודת גמר (תזה) לתואר
מוסמך למדעים

מוגשת למועצה המדעית של
מכון ויצמן למדע
רחובות, ישראל

By
Ilia Gutman

מאת
איליה גוטמן

דיכוי והגברת ההיסטרזיס בחומר מערבולות
Study of hysteresis suppression and enhancement in vortex matter

Advisor: Prof. Eli Zeldov

מנחה: פרופ' אלי זלדוב

February 2009

שבט ה'תשס"ט

Abstract

The discovery of high temperature superconductors (HTSC) in 1986 [1] renewed both extensive academic research and industrial commercial interest in superconductors. The HTSC materials are type II superconductors (SC), which within a certain range of applied magnetic fields and temperatures allow partial penetration of magnetic flux in the form of quantized vortices. These vortices carry magnetic moments which lead to repulsive interaction.

From an academic point of view Vortex Matter (VM) serves as an appealing physical system for fundamental many-body research, as it provides a remarkable example of a condensed matter state with parameters tunable over many orders of magnitude [2]. Some examples of tunable parameters are the following: Vortex density is simply controlled by the intensity of magnetic field, thermal fluctuations can be changed by varying the temperature, inhomogeneities and defects in the sample serve as pinning centers trapping vortices, in-plane fields in platelet crystals increase vortex concentration along 1D lines, and electrical current applies Lorentz force on the vortices.

From a practical point of view, if current along the HTSC is applied, motion of vortices perpendicular to the current produces energy dissipation and an effective resistance. The industrial interest in this research is in better understanding the forces acting on the vortices, thus succeeding to localize them and provide dissipationless current.

This work will deal with position dependent forces. While thermal fluctuations and inter-vortex repulsion will occur the same way in any place across the sample, pinning will depend on the exact location. The Meissner currents also gradually decrease towards the sample's center. Near sample edges there are two barriers for vortex penetration: elongation due to vortex line energy change, and the Bean-Livingston (B-L) surface barrier. All these location dependent forces will contribute to hysteresis in various regions of the temperature versus magnetic field (T-H) phase diagram.

In this work, these contributions and ways to suppress them will be studied mostly in $Bi_2Sr_2CaCu_2O_8$ crystals with magneto-optics techniques. In section 4.1 the geometrical barrier is discussed, and it is shown for the first time that mainly in-plane dc magnetic fields suppress hysteresis through geometrical barrier suppression. This provides an insight into the physics underlying the shaking method [3], which is extensively used to equilibrate VM.

In section 4.2 a region in the sample is patterned with a periodic surface hole matrix which gives rise to induced pinning. There is found to be a barrier for vortex penetration to the patterned region. This barrier has similar effect on vortices as the B-L surface barrier for vortex penetration into the sample.

In section 4.3 a novel system is tuned and tried, providing measurements of vortex penetration into the sample and hysteresis due to the pinning mechanism.

Acknowledgements

I would like to thank: my supervisor, Prof. Eli Zeldov, for guidance and advice, for his readiness to share his knowledge and physical intuition, and for the stimulating discussions which helped advancing the work,

Dr. Yuri Myasoedov for his assistance in high quality crystals preparation,

Sarah Goldberg for her help in studying experimental setups,

Yehonathan Segev for his help in working with Focused Ion Beam machine,

Dr. Michael Rappoport for his technical support in cryogenics and vacuum systems,

Prof. Ernst Helmut Brandt for providing theoretical insights about magneto-optics,

Dr. Satyajit Banerjee for constructive talk on current modulation,

Dr. Dan Oron and Prof. Ernesto Joselevich for consultation in the field of coherent systems noise,

and my colleagues Haim, Amit, Sarah, Yoni, Nurit, Tal for making the time in the lab so pleasant.

Contents

1. Introduction

To give a fairly intuitive understanding of the various vortex states, an explanation of the physical origin of vortices will first be given. Consider a flat crystal in the presence of an external magnetic field. Within the Ginzburg-Landau (G-L) theory, its free energy density can be expanded in powers of a complex nonlocal variable ψ, that serves as an order parameter [4].

$$f = f_{n0} + \alpha |\psi|^2 + \frac{\beta}{2}|\psi|^4 + \frac{1}{4m}|(\frac{\hbar}{i}\nabla - \frac{2e}{c}A)\psi|^2 + \frac{H^2}{8\pi} \qquad (1.1)$$

Here f_{n0} is the free energy of the normal state at zero magnetic field, α and β are parameters depending on the temperature and the material, and *m* and *e* are the mass and the charge of the electron respectively. A is the magnetic field vector potential, and H the external magnetic field. $|\psi|^2$ has a physical meaning as the superconducting electrons density.

Due to energy minimization principle, we minimize eq. 1.1 by variating it with respect to ψ. Integrating eq. 1.1 over the sample volume we obtain the free energy, and by minimizing it we get two G-L equations. The first equation allows the order parameter ψ to be calculated in the presence of the field, while the second gives the distribution of the current. The first equation is eq. 1.2.

$$\alpha\psi + \beta|\psi|^2\psi + \frac{1}{4m}(\frac{\hbar}{i}\nabla - \frac{2e}{c}A)^2\psi = 0 \qquad (1.2)$$

There are two homogeneous trivial solutions to equation (1.2):

1. Normal phase obeys $\psi = 0$ where A is determined only by

$$H = \nabla \times A$$

2. SC phase obeys $\psi = \psi_0 = \sqrt{-\alpha/\beta}$ and $H = A = 0$ (1.3).

In the normal phase, the magnetic field fully penetrates the sample and there are no superconducting electrons at all, while the SC phase is a phase of perfect diamagnetism which is also called the Meissner state. In this state, the field is completely expelled out of the sample and all the electrons are superconducting. The field lines of the two phases are shown in Fig. 1.1.

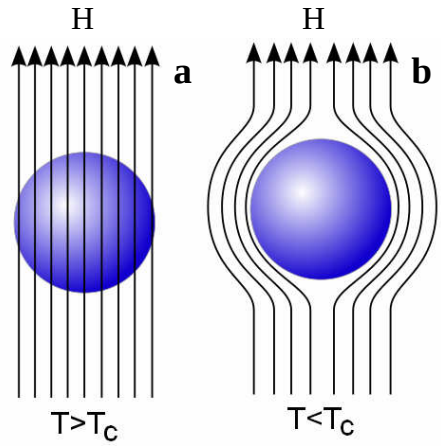

Fig. 1.1: Field lines are seen as black arrows. Superconducting sample marked as blue ball. (a) sample in normal phase. (b) sample in superconducting state

Consider now the superconducting and normal phases as boundary conditions. What will then be the field and density behavior at the interface?

G-L theory points out two different typical lengths for relaxation due to boundary conditions: one is the field relaxation scale λ called penetration depth and the second is the density relaxation length ξ called coherence length. For λ> ξ, the resulting field and order parameter behavior at the normal/SC interface is shown in Fig. 1.2. The inhomogeneous 1D solution for (1.2) is given by

$$\psi(x) = \sqrt{\frac{|\alpha|}{\beta}} \tanh\left(\frac{x}{\sqrt{2}\xi}\right) \qquad (1.4)$$

The interface domain energy is given by

$$\delta = \int_{-\infty}^{\infty} [(1 - \frac{h}{H_c})^2 - (\frac{\psi}{\psi_\infty})^4] dx \qquad (1.5)$$

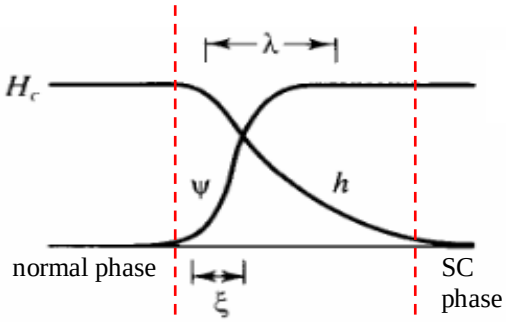

Fig. 1.2 Field and order parameter relaxation at an interface between superconducting and normal phases. Ref. 4.

Calculations show that for $\lambda / \xi > \sqrt{2}$, the domain wall energy becomes negative, making it favorable to have interface area as large as possible. This is done by dividing the sample into cylinders of normal phase parallel to the applied field surrounded by a superconducting phase. The division is continued until the quantum limit is reached (magnetic flux quantum). These cylinders are called Abrikosov vortices. Figure 1.3 presents Abrikosov vortices arrangement and structure.

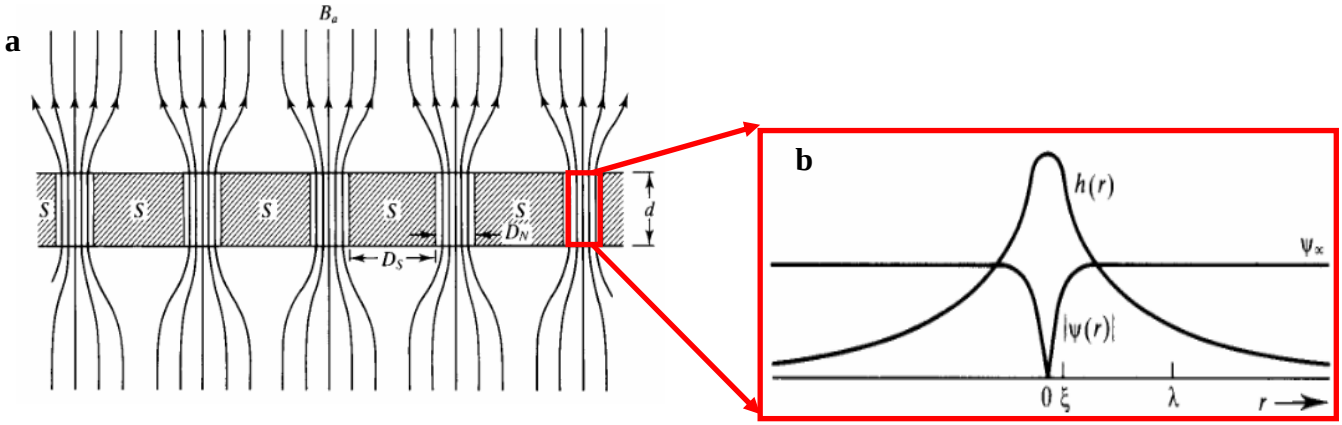

Fig. 1.3: Vortex structure in type II superconductor.
(a): Magnetic flux lines in mixed state. (b) Order parameter and magnetic field of a single vortex. Ref. 4.

Abrikosov vortices are vortices of supercurrent (current that consists of superconducting electrons), which according to Maxwell equations circulate around the region where field penetrates the normal (i.e. non-superconducting) core of each vortex. The core has a size of the coherence length ξ . The magnetic field (and also supercurrents) decays on the length scale λ from the center of the vortex. Each vortex has a total flux equal to a single flux quantum $\phi_0 = \frac{hc}{2e} = 2.07 \cdot 10^{-7} G \cdot cm^2$. These vortices are therefore called fluxons. Inside a vortex, the field penetrates the sample competely. Figure 1.4 is an image of local magnetic induction topography on Nb surface where Abrikosov vortices are visualized.

Thus, magnetic fields penetrate the sample in the form of cylinders which are Abrikosov vortices. Vortices do interact, and the interaction is repulsive [5]. It is similar to two magnets with the same

polarity which repel, as can be seen in Fig. 1.5. This repulsive interaction gives rise to a lattice arrangement as can be observed in Fig. 1.4. Raising the external magnetic field will raise the density of Abrikosov vortices proportionally, as the magnetic flux of each vortex is fixed.

Applying a current on the sample will activate a Lorentz force on the Abrikosov vortices and move them. The force is given by

$$\vec{F}_L = \vec{J} \times \frac{\hat{\phi}_0}{c} \qquad (1.6).$$

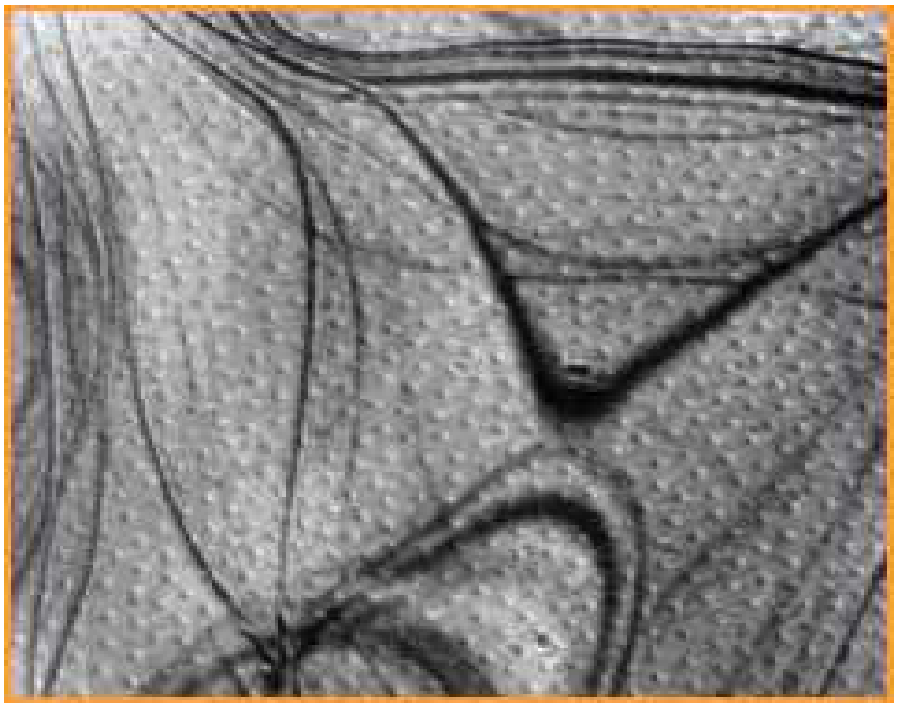

Fig. 1.4: Magnetic vortices in superconductors seen as magnetic field distribution peaks on surface according to Fig. 1.3 b. Image obtained by Lorentz microscopy on Nb films by Hitachi lab [6].

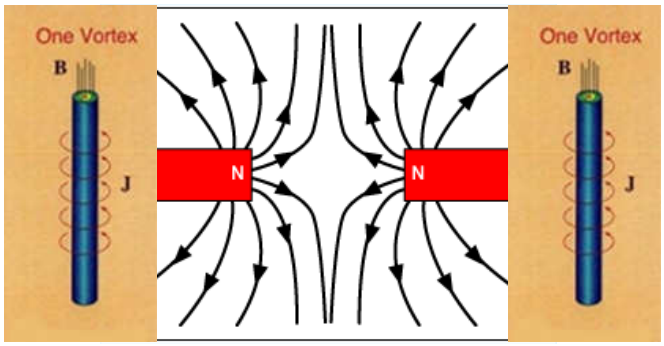

Fig. 1.5: Magnetic vortices repel each other similarly to two magnets.

2. Theoretical background

2.1 Layered superconductors

In 1986 Bednorz and Muller discovered the first HTSC [1]. Although its critical temperature was 35 K, this discovery is considered revolutionary, as it was one representative of a whole family of similar ceramic oxide materials, among them $Bi_2Sr_2CaCu_2O_8$ (BSCCO), that were found to be superconducting at elevated temperatures. Many of them are SC well above the liquefying temperature of Nitrogen. Common to all members of this family is a layered structure of Cu-O planes, separated by various metallic or insulating buffers, resulting in low ξ and high λ values, which make them extreme type II materials. It is mainly the Cu-O planes that are superconducting; therefore the superconducting state inherits the layered structure. These two-dimensional superconducting planes are coupled to each other through Josephson coupling.

Most of our measurements in present work will deal with the layered anisotropic material BSCCO. It is mainly the Cu-O planes that are superconducting and they are separated by insulating interfaces as can be seen in Fig. 2.1. Therefore the superconducting state inherits the layered structure. The layered structure introduces a distance between the superconducting planes *s* as a new length scale to the problem.

When a field perpendicular to the CuO_2 planes is applied, Abrikosov vortices will be formed. However a field in a direction parallel to the planes (in-plane field) will penetrate a layered superconductor also in a quantized manner, known as the Josephson vortex (JV). This vortex is of different physical nature; it resides in between two adjacent superconducting layers, saving the cost in condensation energy, as the order parameter ψ in the neighboring layers is only weekly perturbed. The profile of the screening supercurrents, associated with the JV, follows closely the continuous anisotropic case because $\lambda_{ab},\lambda_c >> s$, where *ab* denotes in-plane direction, and *c* axis denote the out of plane direction. Let

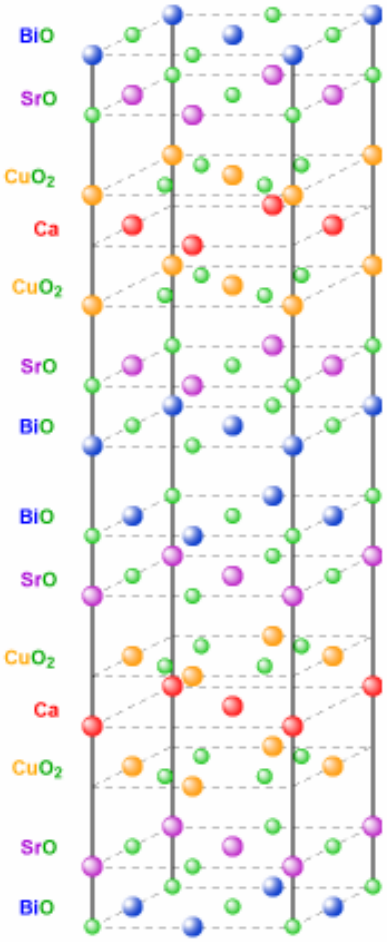

Fig. 2.1: Layered structure of $Bi_2Sr_2CaCu_2O_8$ crystal. CuO_2 planes separated by insulating planes

us define here the anisotropy $\gamma = \frac{\lambda_c}{\lambda_{ab}}$.

JVs create magnetic field with the total flux equal to ϕ_0, just like Abrikosov vortices. JV separation depends on the in-plane field in the following way [7,8] :

$$d_{ab} = \sqrt{\frac{\sqrt{3}\phi_0\gamma}{2H_x}} \qquad (2.1)$$

where γ is defined above. The out-of-plane distance between JV also scales with the in-plane field [7,8] and is given by

$$d_c = \sqrt{\frac{2\phi_0}{\sqrt{3}\gamma H_x}} \qquad (2.2).$$

When a magnetic field is applied perpendicular to the layers, the energy balance is distributed among the individual superconducting planes, where the screening supercurrents are restricted to flow. Once penetration of a quantum of magnetic flux into a single layer becomes favorable, the flux pierces through all layers, establishing a two-dimensional pancake vortex (PV) in each one. The PV has the same cross-sectional structure as an Abrikosov vortex (normal core of radius ξ_{ab} and magnetic flux decaying radially over λ_{ab}), therefore PVs, that reside in the same layer, inherit the mutual repulsion of the Abrikosov vortices, whereas PVs in adjacent layers are weakly coupled by magnetic [9] and Josephson [10,11] interactions. The magnetic interaction is just the usual interaction between two magnetic moments. The Josephson coupling originates from the energy that needs to be invested in establishing a JV to

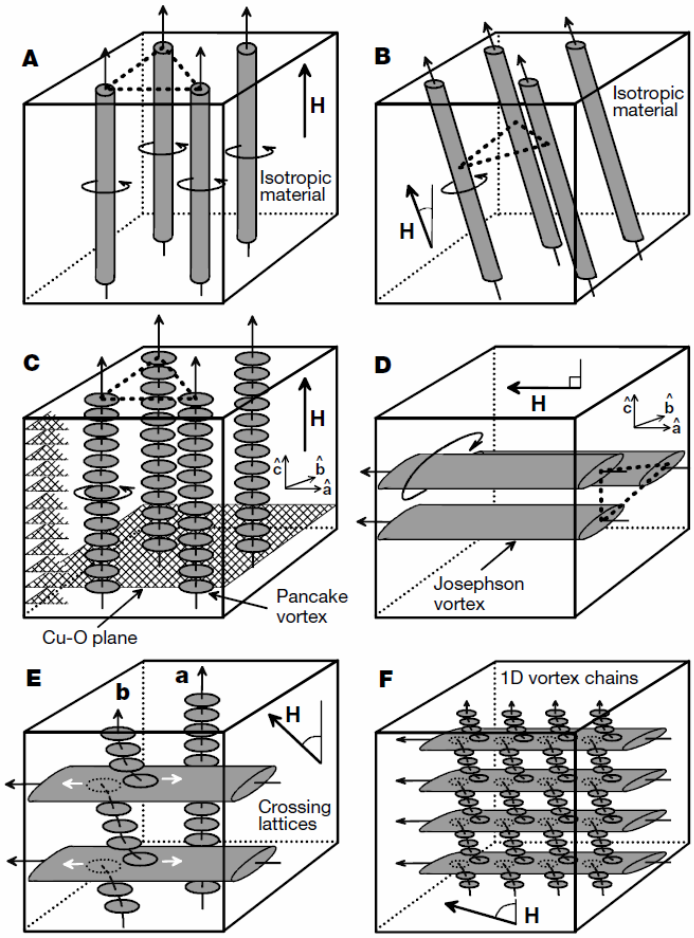

Fig. 2.2: Sketches of vortex structures in isotropic and layered superconductors. (A), (B), An isotropic superconductor where an ordered Abrikosov lattice is formed independent of the tilt angle. (C) C-axis field creates 2D pancake vortices situated in the Cu-O plane. (D) In-plane field form Josephson vortices whose cores reside in the spaces between Cu-O planes. (E) Crossing lattices state (a) If PVs and JVs do not intersect, no interaction occurs. (b) Where a PV stack intersects a JV stack, small PV displacements (indicated by white arrows) driven by the underlying JV supercurrents lead to an attractive interaction. (F) Zoomed-out view of the 1D vortex chain state when all PV stacks become trapped on vertical stacks of JVs. Sketches were taken from Ref. 39

redirect the magnetic flux between misaligned PVs. As a consequence PVs gather into aligned stacks along the c-axis to form a weakly coupled three-dimensional structure, while the repulsive interaction between the stacks leads to the formation of the PV lattice.

When both in-plane and perpendicular fields are applied, and in other words a field with some orientation to the sample is applied, both PV and JV will be formed. The reason is that in highly anisotropic materials such as BSCCO stacks of PVs do not follow the tilt of the external field away from the c-axis. In these materials the coupling between the PVs is predominantly magnetic, while an in-plane field interacts with PVs only through the Josephson coupling. Therefore, it is energetically favorable to respond independently to the c-axis and in-plane components of the tilted magnetic field [10] (up to corrections due to the weak Josephson interaction between the two), establishing the crossing lattices configuration [11-21], in which a weakly interacting c-axis PV lattice and in-plane JV lattice coexist. Crossing lattices state introduce a new ground state of VM, in which PVs are attracted by JVs, see Fig. 2.2. Among various arrangements of vortices in this state, 1D arrangements of ordered PVs, which are trapped and attached by underlying JV, are called vortex chains. The JV and thus also vortex chains separation scales with the in-plane magnetic field according to formula (2.7). Thus, measuring PV density, JV can be visualized by PV decoration.

2.2 Magnetic phases

The region in magnetic field (H) - temperature (T) phase diagram for which vortex creation is energetically favorable is called the mixed state. The qualitative behavior of the mixed state region in the T-H phase diagram is shown in Fig. 2.3. In fact, experimentally the mixed state of BSCCO has been shown to consist of at least three separate phases [22]. This will be discussed in detail in section 4.3.

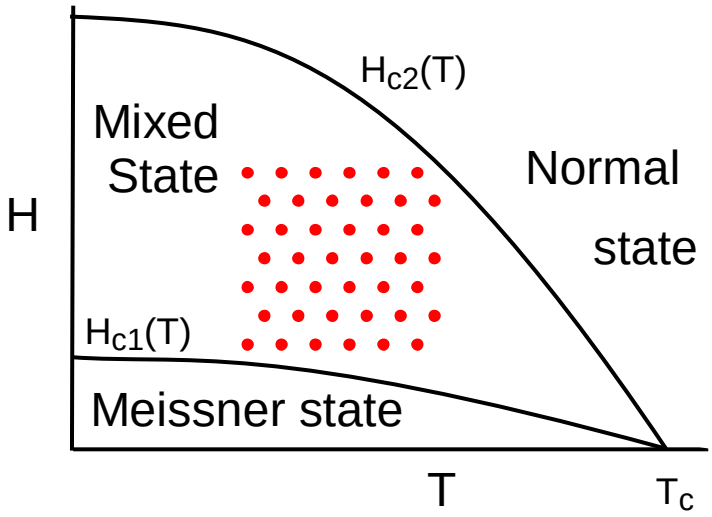

Fig. 2.3: Phase diagram of type II superconductor in field-temperature plane. The separating lines are called H_{c1} and H_{c2}.

The normal and Meissner states are described by homogeneous solutions of eq. (1.2) given in eq. (1.3) while the mixed state is the inhomogeneous solution given by eq. (1.4). Based on these equations, Fig. 2.4 presents the qualitative response of type II SC to applied magnetic field. Above H_{c2} B=H, while below H_{c1} B=0.

M is the magnetization, which is sample's response to the external field. It is given by

$$B = H + 4\pi M \Rightarrow -4\pi M = H - B \qquad (2.3)$$

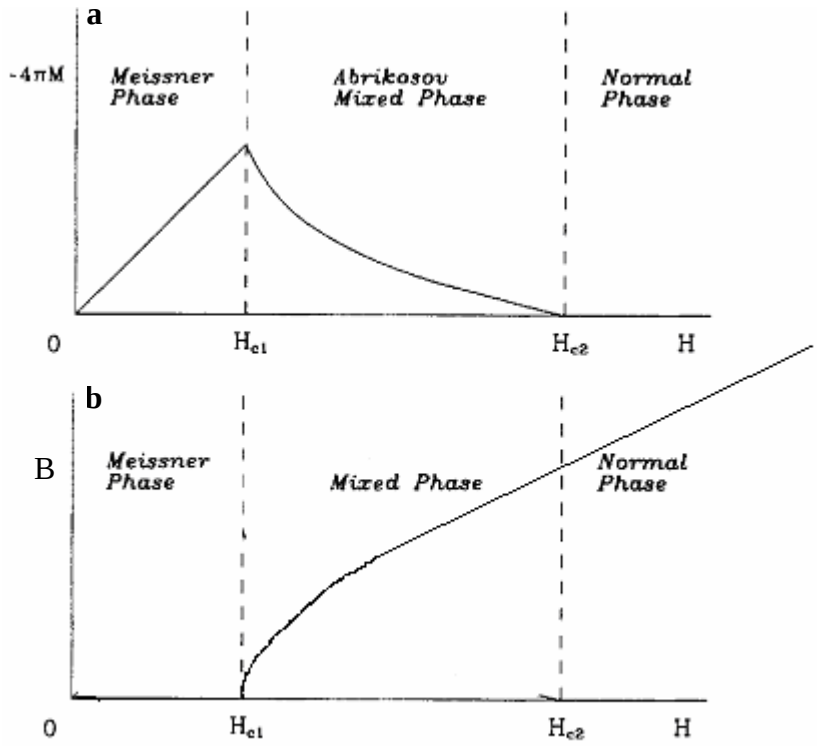

Fig. 2.4: Sample response to applied magnetic field. (a) Magnetization of the sample. (b) Total field penetrating the sample. Ref. 4.

However the real picture is a bit different: These curves may differ a lot depending on whether H is raised or lowered during the scan. This phenomenon is called hysteresis. This will be the subject of the next section.

2.3 Magnetic hysteresis

There are three main reasons for magnetic hysteresis:

1. Geometrical Barrier
2. Pinning (Bean model)
3. Bean-Livingston (B-L) Surface barrier

The B-L surface barrier [23,24] for vortex penetration is a result of barrier current, which can be represented as image anti-vortices outside the sample which attract the vortices inside the sample. The geometrical barrier [25-30] arises due to competition between the elongation energy of a vortex penetrating into the sample corners and the Lorentz force of Meissner currents. However, the usual source of hysteresis in superconductors is bulk vortex pinning due to material defects or inhomogeneties. However, in low pinning HTSC, all three mechanisms affect the vortex behavior, while in relatively dirty samples, pinning is the dominant factor. The present work will concentrate mainly on the first two reasons for hysteresis.

The differences between bulk and layered samples behavior under in-plane and perpendicular fields were discussed and shown in Fig. 2.2. Now two hysteresis models will be considered. The first is general for all type II superconductors, while the second holds only for the layered samples.

Section 2.3.1 considers an infinitely long platelet sample of width 2W and thickness d, where d<<W. A perpendicular geometry will be considered here, namely a field is applied perpendicular to the surface of the platelet. In absence of bulk pinning, the field penetration will be governed by geometrical barrier.

Section 2.3.2 will concentrate on Bean model of pinning in bulk isotropic superconductor of width 2W and infinite in the two other dimensions. A parallel geometry will be considered here, namely the applied field is parallel to the surface of the sample.

2.3.1 Geometrical Barrier

In a Meissner phase, Eq. 1.3 shows that the sample is perfectly diamagnetic. In order to screen the external flux, shielding currents are formed. They are called Meissner currents. A current distribution needed to screen homogeneous external field is maximal in the sample edges and minimal in the center of the sample. This can be seen in Fig. 2.5.

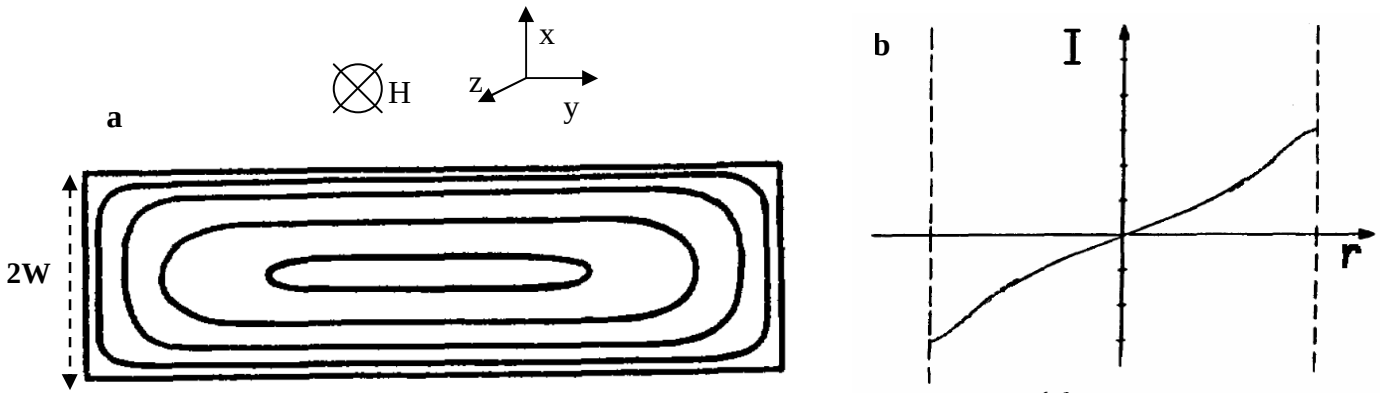

Fig. 2.5: In-plane current distribution in superconductor platelet of constant thickness with applied perpendicular external field. (a) 2D topographic view of current distribution. (b) Radial dependence of Meissner current. The images are taken from Ref. 31.

So, let us consider now a long strip geometry sample of width 2W and thickness d<<W in Meissner state. Because of the current distribution in Fig. 2.5b, it is favorable for vortices (if there have to be vortices) to be in the center of the sample where the Lorentz interaction energy between the vortex and the Meissner current is minimal. Vortices will start penetrating only when the vortex energy at the sample edges will vanish.

But even before vortices start penetrating into the bulk, they will penetrate into the sample edges as shown in Fig. 2.6. The reason for this is that on the edges there is a resisting force for vortex penetration due to vortex elongation energy.

Vortex energy is proportional to its length inside the sample (line energy). Vortices near the edges are curved cutting through the corners as can be seen in Fig. 2.6. So, vortices have reduced length inside the sample, and thus reduced energy. To minimize the elongation line energy, a force will expel vortices outside the sample, opposite to the force of Meissner currents, resulting in a balance which will leave the vortices in the sample edge. This energy balance will be calculated quantitatively in section 4.1.2. This force due to line energy stops acting when the two vortex segments merge at z=0, and this happens approximately when vortices reach the point x=W- d/2 for |z|=d/2 in Fig. 2.6. Thus, vortices will gradually fill the region from x=W to x=W-d/2. When x=W-d/2 is reached, it becomes energetically favorable for vortices to penetrate into the sample bulk. The field for vortex penetration is given by

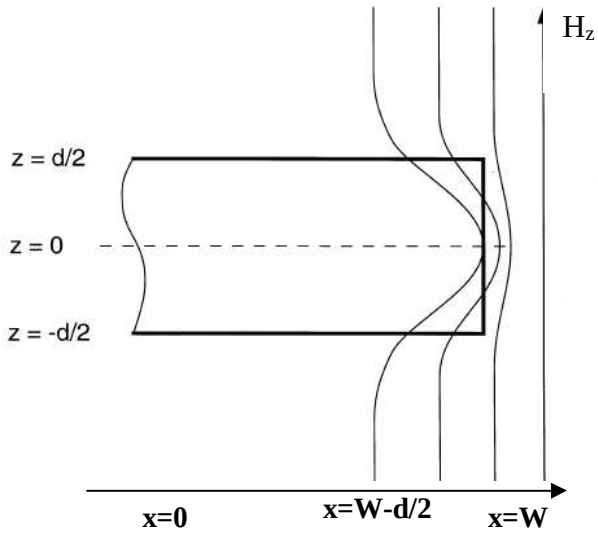

Fig. 2.6 Vortex penetration into the edge. The effect of sample edges on vortex line curvature. 2W is sample width and d is sample thickness. The image is taken from Ref. 27.

$$H_p = H_{c1}\sqrt{\frac{d}{W}} \qquad (2.4).$$

Applied field is denoted here H_z. For $H_z > H_p$, penetrated vortices are carried and focused by the surrounding Meissner currents towards the sample center, forming a droplet of vortices. Vortex distribution then has dome-like shape, where the maximum concentration is at the center x=0 according to the Meissner current density contour lines in Fig. 2.5. This distribution is called vortex dome, and it can be seen in Fig. 2.7 in the region 0<x<b where b is the vortex dome half width.

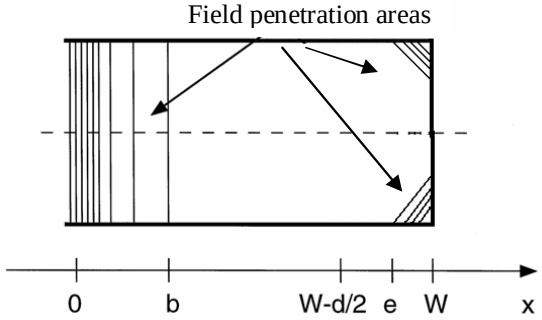

Fig. 2.7 Vortex distribution in the sample sample. b is the dome half width, and e is the coordinate of vortex penetration from the edges. 2W is sample width and d is sample thickness.

The half width of the dome increases with H_z until it reaches x=W-d/2. The functional dependence of this behavior is given by the following formula

$$H_z = \frac{2H_{c1}}{\pi} \ln \frac{\sqrt{W^2 - b^2} + \sqrt{W^2 - e^2}}{\sqrt{e^2 - b^2}} \qquad (2.5)$$

where b is the dome half-width and e is the coordinate of vortex filling of sample edge as in Fig. 2.12. *B(x)* inside the sample is described by the following equation:

$$B_z(x) = \frac{2H_{c1}}{\pi} \ln \frac{\sqrt{|e^2 - x^2|(W^2 - b^2)} + \sqrt{|b^2 - x^2|(W^2 - e^2)}}{\sqrt{(e^2 - b^2)|W^2 - x^2|}} \qquad |x|<b \text{ or } |x|>e$$

$$B_z(x) = 0 \qquad b<|x|<e \qquad (2.6)$$

And *J(x)* inside the sample is described by the following equation.

$$J(x) = 0 \qquad |x|<b,$$

$$J(x) = \pm \frac{2J_E}{\pi} \arctan \sqrt{\frac{(W^2 - e^2)(x^2 - b^2)}{(W^2 - b^2)(e^2 - x^2)}} \qquad b<|x|<e,$$

$$J(x) = \pm J_E \qquad e<|x|<W \qquad (2.7)$$

where $J_E = \frac{cH_{c1}}{2\pi d}$ [25] and c is the speed of light. Figure 2.8 presents a plot of Eqs. 2.6 and 2.7.

Thus on increasing H_z, for $0<H_z<H_p$, b=0 is constant and e grows from e=W to e=W-d/2 according to equation 2.5. For $H_z>H_p$, e=W-d/2 is constant and b grows from b=0 until b= W-d/2.

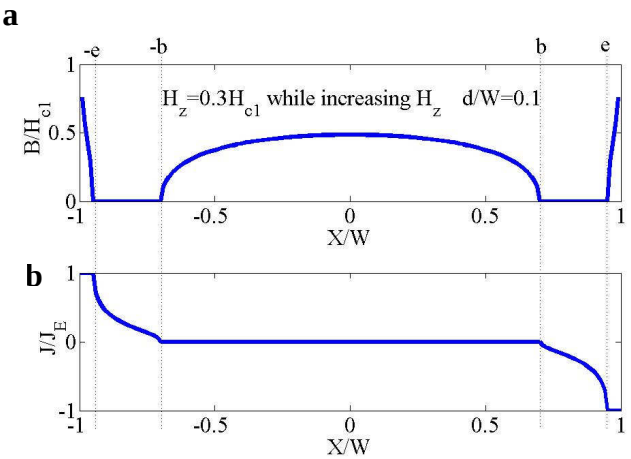

Fig. 2.8 Plot of (a) B(x) and (b) J(x) calculated from equations 2.6 and 2.7. b=0.7W and e=W-d/2=0.95W.

However on decreasing H_z, the situation is different. The vortex dome half-width b=W-d/2 remains constant and vortices leave the sample while the parameter e is determined by equation 2.5 by H_z. In all this process, B is determined completely by equation 2.6. Thus, the behavior of vortex dome is not reversible, and this contributes to the irreversibility of B.

Assume now that field H_z is increased till b<W-d/2 and then decreased. Vortices will be prevented from exiting the sample until b=W-d/2. Vortex dome expands to a maximum allowed value b=W-d/2 and only then vortices begin to leave the sample. While vortex droplet expands on decreasing field, constant flux is kept as no vortices leave the droplet. Along the red arrows, Fig. 2.9 shows the path in the e-b plane while making the magnetization loop. Along the red arrows in Fig.

2.9, H_{c1}=40 Oe is taken, and H_z is increased to 15 Oe. While sweeping H_z down, the dependence of b-e follows the constant flux contour marked by yellow color in Fig. 2.9a, while Fig. 2.9b indicates that H_z is indeed lowered. When the vortex dome half-width reaches b=W-d/2, flux starts to escape as seen in Fig. 2.9a. All flux exits when H_z=0 is reached and at this point e=W.

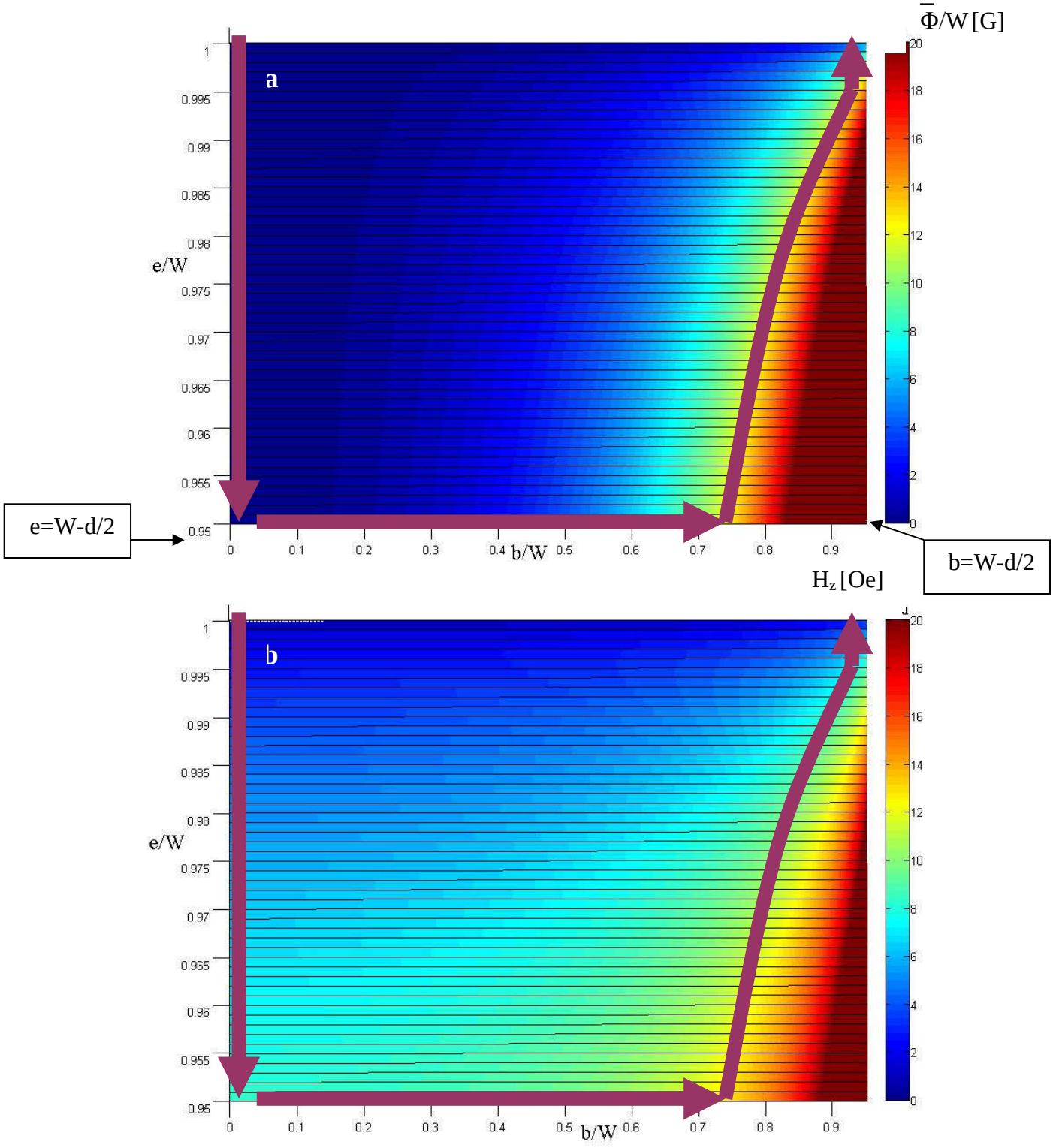

Fig. 2.9: Theoretical charts of (a) flux per unit length of the strip $\overline{\Phi} = \int_{-b}^{b} B(x)dx$ and (b) H_z as function of b and e. d/W=0.1 and H_{c1}=40 Oe. The red arrows show typical path in e-b plane of vortex dome while increasing and decreasing H_z.

2.3.2 Pinning - Bean model

In every natural material, there is a certain concentration of inhomogeneties and defects. Disorder in the sample is brought about by inevitable structural and chemical imperfections in the crystal. Superconductivity is locally weakened at the defects sites, making them energetically favorable positions for vortices. Disorder acts as pinning centers for vortices, creating potential walls [32]. The dynamic behavior of the vortices in the presence of bulk pinning can be qualitatively understood by the Bean critical model [33], in which point pinning is averaged into a spatially uniform pinning force.

An impurity serves as a potential wall that the vortex needs to overcome in order to leave it. The attraction potential is approximately harmonic, as can be seen in Fig. 2.10. Current in the sample applies Lorentz force on the vortices. As long as the vortices stay pinned by the pinning centers, their motion is prevented and the current remains pure superconducting. If a current is high enough, it will overcome the pinning force, thus moving the vortices across the sample and resulting in a non-zero resistivity.

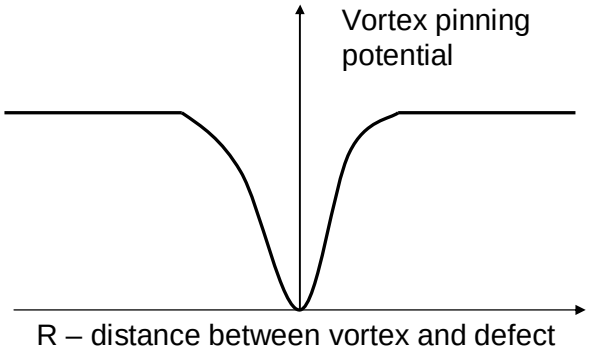

Fig. 2.10 Potential well for vortex pinning

The pinning forces are, therefore, limited and there exists a critical current density J_c and it is determined by the balance between pinning force and Lorenz force. At currents lower than the critical current there is no vortex motion and hence no voltage drop across the superconductor. Thus the pinning force is quantified by J_c. This means that if an external magnetic field is applied, the field inside the sample will be given by a Maxwell equation of the form:

$$\nabla \times B = \frac{4\pi}{c} J_c \tag{2.7}$$

with appropriate boundary conditions. Taking an infinite sample in the y-z planes, will reduce Eq. 2.7 to a 1D equation of the form

$$\frac{dB}{dx} = \pm \frac{4\pi}{c} J_c \tag{2.8}$$

where the signs depend on the field sweep history.

Let us assume that J_c does not depend on B or H_z, and a sample width is 2W (in the x direction). Then, a spatially uniform gradient of magnetic induction in the bulk is obtained, instead of a constant magnetic induction in the equilibrium case. Rising H_z will start flux entrance with

constant derivatives and boundary values $B(x = \pm W) = H_z, B(x = v) = 0$ where v is the penetrated depth. When v reaches 0, there will be a triangular shape of flux distribution. This will happen, according to Eq. 2.8, for

$$H_s = \frac{4\pi J_c W}{c} \tag{2.9}$$

which is the maximum applied field that can be screened out at the midplane x=0 of the sample. However, on the decreasing field, the sign of the derivative in Eq. 2.8 will change. Vortices will start to exit from the sides with the flux in the center remaining the same. This solution can be seen qualitatively in Fig. 2.11.

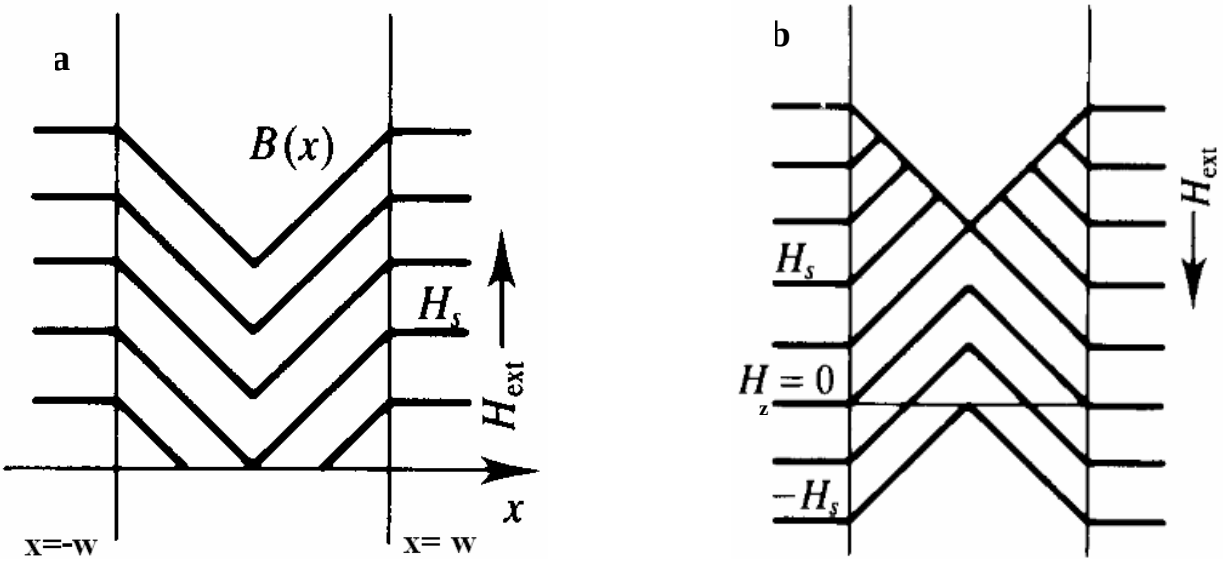

Fig. 2.11: Magnetic profile across the sample for different external fields. (a) While sweeping external field up. (b) While sweeping external field down. H_s is the maximum applied field that can be screened out at the midplane x=0. Ref. 4.

Bean model describes the hysteretic behavior, where changes in the externally applied field can propagate into the bulk only along these critical gradients. As before, here the flux is trapped again, but this time due to a different physical origin. A very substantial amount of flux may be left trapped in the slab even after H_z=0. As is evident from Fig. 2.11, there is much hysteresis and associated irreversibility in this cycling of field. For example, if the external field is cycled through a

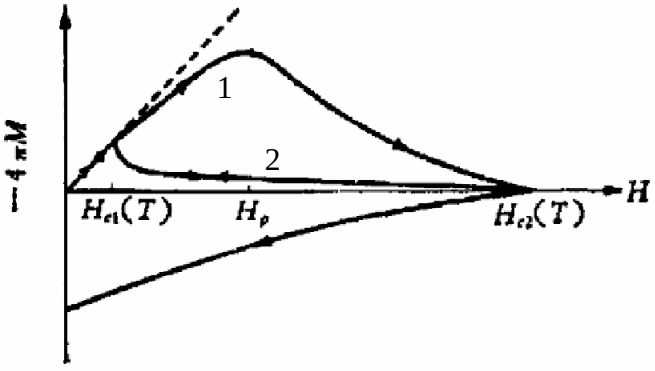

Fig. 2.12: Superconductor with and without hysteresis. Curve 1 without hysteresis is the equilibrium magnetization as in Fig. 2.4. Hysteretic superconductor has the magnetization behavior described by curve 2. Ref. 4.

maximum field $H_m<H_s$, one can see that the area inside the hysteresis loop $\oint BdH$ (and hence the energy Q dissipated as heat per cycle) will increase as H_m^3. On the other hand, if $H_m>>H_s$, then $Q \prec H_m$.

The switch in derivative sign is the hysteresis source, and the reason for the switch is the pinning force which, as every dissipative force, is an irreversible force. The resulting effect of these irreversible mechanisms on magnetization loop measurement can be seen in Fig. 2.12. Magnetization behavior while sweeping H up or down is qualitatively different.

3. Experimental setup

3.1 Principles of conventional Magneto-Optical system

The standard magneto-optical (MO) setup is shown in Fig. 3.1. MO measurements utilize magneto-optical garnet indicators (MOIs). Due to a large Faraday rotation, magnetic induction translates into a rotation of the polarization of the light upon passing through the MOI. Such an indicator is placed on top of the superconducting sample, with the mirror immediately above the sample, or with no mirror on it when the sample is a good reflector. Incident polarized light passes through the indicator, is reflected, and then passes through an analyzer with polarization axis at 90 degrees to the polarization of the incident light. The 2D magnetic field distribution across the sample's surface is translated into an intensity image by the formula

$$I(x,y) = I_0 \sin^2 \theta_F(x,y). \quad (3.1)$$

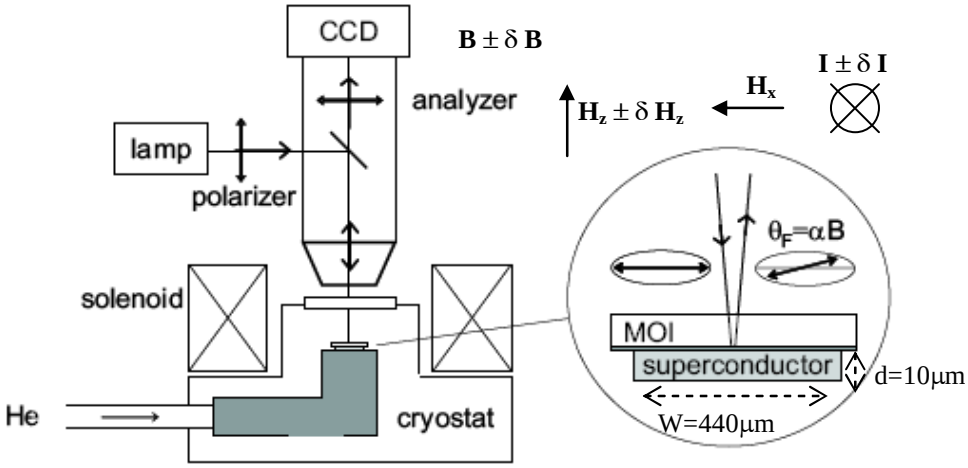

Figure 3.1: The differential magneto-optical (DMO) setup. The enlarged region shows the magneto optical indicator (in white), with mirror (dark grey) adjacent to the sample (light grey). The polarization of reflected light is rotated by angle $\theta_F(x,y) = V \cdot B(x,y)$, where B is the local magnetic induction. The geometry of experiment is also shown. Sample dimensions are written. Current flow and magnetic fields directions are shown.

Here I_0 is the intensity when the polarizer and analyzer axes are aligned, $\theta_F(x,y) = V \cdot B(x,y)$ is the Faraday rotation due to the local magnetic induction and V is the Verdet's constant of the MOI. As the light source here, Hg lamp is used.

To improve the resolution of the magnetic distribution picture, a differential technique was applied. This means changing one of the parameters in the system by a small amount, and subtracting the measured picture from the picture before the change. This gives improvement in picture resolution by several orders of magnitude. The conventional approach is to make modulation by changing H_z or T [34].

Au contacts were evaporated on a BSCCO crystal, and instead of modulating H_z or T, a transport current with periodically alternating polarity was applied to the sample and a

corresponding differential image was acquired and integrated, typically over a hundred cycles. As a result, the self-induced magnetic field generated by the transport current according to the Biot-Savart law can be measured to a very high precision. In section 4, I and H_z modulation is compared showing the supremacy of the first.

Differential MO (DMO) measurements were performed by modulating the current I by dI=60mA. $B(dI/2)-B(-dI/2)$ was measured upon increasing and decreasing H_z at constant temperature T=82 K and constant dc in-plane field H_x. The geometry of the experiment can be seen in the Fig. 3.1 inset. Using a typical camera exposure time of 0.5 sec, each measurement point required averaging over *8* CCD camera exposures, first at $+dI/2$ and then at $-dI/2$, and calculating a difference image. Each final DMO image is the average of *80* such difference images.

3.2 Novel Bragg Magneto-Optical system

Few experiments were done measuring the Long Range Order (LRO) of the VM, which is a good probe of the various phases of VM. The main tool to visualize LRO is by diffraction, and this work presents a novel attempt to make optical diffraction from vortices with a system which was called Bragg Magneto-Optics (Bragg-MO), shown schematically in Fig. 3.2.

In the Bragg-MO system, the main interest lies in the first-order structure of the light reflected off the mirror at the bottom of the MOI. The incident light must therefore be coherent. Thus instead of using an Hg lamp, here a laser with λ=532nm (green) is used. In addition, the image of interest is not the real-space MO image of the sample, but instead the Fourier-space image. This means that the physical location that must be imaged is not the sample itself, but rather the location within the setup that images Fourier-space - namely, the back focal plane of the lens placed closest to the sample. For imaging Fourier-space, the MOI is placed as close as possible to the sample. Coherent polarized light is reflected off the mirror of

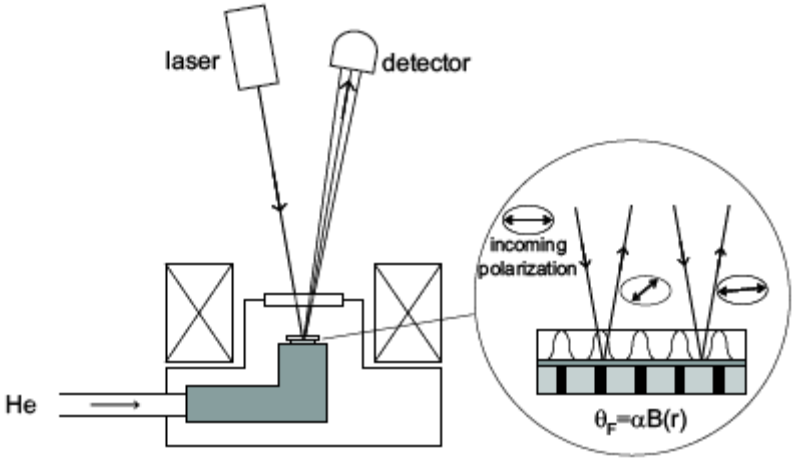

Figure 3.2: The Bragg Magneto-Optics setup. The enlarged region shows vortices (black columns) in the superconducting sample (light grey). The polarization axis is rotated more for light that is reflected above a vortex (left ray) than for light reflected between vortices (right ray). For a periodic vortex lattice, this produces a periodic modulation of polarization, shown schematically in the Magneto Optical Indicator (white region). The maxima of the resulting diffraction pattern (see Eq. 3.2) are measured by the detector (orders p = 0,1,-1 are shown schematically).

the indicator or the sample. The magnetic flux quanta associated with vortices produces local, quasi-periodic maxima in the Faraday rotation of the reflected light. This leads to a diffraction pattern, which for a lattice with ideal periodicity follows Bragg's condition

$$\theta_r - \theta_i = n\frac{\lambda}{a_0} \qquad (3.2)$$

where θ_i and θ_r are the incoming and outgoing angles of the light, respectively, λ is the wavelength of the light, a_0 is the period of the lattice, and n is the diffraction order.

In Fig. 3.3 the difference between conventional MO and Bragg-MO can be seen. In conventional MO we collect the scattered light, while in Bragg-MO we collect diffracted plane waves.

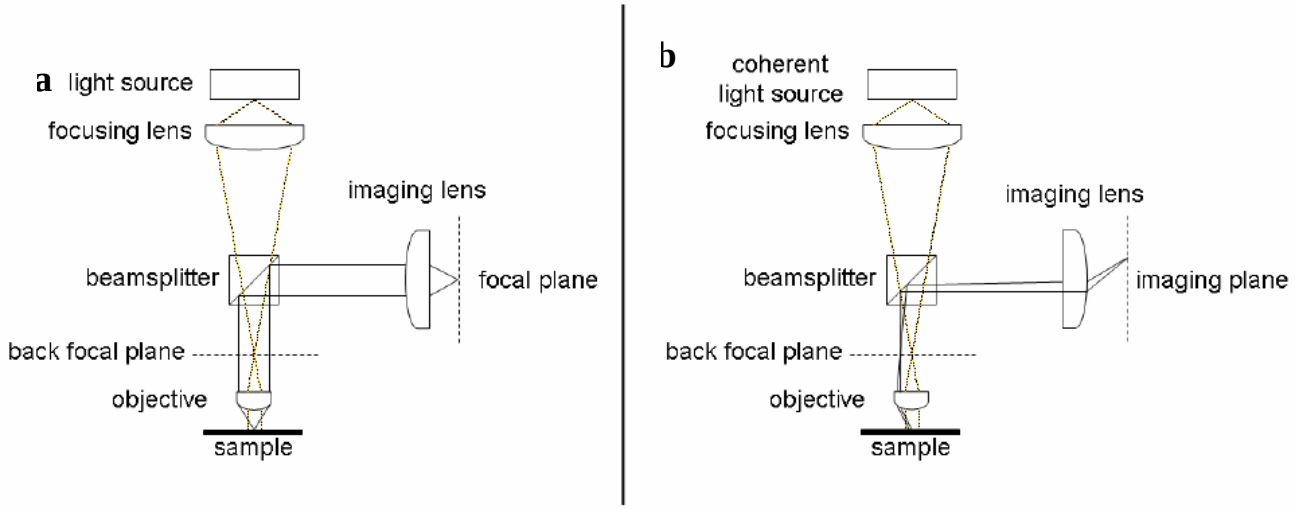

Fig. 3.3: Comparison between conventional Magneto-Optical and Bragg Magneto-Optical systems. In both cases the incoming light (yellow) is focused by a focusing lens to the back focal plane of the objective, and is incident on the sample as a plane wave. The reflected light (black) for real-space imaging (a) is a multi-point source. It is transformed into plane waves by the objective. The sample's image is located on the focal plane of the imaging lens. For imaging of Fourier space (b), the diffracted or plane-wave part of the reflected light is measured. These plane waves are focused to a point on the back focal plane of the objective. This plane is imaged on the imaging plane using the imaging lens.

In this work the main focus of performed measurements is on the zero-order of the Fourier image. Higher diffraction orders from $NbSe_2$ or BSCCO crystals haven't been detected yet. The reason is the large noise the system produces. The main reason for this noise is diffraction rings called also "fringes", formed by diffraction of different optical items in the system. The diffraction signal from Abrikosov vortices is very weak, and in order to observe it all these fringes should be eliminated.

4. Results and discussion

4.1 Conventional magneto-optical measurements

4.1.1 Comparison of vortex dome behavior to theory

Here, an attempt to verify experimentally the geometrical barrier model [25] discussed in section 2 is presented. Experimental verification was done partly by N. Morozov in references 26,27. Here it is done more fully showing one-to-one agreement with the model of vortex dome (vortex filled region) with no in-plane field. To distinguish in-plane and perpendicular fields, let us denote here H_a by H_z, in contrast with the in-plane field called H_x. Let us turn first to experiment.

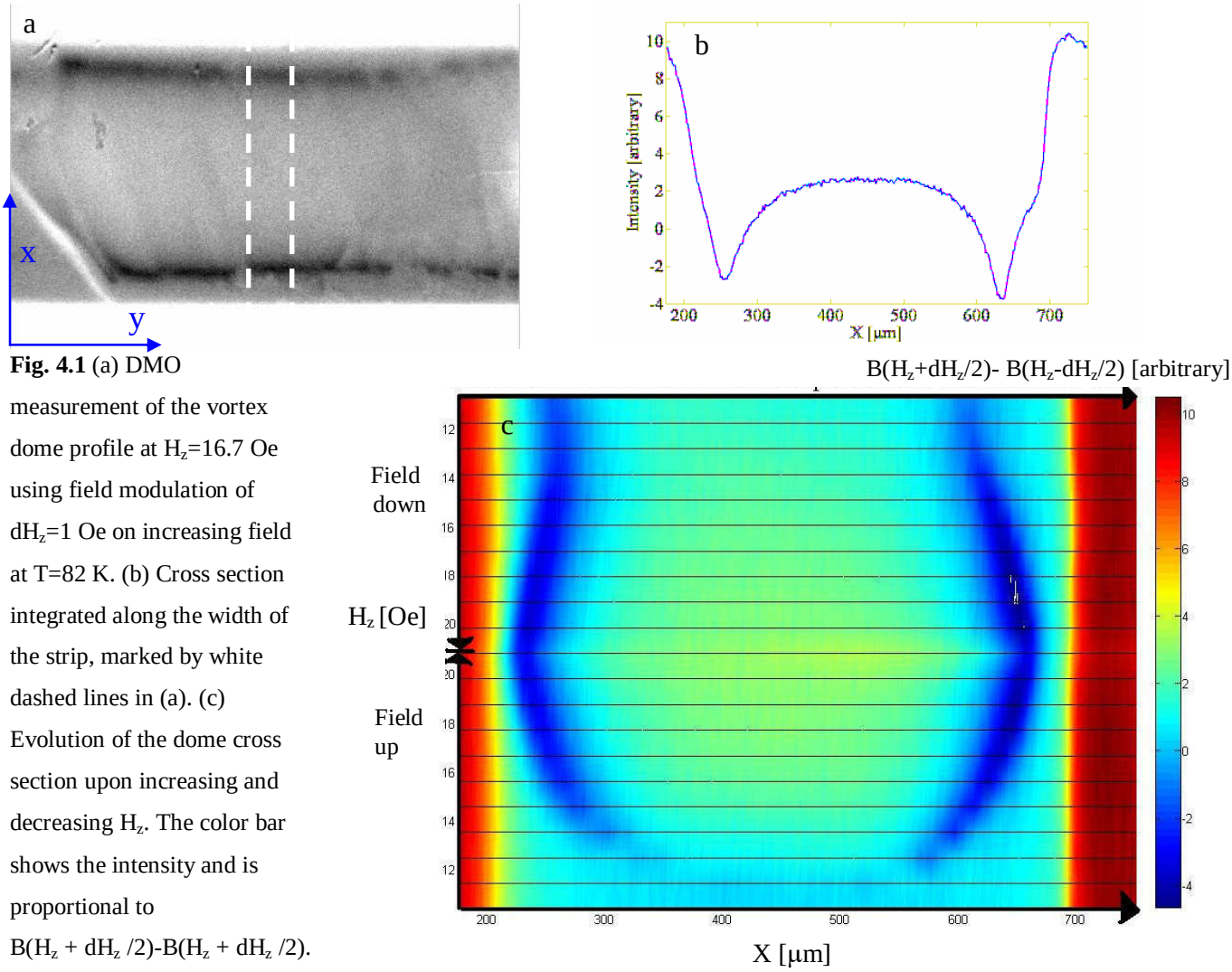

Fig. 4.1 (a) DMO measurement of the vortex dome profile at H_z=16.7 Oe using field modulation of dH_z=1 Oe on increasing field at T=82 K. (b) Cross section integrated along the width of the strip, marked by white dashed lines in (a). (c) Evolution of the dome cross section upon increasing and decreasing H_z. The color bar shows the intensity and is proportional to $B(H_z + dH_z/2)-B(H_z + dH_z/2)$. Blue strips are the dome edges. Yellow regions are sample edges. Red is outside the sample.

Figure 4.1 presents differential MO measurement using field modulation of dH_z=1 Oe. Dome edges are seen as blue regions in Fig. 4.1c. Figure 4.2 shows location of the dome edges upon increasing and decreasing field obtained from the data in Fig. 4.1.

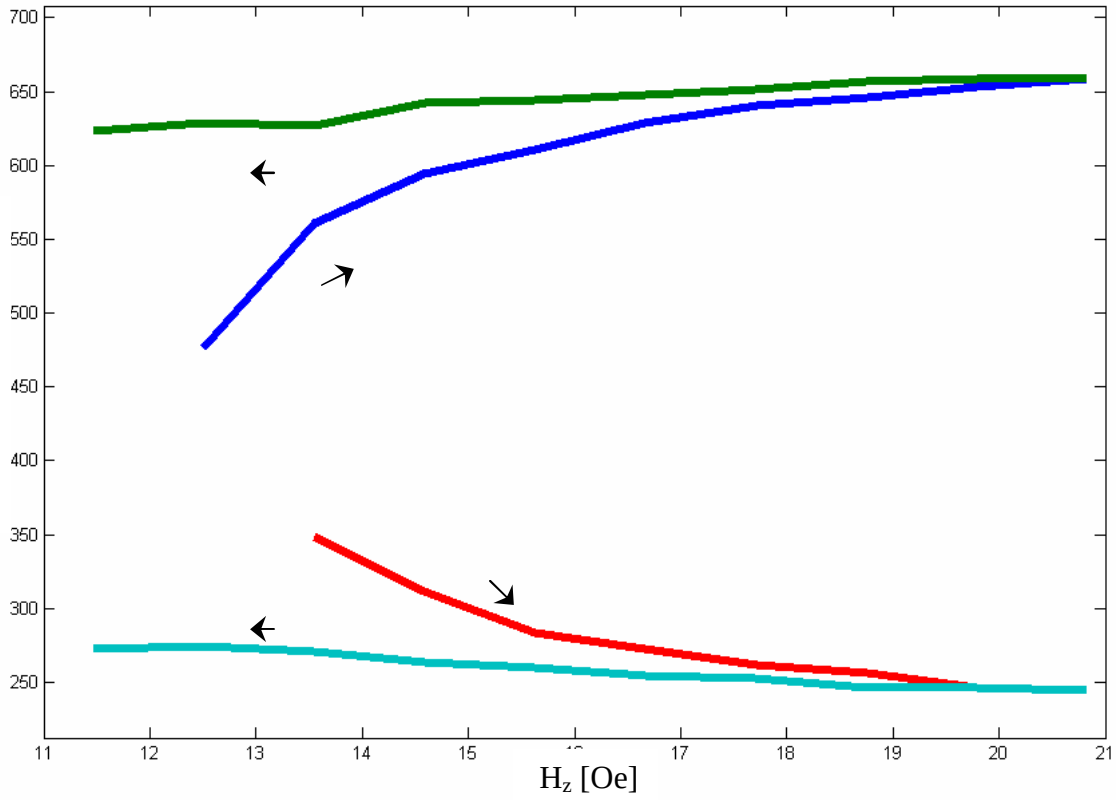

Fig. 4.2 Experimental locations of dome edges during increasing and decreasing H_z. Red and blue curves are the dome edges for field up scan while green and azure are the dome edges for field down scan.

During field modulation, the flux is kept constant as can be seen in Fig. 4.3 showing a theoretically calculated $B(x)$ at $H \pm dH/2$. The reason is that during the modulation vortices do not exit the dome. In Fig. 4.3 the differential dome profile is calculated theoretically on decreasing field while modulating with dH_z=1 Oe. We evaluate H_p=12.5 Oe from Fig. 4.1c, as the field at which the dome edges start to appear, and use eq. (2.4) to obtain H_{c1}=40 Oe. The minima points of the differential curve (red in Fig. 4.3) show the location of the dome edges. Plotting them as function of H_z during magnetization loop will produce the curve in Fig. 4.4.

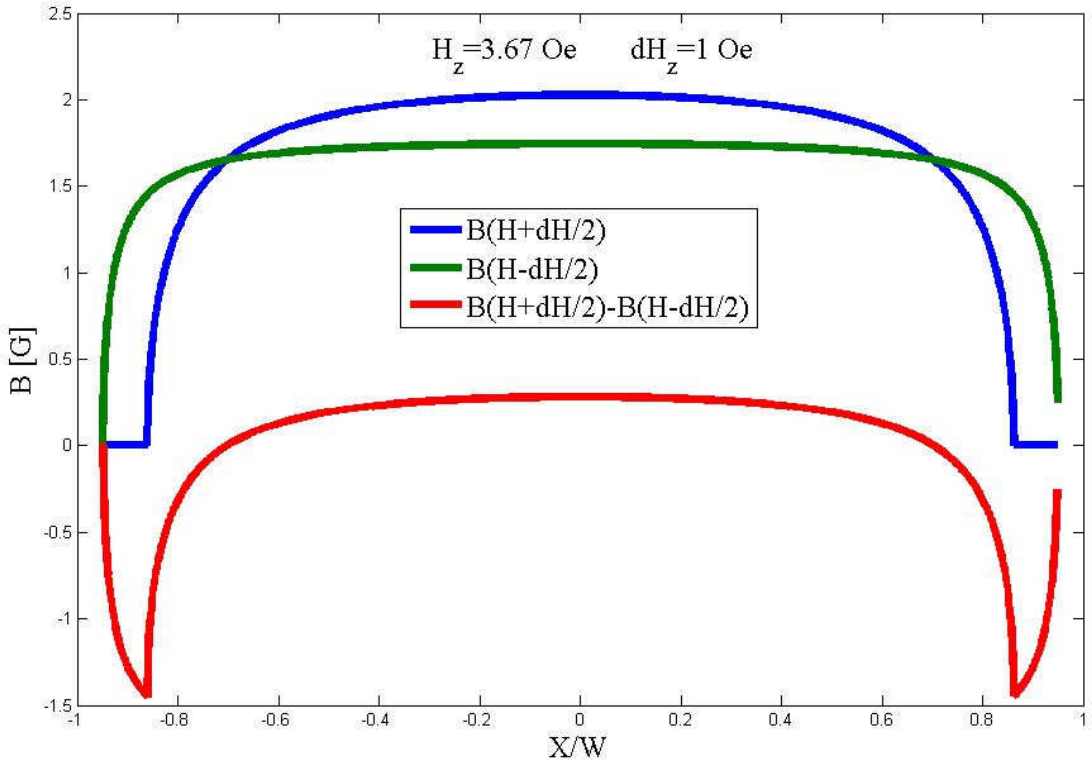

Fig. 4.3 Field modulation plot of vortex dome for H_{c1}=40 Oe while decreasing H_z. Blue curve is vortex dome for $H_z+dH_z/2$ and green curve is vortex dome for $H_z-dH_z/2$ where H_z=3.67 Oe and dH_z=1 Oe. Red curve is their difference. Here d/W=0.1 as it is for our $Bi_2Sr_2CaCu_2O_8$ samples.

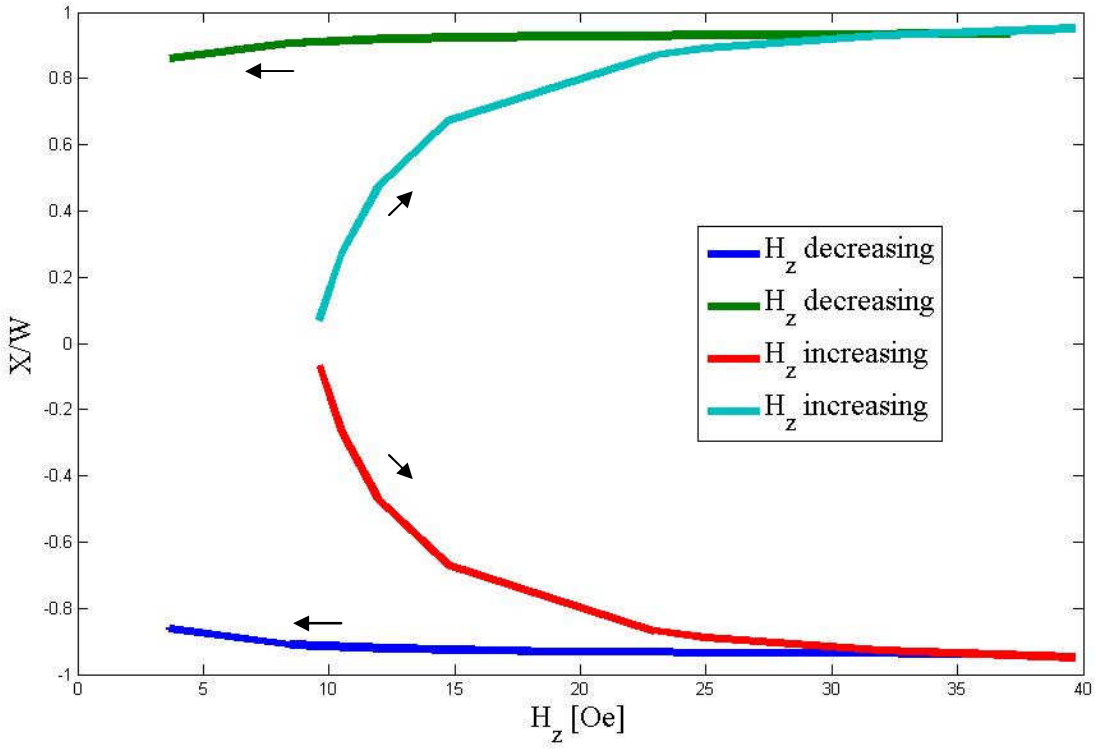

Fig. 4.4 Theoretical calculation of the location of vortex dome edges which is obtained by taking minima points from the differential curves like the red curve in Fig. 4.3.

Comparing Figs. 4.2 and 4.4 a good agreement between theoretical model and experimental measurement is found. On increasing field at H_z=13.5 Oe the dome width is about half of sample width in both Fig. 4.2 and Fig. 4.4. H_p=12.5 Oe seen in the calculation in Fig. 4.4, is also confirmed in both magnetization loop and current modulation measurements as will be seen later. Both on increasing and decreasing field, the theoretical dependence of dome edges on H_z provides a very good description of the experimental edges lines. Thus, the present measurements definitely show the vortex dome rather than a different flux phenomenon.

4.1.2 Controlled suppression of magnetization hysteresis by in-plane field

In section 2.3, three mechanisms which contribute to magnetization hysteresis were discussed. Usually in low pinning HTSC all three mechanisms affect the vortex behavior. It is therefore important to distinguish between the various contributions to the magnetic hysteresis. Thus, finding a way to affect mostly one contribution in a controllable manner is of interest.

In the last decade angular dependence of applied dc field on hysteresis was studied. It was shown that in platelet crystals, a one degree deviation of the applied field angle from the out of plane weakens the hysteresis by a factor of five [36]. The orientation of the in-plane field with respect to the crystal axes is also important; one field orientation suppresses hysteresis while the second enhances it because of linear defects which lie along one of the crystal axes [37]. Recently the group of K. Moler measured the interaction of a moving vortex with the local disorder potential by magnetic force microscopy and found vortex pinning anisotropy [38].

Scanning Hall probe microscopy experiments [39] have revealed that the PV mobility along the chains is considerably higher than in JV-free regions and it suppresses the pinning interaction between PV and defects, effectively depinning PV. In addition, from previous measurements [13,40-48] it is evident that PV preferentially enter the sample along JV, and then enjoy a much higher mobility along the JV chains [39,40,49]. In-plane field was shown to slightly decrease the PV penetration field. But, until now the prevailing opinion was that an in-plane dc field suppresses irreversibility by decreasing pinning effects and increasing mobility of PV along the vortex chains.

However, the striking observation in this work is that in a certain region of phase diagram (high temperatures and low fields), vortex chains suppress hysteresis mainly through the geometrical barrier suppression rather than pinning suppression. Until now there was no experimental evidence of a particular mechanism in which vortex chains suppress hysteresis.

In order to answer this question, this work is an attempt to achieve the following:

(a) Visualize the suppression of vortex dome by vortex chains using a method never used previously for vortex chains and vortex dome observation - current modulation. (b) Show correlation between dome width irreversibility suppression to magnetization hysteresis suppression by an in-plane field. (c) Explain theoretically how in-plane field modifies the geometrical barrier. Achieving all this will provide also an insight into the physics underlying the shaking method [3], which is extensively used to equilibrate VM.

Au contacts were evaporated onto the surface of BSCCO crystal. Instead of modulating H_z or T, a transport current with periodically alternating polarity was applied to the sample and a corresponding differential MO image was acquired and integrated, typically over a hundred cycles. As a result, the self-induced magnetic field generated by the transport current, according to the Biot-Savart law, was measured to a very high precision. With this differential imaging we are able to determine the distribution of currents as low as 0.1 mA, about 3 orders of magnitude improvement compared to previous methods [50, 51].

DMO measurements were performed by modulating the current by dI=60mA. $B(dI/2)-B(-dI/2)$ was measured during increasing and decreasing H_z at constant temperature T=82 K and constant dc in-plane field H_x. The geometry of the experiment can be seen in Fig. 3.1. Using a typical camera exposure time of 0.5 sec, each measurement point required averaging over *8* CCD camera exposures, first at $+dI/2$ and then at $-dI/2$, and calculating a difference image. Each DMO image is the average of *80* such difference images.

Field modulation affects PV density, making 2D expansion and compression of the dome and the chains. In contrast, current modulation applies on them a Lorentz force, which makes 1D translation thus succeeding to achieve a better resolution. Figure 4.5 compares DMO images of field and current modulations.

In presence of field modulation (Fig. 4.5 b), the dome is visible as dark contour around the dome due to the negative local permeability resulting from compression of the dome by dH_z. For current modulation (Fig. 4.5 a), one of the edges of the dome is visible as bright strip while the other as dark due to the small translation of the dome by the transport current. Inside the dome, diagonal defects can be distinguished. In the bottom of each picture vortex chain stripes are seen outside the dome. Apparently, current modulation provides more clear images. The vortex chains are not visible in the top part of the images due to poor proximity between the crystal and the MOI in this part.

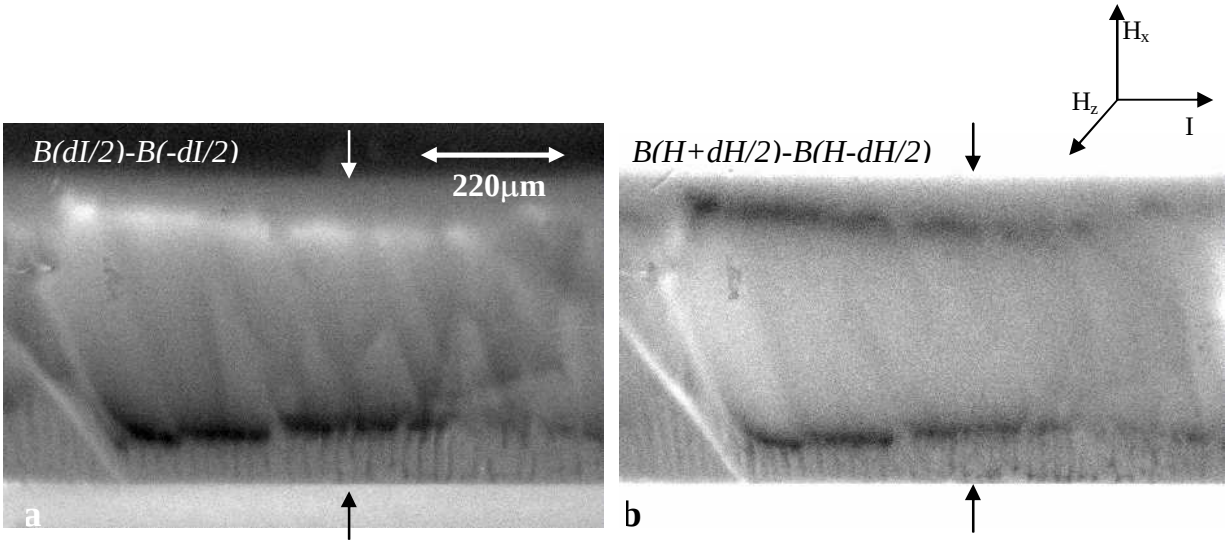

Fig. 4.5: Comparison of the same image for two modulations. The grayscale is proportional to the differential of B, while modulating with (a) current modulation of dI=60 mA and (b) field modulation of dH=1 Oe, H_x=-17 Oe and H_z=11.5 Oe while sweeping H_z up, taking same averaging. Arrows show sample edges. Current and fields directions are shown on the top right.

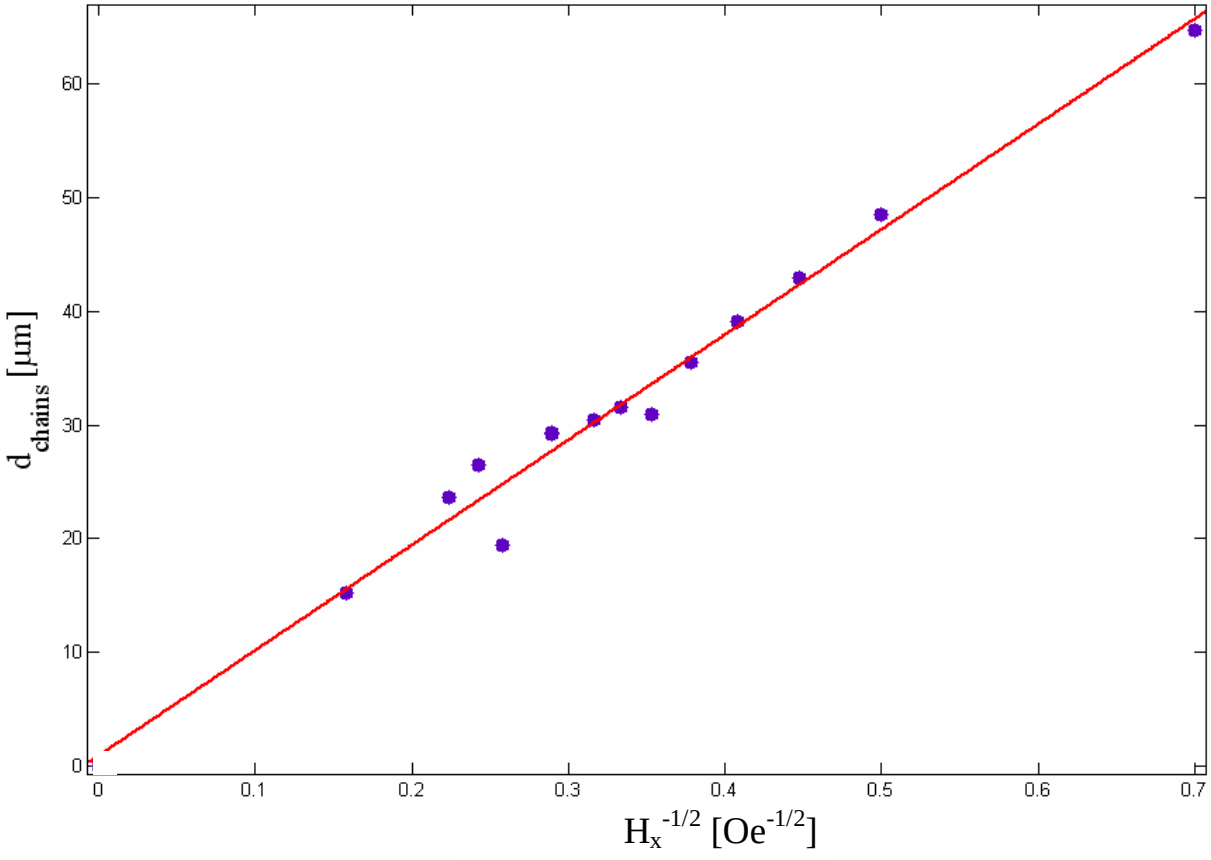

Fig. 4.6: Linear dependence of vortex chains separation with $H_x^{-1/2}$. From theoretical prediction of Eq. 2.1, the anisotropy parameter is γ=406.

Vortex chains appear in the flux free regions outside the dome like "whiskers" parallel to H_x. We observe the whiskers both in presence of field modulation and current modulation, although current modulation gives clearer images. The scaling of the distance between the whiskers vs. H_x is

consistent with vortex chains formed by JVs. Figure 4.6 shows a linear dependence of vortex chains separation on $H_x^{-1/2}$ in agreement with eq. 2.1. The slope of the fit according to eq. 2.1 gives the anisotropy parameter γ=**406**.

Y.Yasugaki et al., [41] succeeded to visualize in BSCCO vortex dome for H_z <30 Oe and vortex chains for H_z >30 Oe using field modulation. In their measurements, vortex dome appears as black boundaries perpendicular to H_x, expands towards the sample edge and finally disappears. At the same time white strip structures emerge from a fixed position at the edge of the sample indicating the vortex chains. H_x sweeping [42,43] were also done and it was seen that for slow sweeping rate vortex dome is visualized as the flux dominant object, while for fast sweeping rate JV motion cancels the dome structure, so that vortex chains can be visualized.

Our measurements visualize vortex chains only outside the dome in contrast to Y.Yasugaki. Dome boundary orientation does not seem to change with H_x direction and the number of chains does scales with H_x as expected. These differences can be explained by the fact, that their sample geometry is not long strip but a square sample and does not allow vortices enter the dome through vortex chains. If so, JV can be seen only where PVs exist to decorate them, and PVs are only inside the dome.

In Fig. 4.7, DMO images of current modulation are presented. Each image is taken from a separate H_z loop, on decreasing H_z, for a different H_x value. Vortex chains with different separation can be seen in the bottom of each image, connecting the bulk vortex dome with the edges of the crystal. The density of chains has an affect on the dome width. As we rise H_x from H_x=0 Oe to H_x=17 Oe , the black strip, which indicates the dome edge, is moving up and the white strip which indicates the opposite edge is moving down decreasing vortex dome width.

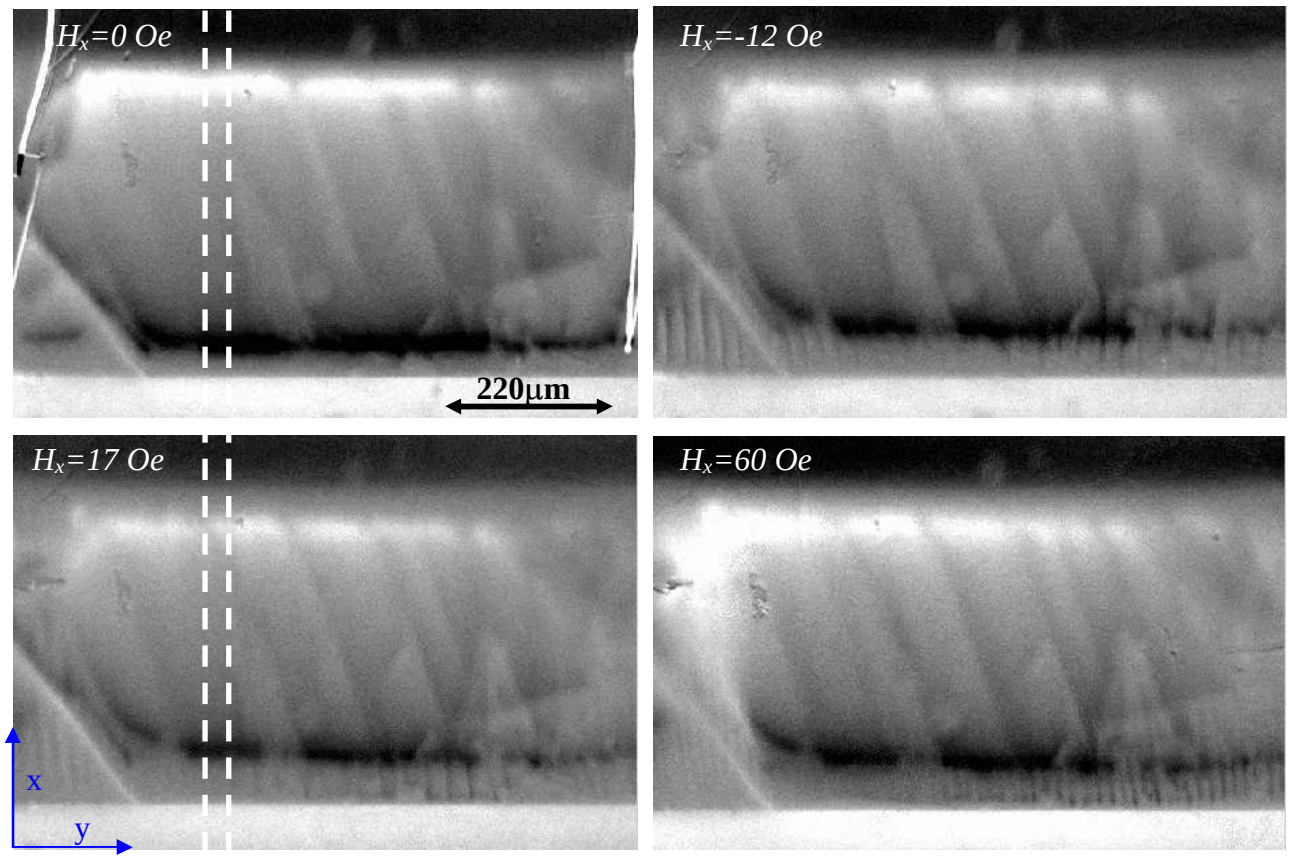

Fig. 4.7: Comparison of images with different H_x while sweeping H_z down. T=81.9 K H_z=10.5 Oe dI=60 mA. The dashed white lines show where vortex dome profile was measured.

The measurements in Fig. 4.7 could not be visualized so efficiently by any technique other than magneto optics. Magneto optics gives us immediately the dome profile in very high resolution and in the range of the whole sample, thus making it possible to observe clearly the instantaneous changes of whole vortex dome profile by changing the fields.

There are many parameters affecting the geometrical barrier. It was shown theoretically [27] that prism geometry samples do not have geometrical barriers, and magnetization loops of platelets and prism shaped crystals were compared to show that hysteresis of the latter is weaker and closes at lower fields than the former [52,27]. Our measurements expand this finding and show gradual contribution of vortex dome to hysteresis by an in-plane field rather than the discrete effect of changing sample geometry [52]. Our purpose now is to see the effect of an in-plane field on geometrical barriers and on hysteresis, showing a correlation between the two.

In Fig. 4.8 we see a profile of the data along the white dashed lines in Fig. 4.7, where the y axis between the dashed lines was averaged. We measure in Fig. 4.7 the upper bright strip of vortex dome profile, and take an intensity threshold of 1 to detect the point where the dome starts to appear. This point is the definition of the parameter b, which was discussed in section 2.3.1. The point b can be seen in Fig. 4.8. We take here the location point where the dome starts to appear, as this is the

determination of b. An intensity threshold of -1 and +1 for the intensity minima and maxima was chosen, as an indication to the x location where the dome starts to appear.

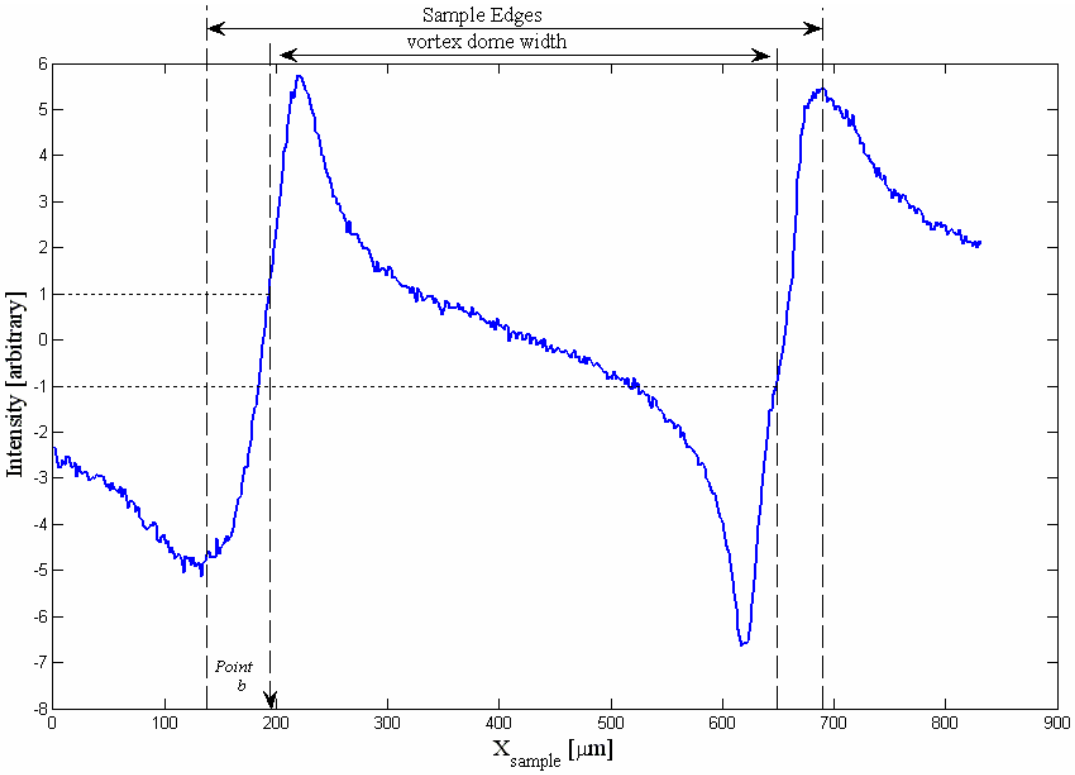

Fig. 4.8: Intensity profile inside the region marked by white dashed lines in Fig. 4.7. Sample edges and dome width are shown. Intensity thresholds of 1 and -1 for the maxima and minima peaks respectively are defined as the dome edges.

The profile in Fig. 4.8 results from the Lorentz force that shifts the dome. Figure 4.9 shows two vortex domes which were shifted by the current. Their difference reproduces the experimental result of Fig. 4.8.

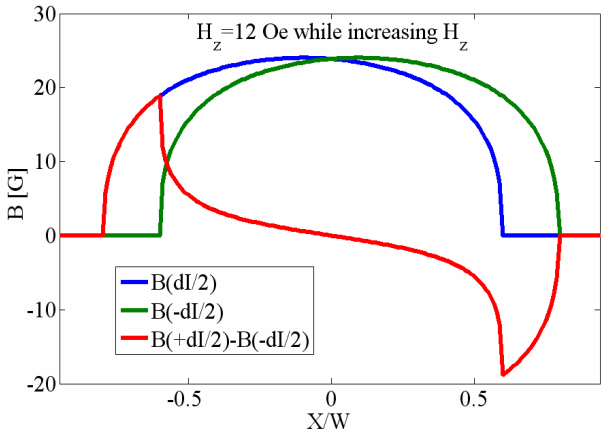

Fig. 4.9: The effect of applied current on dome position. The dome was calculated using Eq. 2.6, and shifted qualitatively to the right and left to show the effect of applied current. The red curve is the expected differential profile that explains the experimental curve in Fig. 4.8. H_{c1}=40 Oe was used here.

Using the threshold analysis of Fig. 4.8 the curves in Fig. 4.10 for positive H_x were obtained. As H_x increases, vortex dome edge position becomes progressively more reversible, as the separation between the curves on increasing and decreasing H_z diminishes. In Fig. 4.10, hysteresis is about to close at H_x=17 Oe suggesting that this is the field needed to equilibrate the dome. In Fig. 4.11 we plot the width of the hysteresis at H_z=9.4 Oe as marked by the dashed lines in Fig. 4.10. Two kinds of hysteresis will be studied: hysteresis in dome width or equivalently in dome edges location *b* and

in local magnetization determined by B-H_z. Both types of hysteresis will be evaluated at the point H_z=9.4 Oe to obtained the largest effect. The two types of hysteresis could be different if other sources of irreversibility, like pinning, are present. We expect that pinning plays relevant role, and JVs help to overcome the pinning force by enhancing the mobility along the chains. However, as shown below, we find that for H_z <20 Oe and high T=82 K , H_x affects hysteresis in local magnetization mainly through geometrical barrier.

Figure 4.11 is obtained by subtracting the values of b on decreasing and increasing H_z at H_z=9.4 Oe for the various H_x curves. Clear vortex dome hysteresis suppression by H_x can be seen. For H_x=0 Oe the hysteresis width is Δb=25 μm, while for H_x=15 Oe it is Δb=5 μm, showing hysteresis reduction by a factor of five from H_x=0 Oe to H_x=15 Oe.

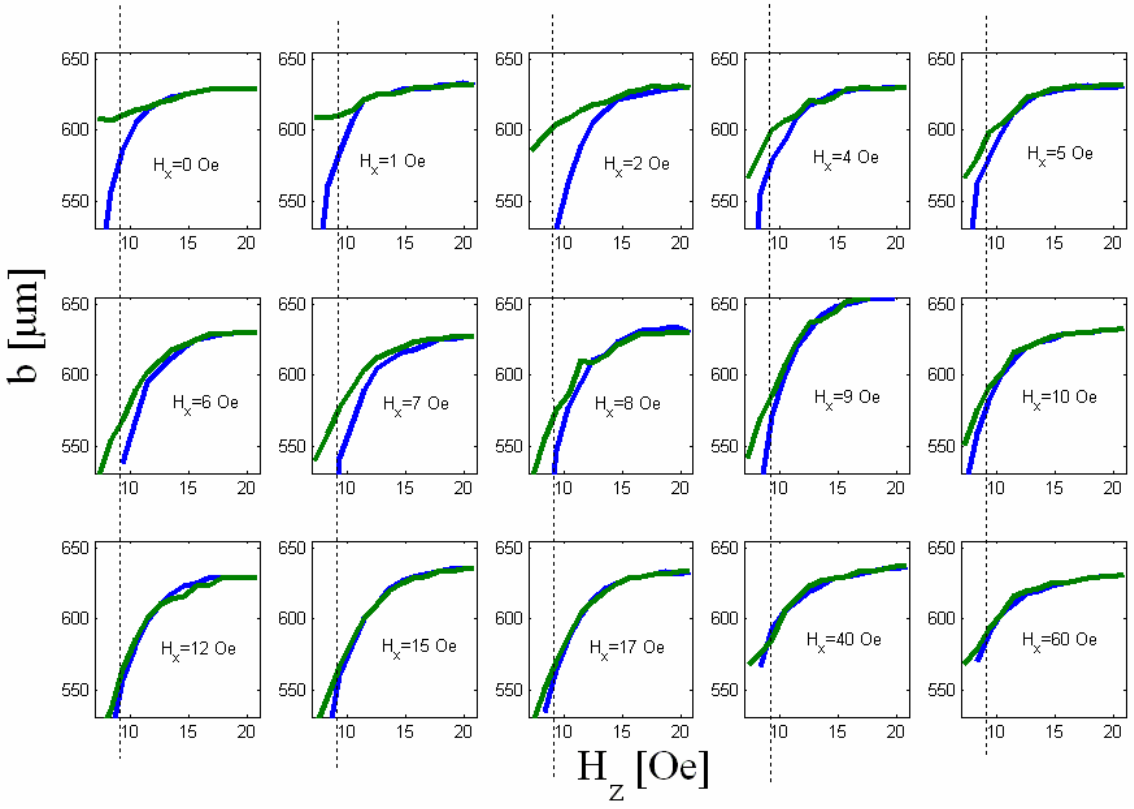

Fig. 4.10: The location of vortex dome edge $b(H_z)$ while sweeping H_z up (blue lines) and down (green lines) for various positive in-plane fields. The points $b(H_z)$ were obtained by threshold of 1 described in Fig. 4.8. In the measurements H_z was swept in steps of 1 Oe from H_z=0 Oe to 20 Oe and back.

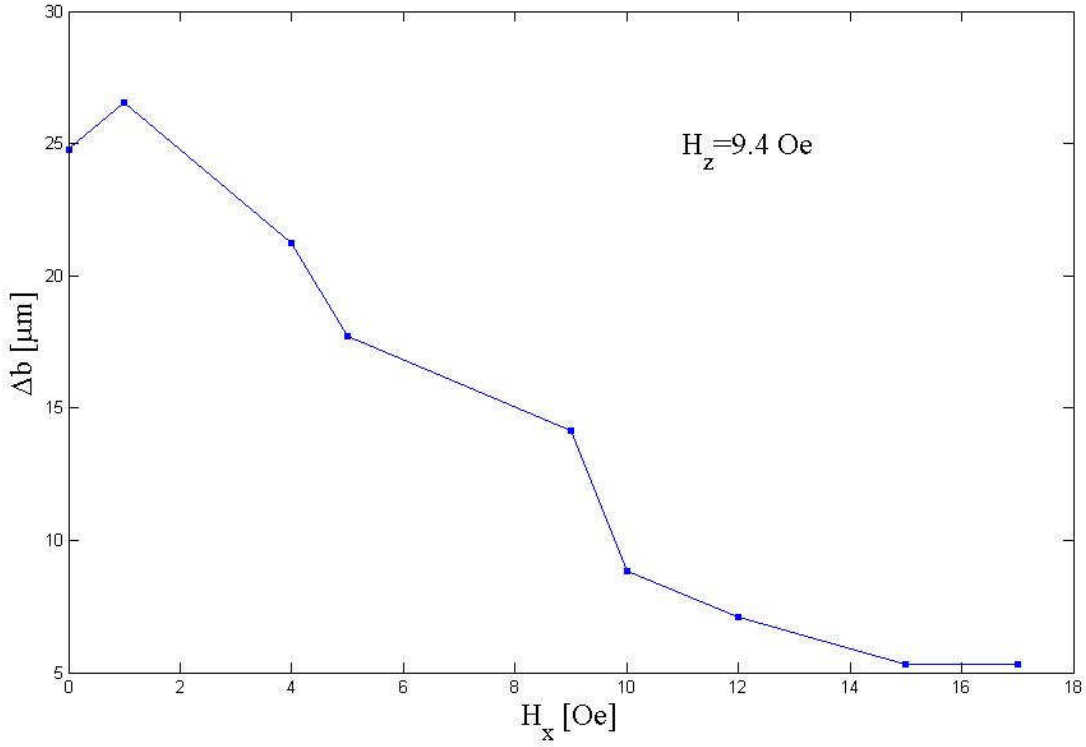

Fig. 4.11: Width of the vortex dome edge hysteresis vs. H_x obtained from the data in Fig. 4.10 at H_z=9.4 Oe.

Now let us observe the effect of in-plane field on magnetization loops. Figure 4.12 shows various magnetization loops for different values of in-plane field. The dashed lines show where the hysteresis will be evaluated. Figure 4.13 shows magnetization hysteresis suppression with an in-plane field calculated the same way and in the same field H_z=9.4 Oe as in Fig. 4.11. According to Fig. 4.13, for H_x=15 Oe the width of the hysteresis is $\Delta(B\text{-}H_z)$=1.5 G while for H_x=2 Oe it is $\Delta(B\text{-}H_z)$=7.5 G. As in Fig. 4.10, here also hysteresis is reduced by a factor of five from H_x=2 Oe until H_x=15 Oe suggesting that one hysteresis behavior leads to the other. The functional dependence in Fig. 4.12 and Fig. 4.10 also looks quite similar. The equilibration field for which the hysteresis is about to vanish H_x=17 Oe is evident also in Fig. 4.12. In contrast to previous studies [40,49], Fig. 4.12 does not show a decrease in the first penetration field H_p. It seems that H_p remains constant vs. H_x.

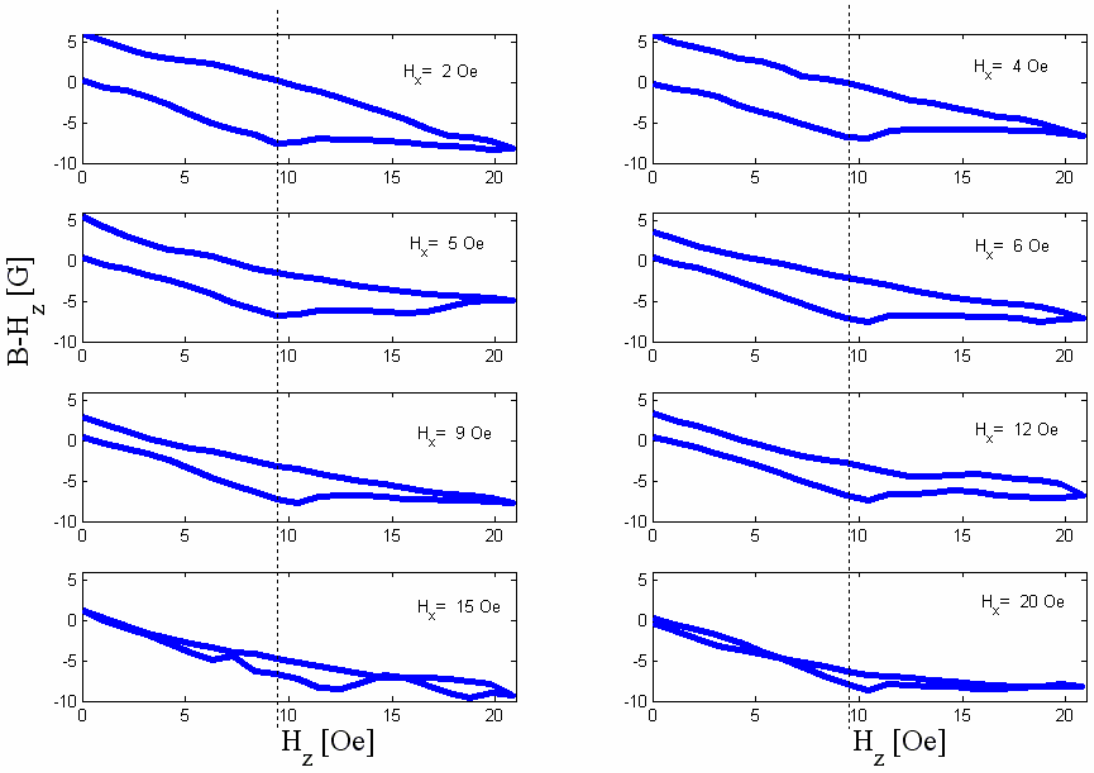

Fig. 4.12: Local magnetization loops of $Bi_2Sr_2CaCu_2O_8$ sample for various positive in-plane fields. The measurement is an average on square 10X10 μm^2 in the center of the sample. In the measurements H_z was swept in steps of 1 Oe from H_z=0 Oe to 20 Oe and back at T=82 K.

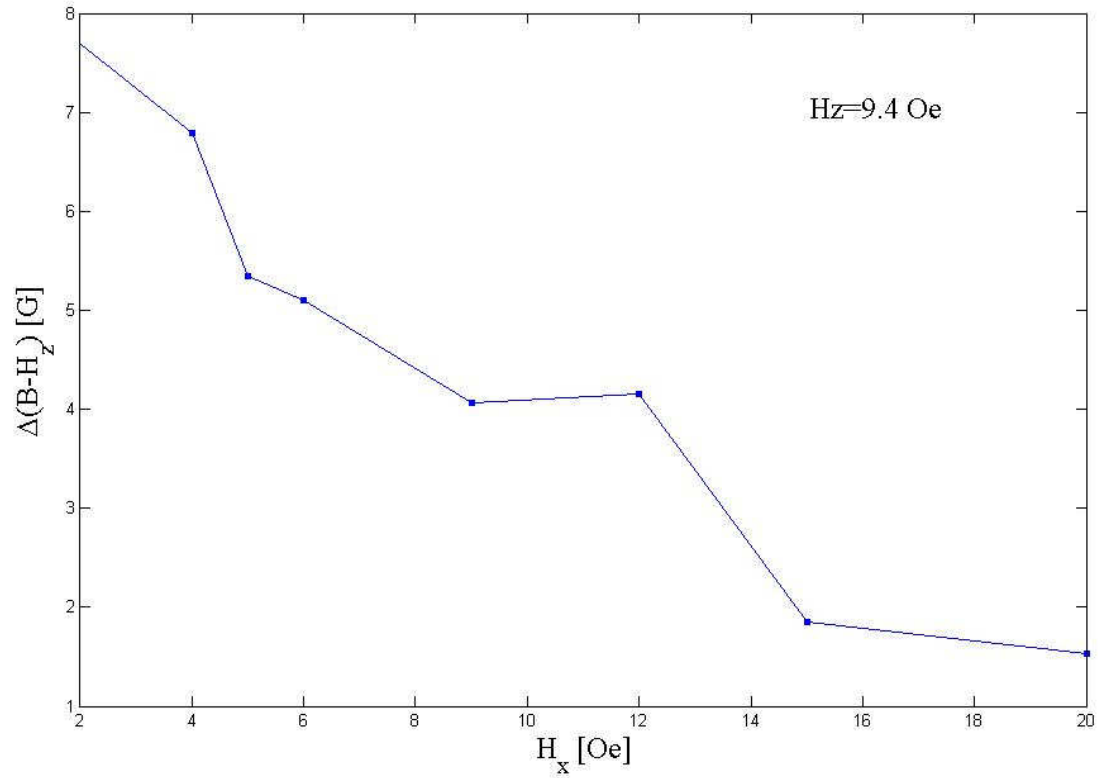

Fig. 4.13: Suppression of local magnetization hysteresis by in-plane field. The hysteresis is evaluated by subtracting the magnetization of field up scan from field down scan for H_z=9.4 Oe. This is shown as dashed lines in Fig. 4.12.

Hysteresis suppression with increasing H_z can be also compared for these two cases. According to Eq. 2.6 we expect that hysteresis in the dome edge b, will give rise to hysteresis in B, and thus also in B-H. However this is true only if the geometrical barrier is the dominant source for hysteresis, and there are no significant effects of pinning and B-L surface barriers. Here we will check the geometrical barrier dominance.

Experimentally a similarity in hysteresis suppression with H_z can be observed. This will be presented for negative H_x to show that the sign of in-plane field does not change the similarity. In figure 4.14a vortex dome edge loop for H_x=-15 Oe is shown, and it is compared to the magnetization loop for the same H_x. At H_z=12.3 Oe marked by the dashed line, a strong reduction can be distinguished in the magnetization on increasing field, giving rise to significant hysteresis reduction for H_z>12.3 Oe. At the same field, H_z=12.3 Oe, the irreversibility in dome edge is closed completely. This suggests that the sudden suppression in the magnetization hysteresis is caused by the fact that vortex dome ceases to contribute to hysteresis at this point.

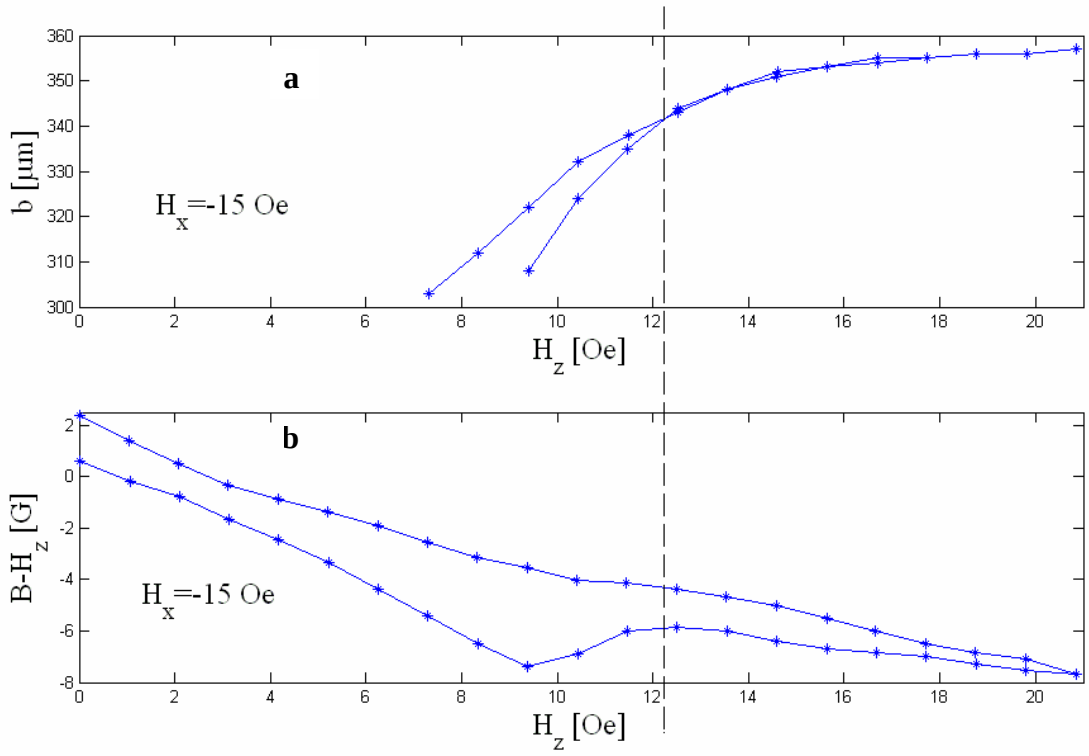

Fig. 4.14: (a) Dome edge loop as function of H_z. (b) Local magnetization loop B-H_z as function of H_z. At H_z=12.3 Oe a sudden decrease in magnetization is observed followed by significant suppression of the hysteresis. The irreversibility point of dome edge in (a) also corrssponds to the same H_z=12.3 Oe. H_x=-15 Oe, T=82 K.

As can be seen in Fig. 4.10, the decreasing field branch of the loop (green) gradually approaches the increasing field branch (blue) upon increasing H_x. This decrease in dome edges location for decreasing H_z which leads to equilibration can be observed also in Fig. 4.15. This figure shows the

location of dome edges for H_z=7 Oe on decreasing field in Fig. 4.10 for different H_x. It can be seen that while rising H_x, vortex dome reduces 35% of its width from W_{dome}=440 μm to W_{dome}=290 μm while increasing H_x from 0 Oe to 17 Oe, proving a very strong effect of H_x. As expected, the equilibration field $|H_x|$=17 Oe is visible here, as we see a constant dome width above $|H_x|$=15 Oe.

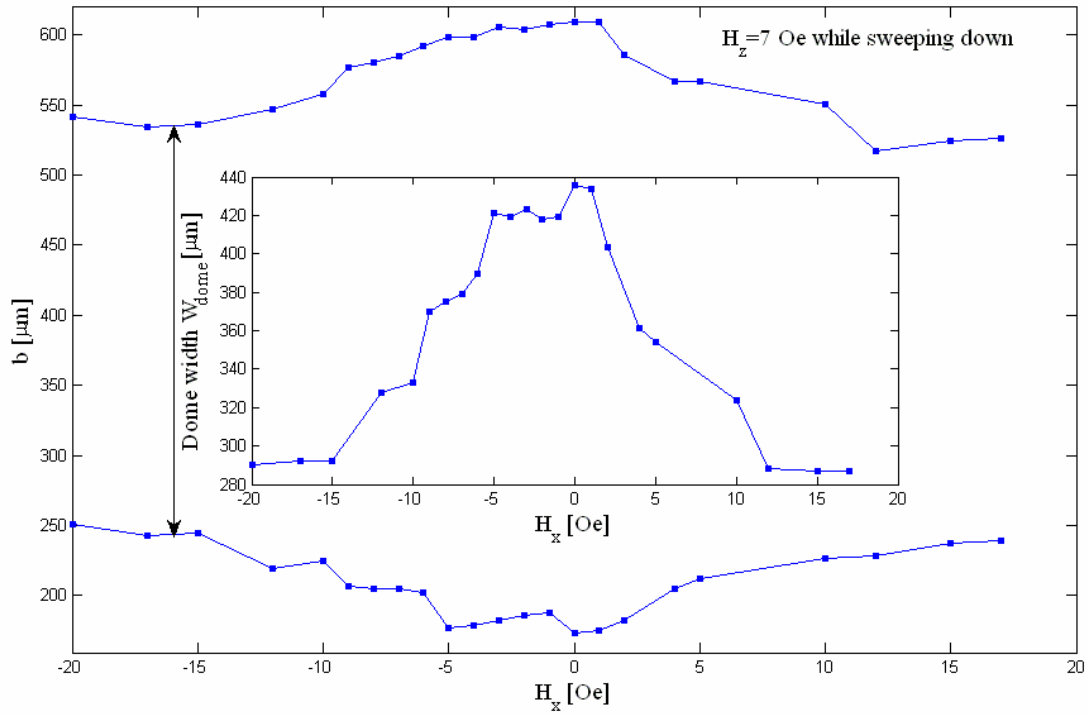

Fig. 4.15: Location of the two dome edges vs. H_x. Every point is taken from a separate H_z loop while sweeping H_z down at H_z=7 Oe. Inset: the dome width vs. H_x showing equilibration for $|H_x|$>15 Oe.

Our novel explanation to the way in which dc H_x field suppresses hysteresis is based on the statement that JV create 1D channels (which were visualized in Fig. 4.7) from the sample bulk to the sample edges. Along these channels the potential created by shielding currents is reduced and vortex exchange between bulk and surface is possible. As a result, the geometrical barrier is suppressed. In Fig. 4.15 we see that H_x changes dome edges, and thus affects the efficiency of vortex exchange. We will now try to explain this effect based on the recent models of geometrical barrier and JV-PV interaction.

Let us try to understand theoretically the situation in which there is a vortex dome with "whiskers" of vortex chains in the flux free region. For this, we need to calculate the reduction of vortex energy due to interaction with JV in order to explain the long whiskers sticking out of the dome.

Basically an in-plane field does two things to JV: changes JV out-of-plane separation by eq. (2.2) and changes JV in-plane separation by eq. (2.1). In Fig. 4.6 the anisotropy parameter was measured to be γ=**406**. In section 4.1.1 another important parameter was obtained by showing agreement

between theoretical vortex dome width to experiment. It was found that H_{c1}(T=82 K)=40 Oe. Now we can use these results in our calculation of energies.

According to A. Koshelev [8,12], the interaction energy between single JV and single PV is given by

$$E_x = -\frac{2.1\phi_0^{\,2}}{4\pi^2\gamma^2 s\cdot \ln\frac{3.5\gamma s}{\lambda_{ab}}} \tag{4.1}$$

where λ_{ab} is the penetration depth, s is the CuO_2 planes separation, and γ is the anisotropy parameter. The c-axis distance between JVs is given by eq. (2.2). Assuming sample thickness d, the total number of JV layers is

$$N(H_x) = \frac{d}{d_c} = d\sqrt{\frac{\sqrt{3}\gamma H_x}{2\phi_0}} \tag{4.2}.$$

Thus total interaction energy is the sum of interactions between PV and all the JV across sample thickness and is given by $E_{xt}(H_x) = N\cdot E_x$. We have estimated from the measurements the following parameters: H_{c1}=40 Oe, γ=4**06**. Substituting also the typical values for BSCCO :

λ_{ab} (T=0) =0.2 μm, so $\lambda_{ab}(T=82K) = \frac{\lambda_{ab}(T=0)}{\sqrt{1-(\frac{T}{T_c})^2}} = \frac{\lambda_{ab}(T=0)}{0.4} = 0.5\mu m$,

s=$15\cdot 10^{-4}$ μm , ϕ_0=20.7 G · μm ^{2}, we obtain $E_{xt}(H_x) = N\cdot E_x = -\frac{\sqrt{H_x}}{265}\varepsilon_0 d$

where we used $\varepsilon_0 = \frac{H_{c1}\phi_0}{4\pi}$ in order to write the energy in terms of ε_o, and H_x is in units of Oe.

T. Tamegai evaluated [53] the crossing energy experimentally and found it to be significantly larger than the theoretical prediction, with a ratio of: $\frac{E_x(theo.)}{E_x(ex.)} = 0.15$. If we use this ratio we obtain

$$E_{xt}(H_x) = -\frac{\sqrt{H_x}}{39}\varepsilon_0 d \tag{4.3}$$

Shielding currents are location dependent, as was seen in Fig. 2.8b and 2.5. Therefore, Lorentz force applied on PV is also location dependent. The vortex energy per unit length due to the Lorentz force is given by [25,54,55]

$$\varepsilon(x) = \varepsilon_0\left(1+\frac{4\pi}{H_{c1}}\int_x^W J_y(t)dt\right) \tag{4.4}$$

According to the geometrical barrier model [25], the current is given by Eq. 2.7.

For b<x<W-d/2 if we use $J_E = \frac{2c\varepsilon_0}{\phi_0 d}$ we get

$$\varepsilon(x) = \varepsilon_0\{1 - \frac{2}{d}[W - e + \frac{2}{\pi}W * I(x,b,e)]\} \tag{4.6}$$

where

$$I(x,b,e) = \int_{x/W}^{e/W} \arctan\sqrt{\frac{(1-(\frac{e}{W})^2)(t^2-(\frac{b}{W})^2)}{(1-(\frac{b}{W})^2)((\frac{e}{W})^2-t^2)}}dt \tag{4.7}$$

For x>W-d/2 we have to add the linear potential due to elongation energy described in section 2.3.1.

$$\varepsilon(x) = \varepsilon_0\{1 - \frac{2}{d}[W - e + \frac{2}{\pi}W * I(x,b,e)] - [\frac{2}{d}(x - (W - \frac{d}{2})]\} = \varepsilon_0\{1 - \frac{2}{d}[x - e + \frac{d}{2} + \frac{2}{\pi}W * I(x,b,e)]\}$$

When H_z is varied, b and e behave as was described in section 2.3.1. Using this, we can plot energy across the sample for various H_z. This is shown in Fig. 4.16. It coincides with the curves in Ref. 25. Figure 4.16 shows that there is no barrier for vortex penetration for $H_z > H_p$, because $\varepsilon(x) \le 0$ everywhere. In presence of JVs, the energy of PVs will be reduced by E_{xt} given by Eq. 4.3 to penetrate along the JVs, and this is the explanation of images in Fig. 4.5.

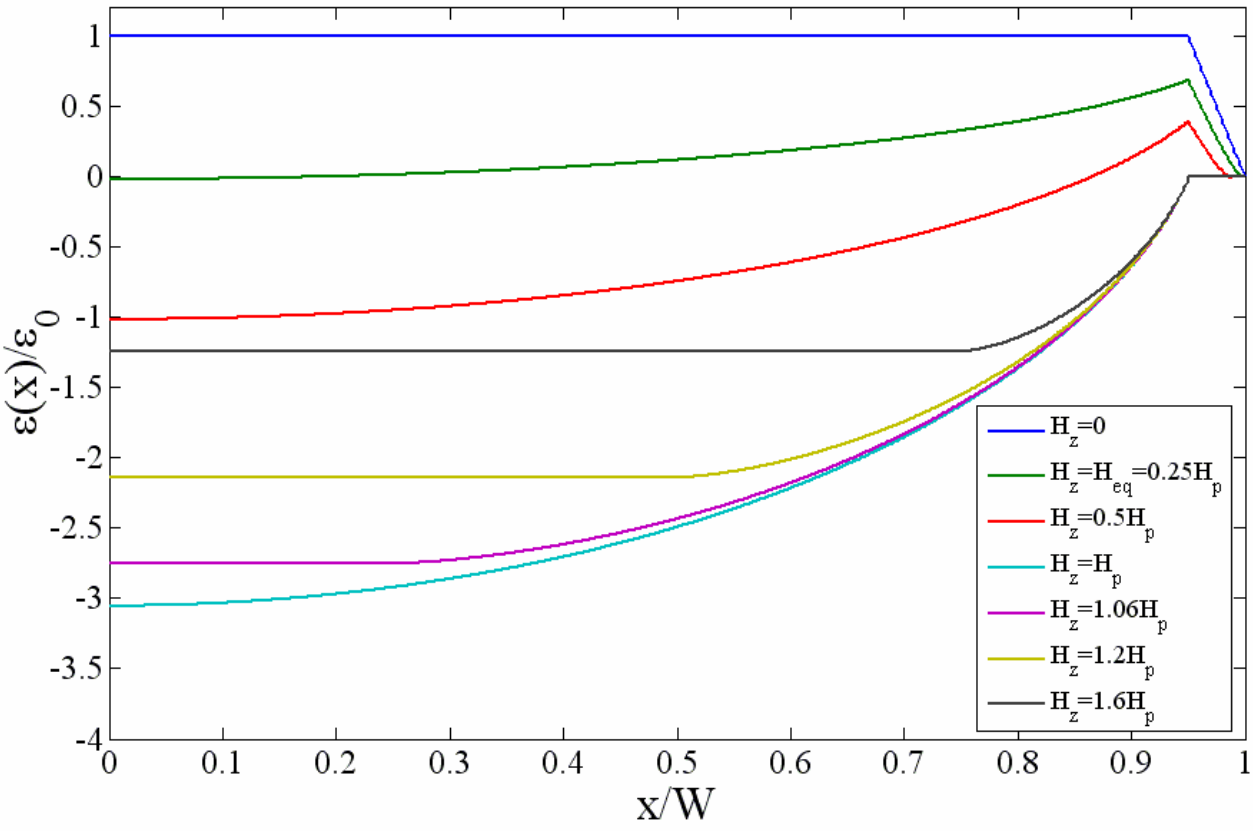

Fig. 4.16: Vortex energy across the sample for various H_z. The green curve $H_z=H_{eq}$ corresponds to the equilibrium penetration field, but vortices start to penetrate only at higher $H_z=H_p$ due to the energetic barrier at the edge.

Now we can understand the gradual suppression of dome hysteresis by H_x. H_x raises the JV-PV attractive interaction, and thus lowers the energetic barrier for vortex exit. For H_x=0, [25] there is no thermal activation over such an extended barrier, which involves macroscopic energy of $d \cdot \varepsilon_0$ (eq. 4.3). However in the chains scenario, we see that this extended macroscopic barrier reduces, and due to thermal fluctuations of PV, some percent of the PV will overcome the barrier according to Maxwell-Boltzman probability function. Raising H_x will increase the probability and thus contribute more to vortex dome equilibration.

Thus, the suppression of dome irreversibility with chains was visualized by using a new method for this purpose - current modulation. It was found that the in-plane magnetic field, which dictates chains density, tunes the dome reversibility. This tuning is made by tuning the c-axis density of JV and thus tuning the interaction between JV and PV to overcome the barrier strength. Measurements of hysteresis were provided which show direct dependence and strong correlation between the irreversibility of the dome behavior, and the irreversibility of the sample's magnetization. The correlation was shown both as a function of H_z and H_x. Vortex dome contribution to hysteresis caused by the in-plane field was separated from other contributions to hysteresis. Magnetization hysteresis for high temperatures and low fields is mainly due to geometrical barrier. This hysteresis can be suppressed by in-plane field which has crucial effect on geometrical barrier.

These finding can explain the mechanism that suppresses the geometrical barrier in presence of vortex shaking by ac H_x [3]. Apparently PV can penetrate the sample and move into or out of the vortex dome along the whiskers formed by JV.

Thus we confirm the hypothesis that magnetization hysteresis is affected in a controllable manner by an in-plane field through its effect on vortex dome hysteresis. This effect is shown to be achieved by creating vortex chains which serve as 1D channels for flux exchange between sample bulk and the sample edges.

4.1.3 Phase transitions from 2D vortex dome to 1D chains

Another novel phenomenon which was observed in these measurements is a phase transition from 2D vortex dome, to 1D vortex chains with edges arranged as a dome profile. This phase transition occurs only when H_z is swept down, and thus may be a source of irreversible behavior. However there is a minimal field H_x, only above which a phase transition is seen. The equilibration field from the previous section H_x=15 Oe was chosen to show the phase transition in Fig. 4.18. During the phase transition, apparently much flux exits the sample. The phase transition occurs at H_z=6.26 Oe. For fields above H_z=6.26 Oe the dome is observed and the dome width decreases with decreasing H_z.

However for fields below H_z=6.26 Oe chains are formed and their edges expand towards the sample edges with decreasing H_z.

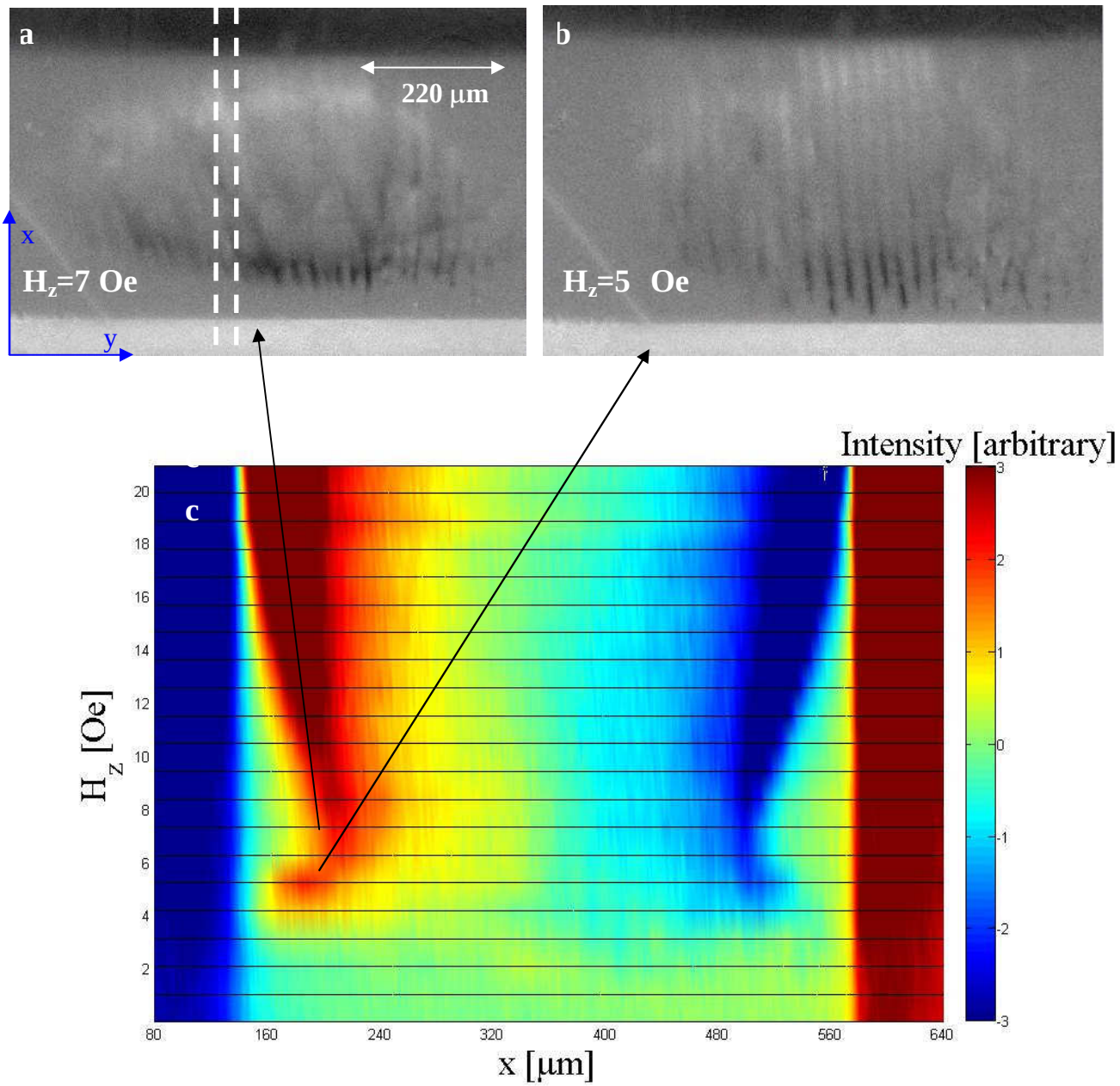

Fig. 4.18: Phase transition from (a) 2D vortex dome to (b) 1D vortex chains while sweeping H_z down for H_x=-17 Oe. dI=60 mA. (c) Evolution of dome profile on decreasing H_z at H_x=15 Oe. The signal was integrated over the strip marked by the white dashed lines in (a). At H_z=6.26 Oe there is a phase transition from dome to chains. For H_z<6.26 Oe we see that the location of chain edges increases towards the sample edge with decreasing the field.

To understand this transition, let us take a look at the energy inside the dome by using Eq. 4.6. The energy inside the dome is given by $\varepsilon = \varepsilon_0\{1-\frac{2}{d}[W-e+\frac{2}{\pi}W*I(b,b,e)]\}$ where $I(b,b,e)$ is given by Eq. 4.6. It is plotted in Fig. 4.19.

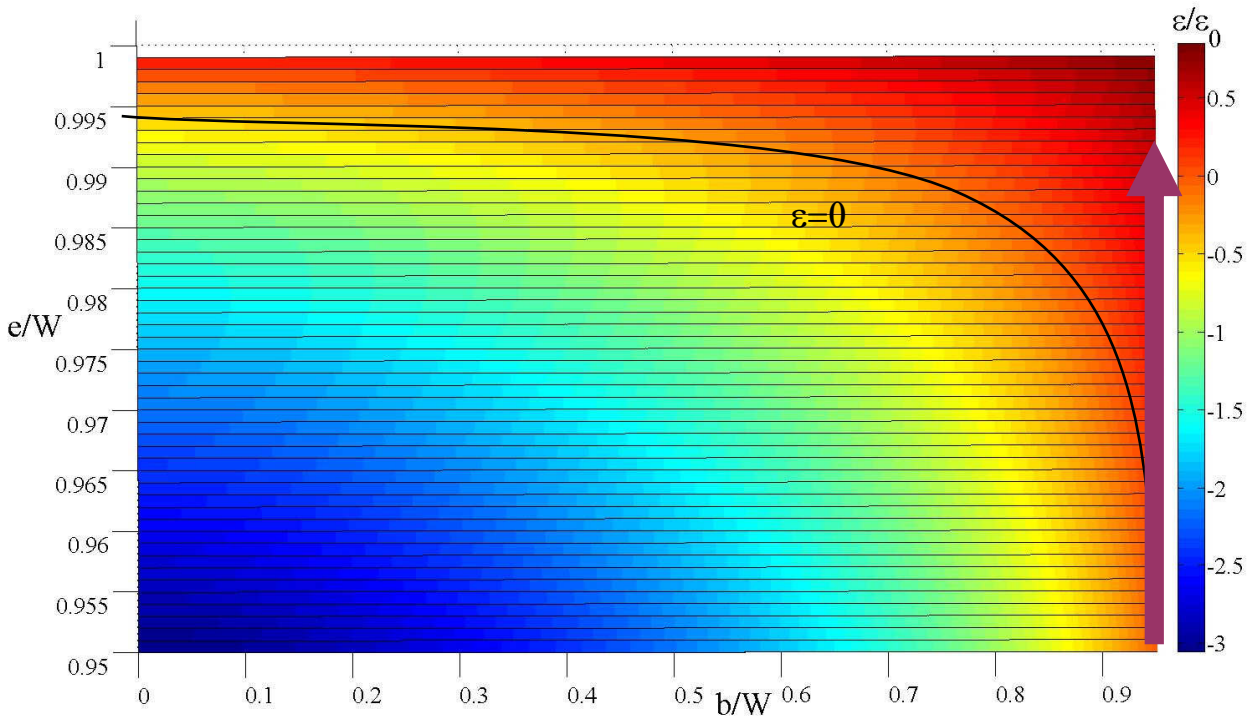

Fig. 4.19: Energy inside the dome given by Eq. 4.6. The black line shows the zero energy curve. The pink arrow shows the trajectory of decreasing H_z.

When H_z is decreased along the pink arrow in Fig. 4.19, at some field the energy inside the dome turns to be positive, as can be seen in Fig. 4.19. The structure of PVs rearranges from the dome configuration to the chain configuration, as is seen in Fig. 4.18. After this phase transition, the concentration of PV increases much on the 1D chains, and elastic repulsion between PVs results in their exit outside the sample as is evident in Fig. 4.18c.

A theoretical explanation to the phase transition was described in Refs. 8,12. It considers the phase transition to be as a result of an energies equilibration between the PV-JV attraction energy given by Eq. (4.1) and the PV elastic repulsion energy in the chains. According to E. Koshelev [8,12], the critical field for a stable chain with PV repulsion is given by

$$H_c = \frac{\phi_0}{\lambda_{ab} d_{ab} \ln(\frac{d_{ab}\gamma s}{\lambda_{ab}^2})} \tag{4.8}$$

where d_{ab} is given by eq. (2.1). This means that the isolated chain state is stable when H_z and H_x satisfy the following inequality:

$$\frac{H_z^2}{H_x} < \frac{2\phi_0}{\sqrt{3}\cdot\gamma\cdot\lambda_{ab}^2\cdot\ln^2(\frac{d_{ab}\gamma s}{\lambda_{ab}^2})} \tag{4.9}.$$

All these features of crossing lattices agree very well with our experimental observations.

Eq. (4.9) shows weak dependence of the transition point on H_x, and indeed checking the range of H_x from 0 to 20 Oe showed only a small variation of the phase transition point from H_z=5 to 7 Oe.

4.2 Vortex behavior in presence of periodic surface holes

As was discussed in section 2.3.2 and was shown in Fig. 2.10, any kind of inhomogeneity in the crystal serves as a potential well which pins vortices. In order to study this effect, artificial pinning of different types is patterned in our lab. Earlier in our lab, S. Banerjee [56] and N. Avraham [57] studied BSCCO with columnar bulk defects made by heavy ion irradiation. BSCCO samples were irradiated with high energy ions of Pb, and columnar defects disordered in the a-b plane were obtained.

For measurements presented in the current work, the focus is on another type of artificial inhomogeneties: periodic surface holes. BSCCO samples, prepared in our lab, were patterned with periodic surface holes arranged in a triangular lattice. The typical spacing periods range from 0.8 μm up to a few microns. Surface holes were created on a square regions 170X170 μm^2 using the focused ion beam (FIB) facility either in the Technion (Haifa) or Bar Ilan Univ. (Ramat Gan). An example of a hexagonal array with lattice constant d = 2.17 μm, is shown in Fig. 4.20.

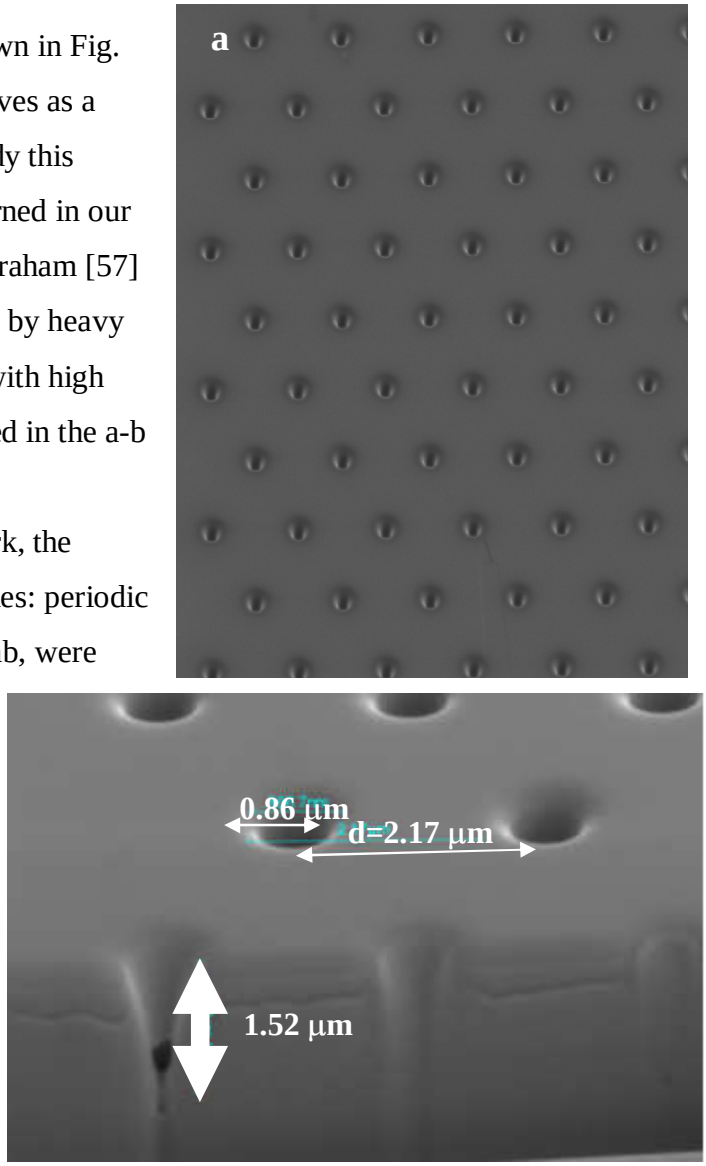

Fig. 4.20 Surface holes in $Bi_2Sr_2CaCu_2O_8$ crystal made by focused ion beam: (a) zoom out, (b) zoom in images.

The goal of section 4.2.1 is to discuss the static behavior of vortices in the presence of surface holes, while section 4.2.2 presents transport measurements which point on dynamic properties.

Statically, we expect that columnar defects promote disorder in vortex matter while surface hole promote order. Dynamically, at temperatures above T_c assuming that the current flows mainly on the sample surface where the contacts were evaporated, we expect to see reduced conductivity in surface holes compared to pristine region because of reduced conducting materials, in contrast to columnar defects. And indeed S. Banerjee did not distinguish the patterned regions above T_c.

4.2.1 Matching effect and melting with field modulation

Using field modulation on the patterned region, a very interesting physical phenomenon can be demonstrated. This phenomenon is called matching [58,59]. When the applied field corresponds to a vortex density which is identical to the hole density, enhanced pinning and reduced compressibility of the vortex matter is expected. A vortex phase, where every vortex sits on every hole, is formed and there are essentially no free remaining vortices. This state is energetically favorable and will stay so up to some elevated temperature. In this state no extra vortices will be allowed to enter the patterned region. Matching fields [58,59] are given by the formula

$$m \cdot B_\phi \tag{4.10}$$

where $B_\phi = \frac{\phi_0}{S} = \frac{2\phi_0}{\sqrt{3}d^2}$, S is the area of a unit cell of the holes array, d is the interhole distance and m is an integer number.

Figure 4.21 presents a DMO image of the BSCCO crystal with field modulation showing a region patterned by periodic surface holes with a lattice constant of d=1 μm corresponding to B_ϕ=23.9 G seen in the image as a dark square, because of reduced vortex reversibility in this region.

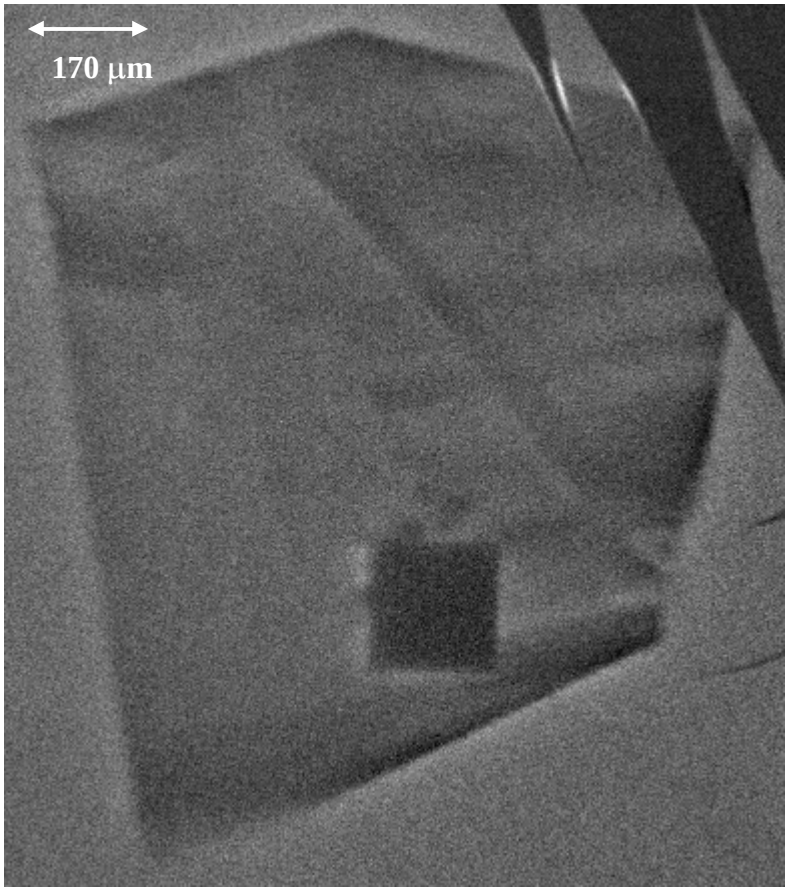

Fig 4.21: DMO image of the measured BSCCO sample with dH_z=1 Oe, H_z= 25 Oe and T=83.3 K. The patterned region is seen as a dark square. The black triangles on the top right side are magnetic domains of the MO indicator.

Figure 4.22 shows the signal, integrated over the entire patterned region versus temperature and field. *dB/dH* is represented by the color. The blue region is the irreversibility region of vortices where *dB/dH* is close to zero. Modulating the field does not move the vortices and thus B is constant. The red region is the reversible region where *dB/dH=1*. In this region pinning forces stop playing a role. As can be seen, the matching field in Fig. 4.22 is H_ϕ= 25 Oe. It agrees with the calculated B_ϕ=23.9 G. The reason for the difference between experimental and calculated matching field is because H>B in mixed state (see Fig. 2.4b).

At the matching field in Fig. 4.22 the blue irreversible finger extends to slightly higher temperatures, demonstrating that pinning forces play a stronger role at matching fields. Further details about the

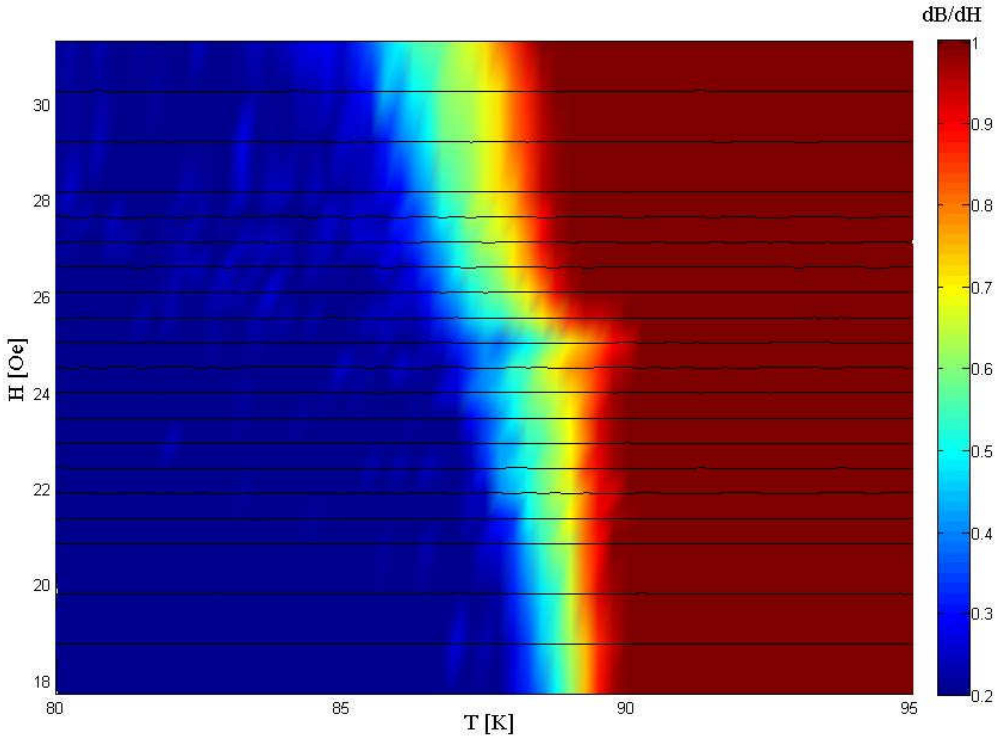

matching effect can be found in Ref. 35.

Fig. 4.22 Matching effect in $Bi_2Sr_2CaCu_2O_8$ sample using field modulation. Color represents *dB/dH*. At H_ϕ=25 Oe, enhanced irreversibility of vortex matter is distinguished. It agrees with the calculated B_ϕ=23.9 G.

The same kind of measurement in the pristine (not patterned) region visualizes another interesting effect called vortex melting. Theory predicts that rising the temperature will lead to increased thermal fluctuations, which lead to melting of the ordered lattice into a vortex liquid of mobile flux lines [60]. This melting transition is a thermodynamic first-order phase transition [58] associated with a loss of translational periodicity [62]. Quasi-ordered Abrikosov lattice turns into randomly fluctuating vortex liquid and the long range order is lost. This effect was measured for the first time in our lab in 1995 [62]. The melting transition will be explained more quantitatively in section 4.3.

The melting transition in Fig. 4.23 is seen as a dark red strip on a red background. The melting phase transition occurs in a region where vortex matter is reversible. The main reason for vortex irreversibility is the pinning force due to sample inhomogeneties, while the reason for vortex solidification below the melting line is the repulsive interaction between vortices [62]. The dark red color of the transition line indicates that vortex density jumps up at the transition, which is not the general case in molecular melting. H_2O is an example of molecular melting anomaly which exhibits higher density in liquid water phase than in solid ice phase like the vortex melting.

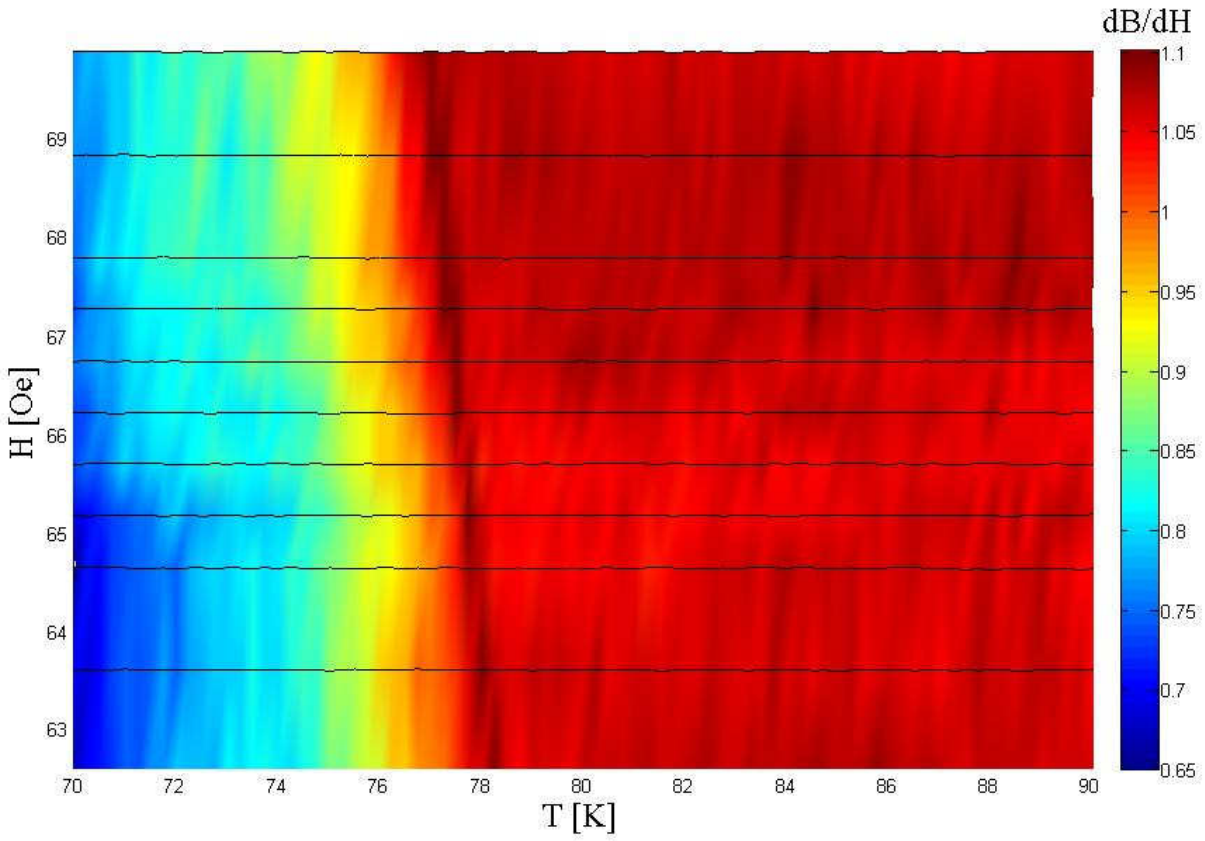

Fig. 4.23 Vortex melting in pristine region of $Bi_2Sr_2CaCu_2O_8$ seen here as dark red strip in red domain with *dB/dH>1*.

4.2.2 Edge and bulk flow by current modulation

Another interesting direction is observing vortex dynamics in the hole patterned region. This can be done by current modulation.

The pinning energy for the interstitial vortices is predicted to be weaker than that of the pinned vortices [63, 64], resulting in new heterogeneous phases of the vortex matter [65, 66]. Current modulation was already used in our lab [56,67] to resolve this new state of vortices called vortex nanoliquid. In presence of columnar defects it was found that current modulation is much more sensitive to vortices that are pinned by columnar defects and thus can detect a small amount of pinned (localized) vortices, while field modulation is sensitive mainly to the majority of mobile vortices which are delocalized in the nanoliquid state. This is because field modulation measures how many vortices enter/exit a region in response to an external modulation dH_z. This does not detect regions with pinned vortices above the depinning line of the interstitial vortices because any change in flux density can be achieved by a change in the number of

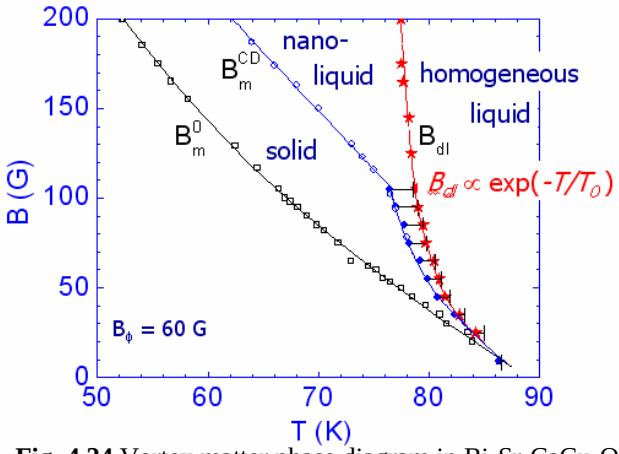

Fig. 4.24 Vortex matter phase diagram in $Bi_2Sr_2CaCu_2O_8$ with columnar defects taken from Ref. 56.

interstitials, which are fully mobile. However, pinning suppresses vortex motion, and thus suppresses dissipation of energy and as a result regions with columnar defects have higher critical current.

Figure 4.24 shows the various vortex phases in BSCCO with a low dose of columnar defects. The pristine melting line, B_m^0, is shown in Fig. 4.24 by the black line while the melting of the interstitial vortices in presence of columnar defects B_m^{CD} is shown by the blue line. The resulting nanoliquid phase consists of liquid droplets intercalated in a porous solid matrix of pinned vortices. Current modulation revealed the melting of this porous solid matrix into homogeneous liquid B_{dl}, shown by the red stars in Fig. 4.24. The theoretical fit [68,69] to the data, is shown by the red line in Fig. 4.24 and fits the experimental results.

As stated in the beginning of section 4.2, we investigate periodic surface holes. It will be interesting to apply current modulation to this kind of defects and see if similar results are obtained. D. Fuchs et al., [70] found that the B-L surface barriers for vortex penetration discussed in section 2 force the current to flow mainly at the edges of BSCCO crystals rather than uniformly in the bulk. The current flow can be divided into three modes shown schematically in Fig. 4.25. At low temperatures material disorder pins the vortices and prevents their motion, resulting in a finite critical current. In this case the transport current is expected to flow in a way similar to the case of the Meissner state where $B_{ac}(x)$ is expelled from the sample as shown in Mode (a). In the presence of significant surface barrier, the transport current flows at the edges of the sample as shown in Mode (b). Vortices enter and leave the superconductor at the edges, and the current drives the vortices over the barrier. In a highly dissipative state, the current is expected to flow uniformly across the sample as in a normal conductor, as shown in Mode (c).

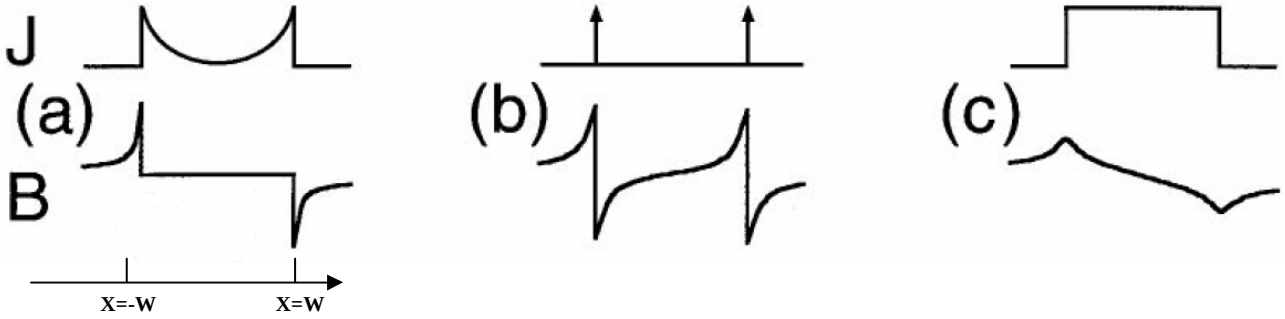

Fig. 4.25 Flow modes in $Bi_2Sr_2CaCu_2O_8$ sample. (a) Bulk pinning state dictates zero magnetic field change $B_{ac}=0$ in sample bulk. From inverse Bio Savart law this gives a current profile that has a maximal flow at the edges. (b) The main energy is required for vortices to overcome surface barrier for entering and exiting the sample, and thus current flows mainly at the edges. (c) Uniform current flow at elevated temperatures. Figure taken from Ref. 71.

In Fig. 4.26 the BSCCO sample is seen in a DMO measurement with current modulation dI=60 mA , T=77 K and H=82.2 Oe. The grayscale in every point of the image scales with *B(dI/2)-B(-dI/2)*. Let us denote here B_{SF}= *B(dI/2)-B(-dI/2)*. The contact locations are denoted by curved brown lines. The current flow directions in the sample bulk are shown by the orange arrows. The patterned region is seen as a square above the green rectangle.

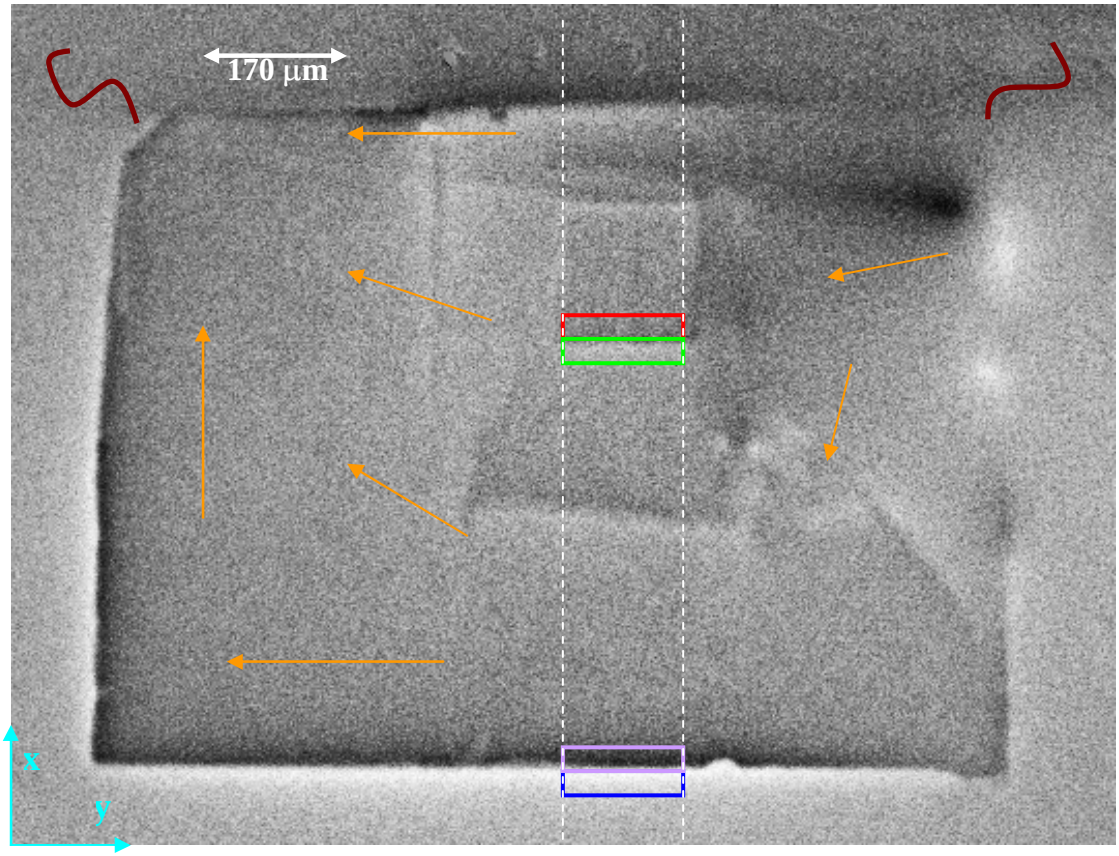

Fig. 4.26: DMO image with dI=60 mA, T=77 K and H=82.2 Oe. Red rectangle: inside patterned region at the lower edge of the region. Green rectangle: outside patterned region. Purple rectangle: inside the sample. Blue: outside the sample.

Figure 4.27 shows cross section near the edge of the sample for various temperatures integrated along the width of the strip marked by white dashed lines in Fig. 4.26. The three current flow modes in the figure are separated by two black dashed lines. It shows agreement with the current flow modes in Fig. 4.25.

The three current flow modes at the sample edges are shown in Fig. 4.28, integrated over the blue and purple rectangles regions in Fig. 4.26. The transition lines in T-H phase

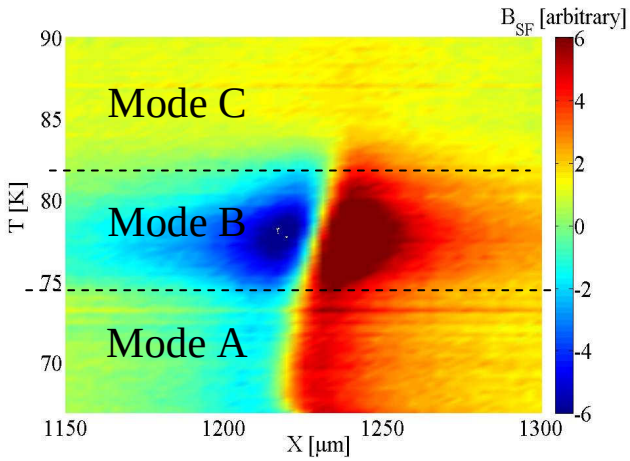

Fig. 4.27: Differential measurement with current modulation of dI=60mA. H_z= 46.9 Oe. Temperature scan is made and cross-section near sample edge is presented. Three flow regimes can be seen (two black lines show the separation between the regimes).

diagram between the modes show good agreement with the modes transition lines discovered by D. Fuchs in our lab in 1998 using arrays of Hall probes [71].

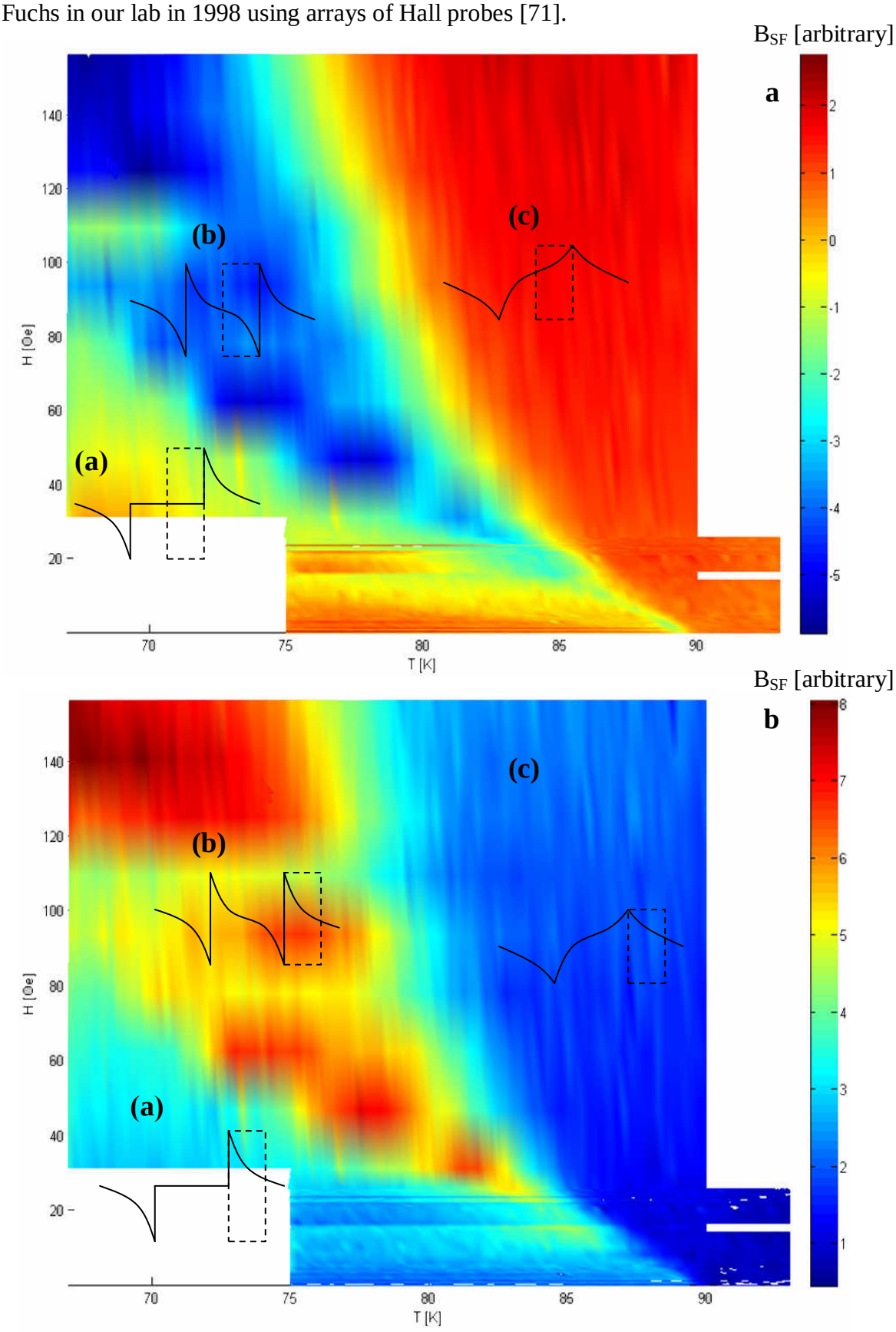

Fig. 4.28 Average B_{SF} measured near the edge of the sample, corresponding to the (a) purple and (b) blue regions in Fig. 4.26. The modes are illustrated on the corresponding phase regions, and the integrated region is marked by rectangle.

As expected, both figures 4.28 show the same location of transition lines between current modes. The modes in the figure are colored differently, and are accompanied by illustrations of the relevant modes with measured region marked with dashed rectangle. These are the modes (a), (b) and (c) from Fig. 4.25. In mode (c) in both figures B_{SF}= B(dI/2)-B(-dI/2)~2 which means that the edges of the sample are not seen. This agrees with the (c) profile – sample edge does not change the sign of the self field. In mode (b) Fig. 4.28a shows B_{SF}=-6 while Fig. 4.28b shows B_{SF}=6, which demonstrates an edge flow of the current according to Fig. 4.25. Finally in mode (a) Fig. 4.28a shows B_{SF}=0 inside the sample while Fig. 4.28b shows B_{SF}=-3 outside. This corresponds to the bulk pinning mode (a) in Fig. 4.25.

Let us examine now the current flow modes at the edges of the patterned region. One would expect some level of similarity to the result of D. Fuchs et al., [70], because there would be a barrier for vortex entrance to the patterned region made by the repulsive interaction with the vortices already pinned by a hole. The pinned and the high dissipative states are also expected to be reproduces inside the patterned region.

The strip between the white dashed lines in Fig. 4.26 was integrated, and line scans like Fig. 4.29a were obtained for various T and H values during T scan. Figure 4.29a shows a *T* scan with *I* modulation for H_z=78.2 Oe. Three flow regimes are resolved and separated by the black dashed lines. Figures 4.29 (b), (c) and (d) show three representative current profiles, one from each regime. Regime 1 is a low temperature regime where B_{SF} =0 inside the patterned region. Regime 2 is an intermediate temperature in which flow concentrates at the edges of the patterned region. Regime 3 is present at high temperatures and corresponds to homogeneous flow in the patterned region which seems to be reduced comparing to the flow in pristine region.

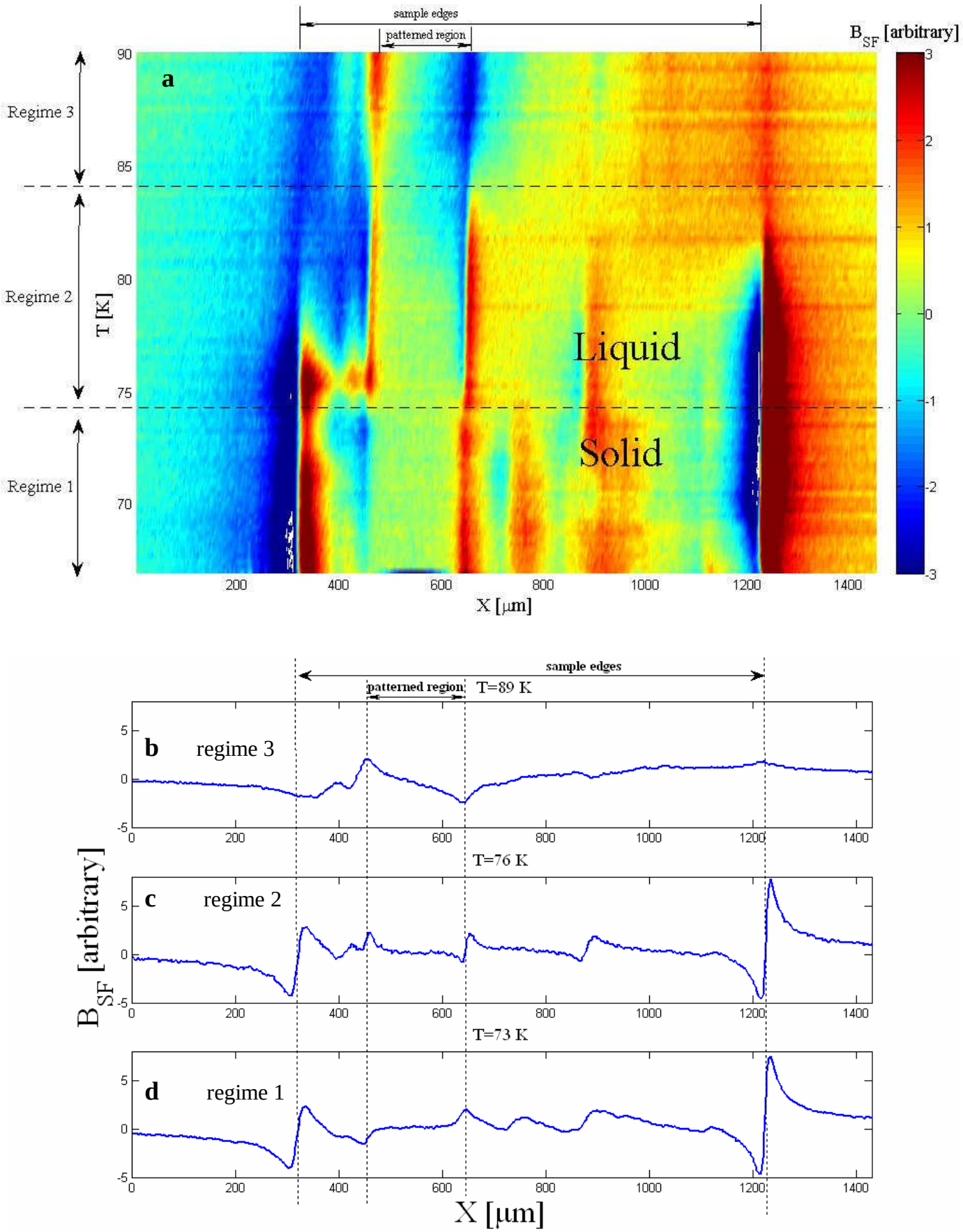

Fig. 4.29 (a) Differential measurement with current modulation of dI=60mA. H_z= 78.2 Oe during temperature scan. Three flow regimes can be seen (two black dashed lines show the separation between the regimes). A representative of each regime is presented: (b) regime 3, (c) regime 2, (d) regime 1. Patterned region edges and sample edges are shown denoted by dotted lines. Profiles are evaraged over region between dotted lines in Fig. 4.26.

Regime 1 in Fig. 4.29 is similar to the bulk pinning mode Fig. 4.25 (a). Inside the patterned region there is zero differential field because strong vortex pinning by holes occurs. Regime 2 is the regime where vortices have a barrier to enter the patterned region because of repulsive interaction with the pinned vortices, thus the current behaves like with surface barriers in mode (b). Regime 3 is similar to the uniform flow in Fig. 4.25 (c) except for one interesting detail; current direction seems to be reversed.

A way to understand the reversed current is that the uniform current density in the patterned region is less than in the pristine region, resulting in a relative negative flow. The reason may be that for high temperatures the patterned region has induced resisitivity because of reduced conduction material. Thus, at elevated and low temperatures holes play the opposite role. At low temperatures they lower resistivity of the patterned region by pinning the vortices, while at elevated temperature they raise the resistivity by reducing the conduction material. Interestingly, a similar behavior was reported in our lab in the PhD thesis of Dr. Alex Soibel 2001 [72]. He found that at low temperatures current is attracted to a defect in the crystal and exhibits enhanced flow, while close T_c, both above and below T_c, current avoids the defect.

Let us discuss the differences between regime 2 and regime 3. In regime 2 all pinning sites are occupied, and thus vortices that enter the patterned region experience a repulsive force. This behavior is of the same physical nature as was discussed in section 4.2.1 and plotted in Fig. 4.22. In Fig. 4.27 at T>84 K there are no barriers for vortex penetration and the current flow is homogeneous. We conclude that in this regime vortices are delocalized and no longer pinned. Thus the transition line from regime 2 to regime 3 is the delocalization line transition where a nano-liquid state melts into homogeneous liquid.

We now find the transition lines change over T-H phase diagram between the three flow regimes. The green and red rectangles in Fig. 4.26 are the regions over which signal is averaged.

In Fig. 4.30 self field measurements from current modulation obtained near the inner side of the patterned region (red rectangle in Fig. 4.26) are presented. If we look at Fig. 4.29 (a), we will see that measuring near the inner side of the patterned region located at sample coordinate=640 μm will reveal the starting point of the blue strip. Thus Figure 4.30 shows the transition line between regimes 1 and 2. The transition is colored by the green color, where B_{SF}=0.

The black dashed line shows the pristine melting line measured by field modulation dH=1 Oe in a pristine region of the sample close to the patterned region. These two lines agree. Thus we conclude that the transition between regimes 1 and 2 is the pristine melting line. This result will be explained later following Fig. 4.32.

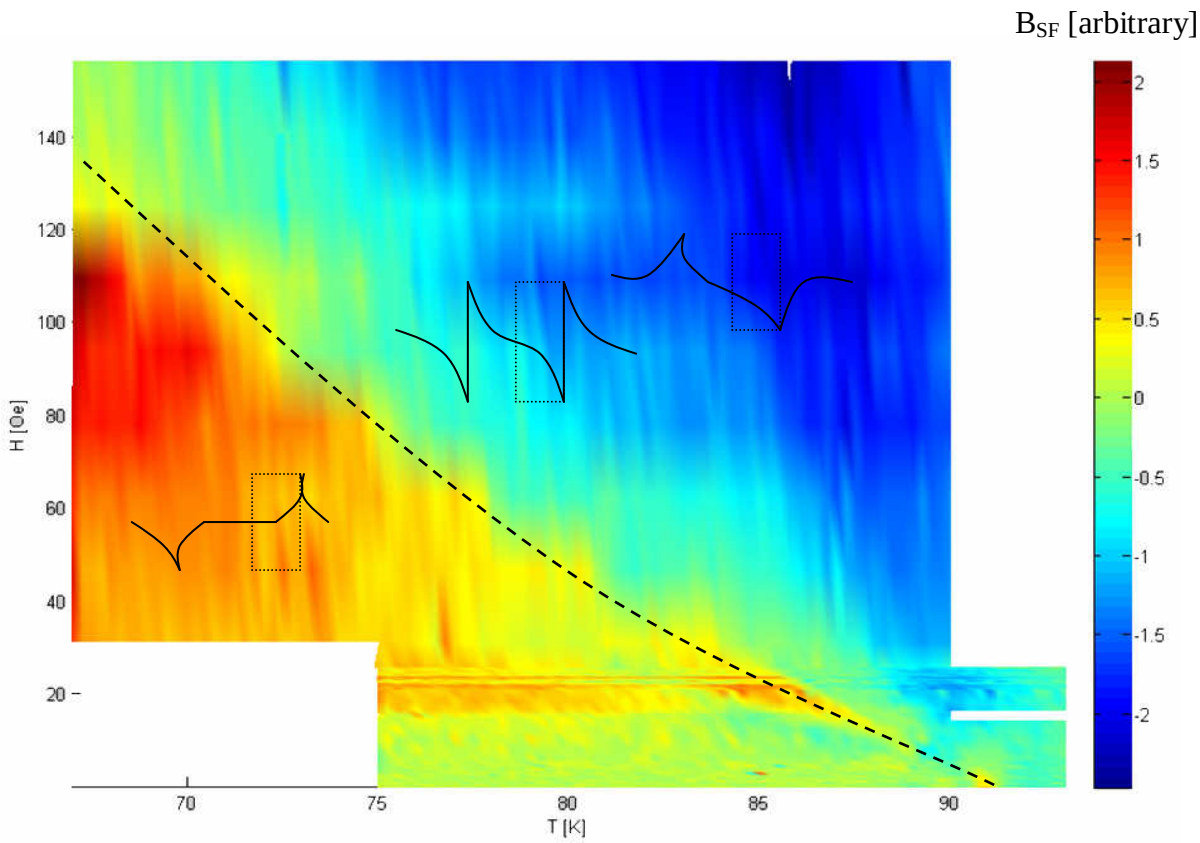

Fig. 4.30: Measurement near the inner edge of the patterned region. The transition between regimes 1 and 2 is seen while B_{SF} turns from positive to negative indicating the transition line between the regimes at B_{SF}=0 colored here by green-yellow. Pristine melting line is marked by the black dashed line. An agreement between the two lines can be seen. The steps in the green transition line are seen because the discreteness of H which was measured in steps of 15 Oe.

In Fig. 4.31 the same kind of measurement outside the patterned region (green rectangle in Fig. 4.25) is introduced. If we look again at Fig. 4.29a, we will see that measurement right to sample coordinate 640 μm will demonstrate the place where the red strip appears. Thus it visualizes the transition between regimes 2 and 3.

This transition as discussed before may be similar to the vortex delocalization line introduced by S. Banerjee [56,67] and shown in Fig. 4.24 as B_{dl}. When vortices delocalize from the surface holes, the barrier disappears and uniform flow begins. The functional dependence of the delocalization line looks similar to Fig. 4.24 even quantitatively. Both lines reach the value H=150 Oe around T=80 K. The transition line in Fig. 4.28 seems to be exponential obeying the same behavior of $e^{-\frac{T}{T_0}}$ as the result of S. Banerjee. The homogeneous liquid state looks differently in our measurements compared to S. Banerjee because heavy Pb ions do not introduce reduced conductive material while surface holes do introduce. For this reason in his measurements the patterned region was not resolved in the homogeneous liquid state while in our measurements it is resolved.

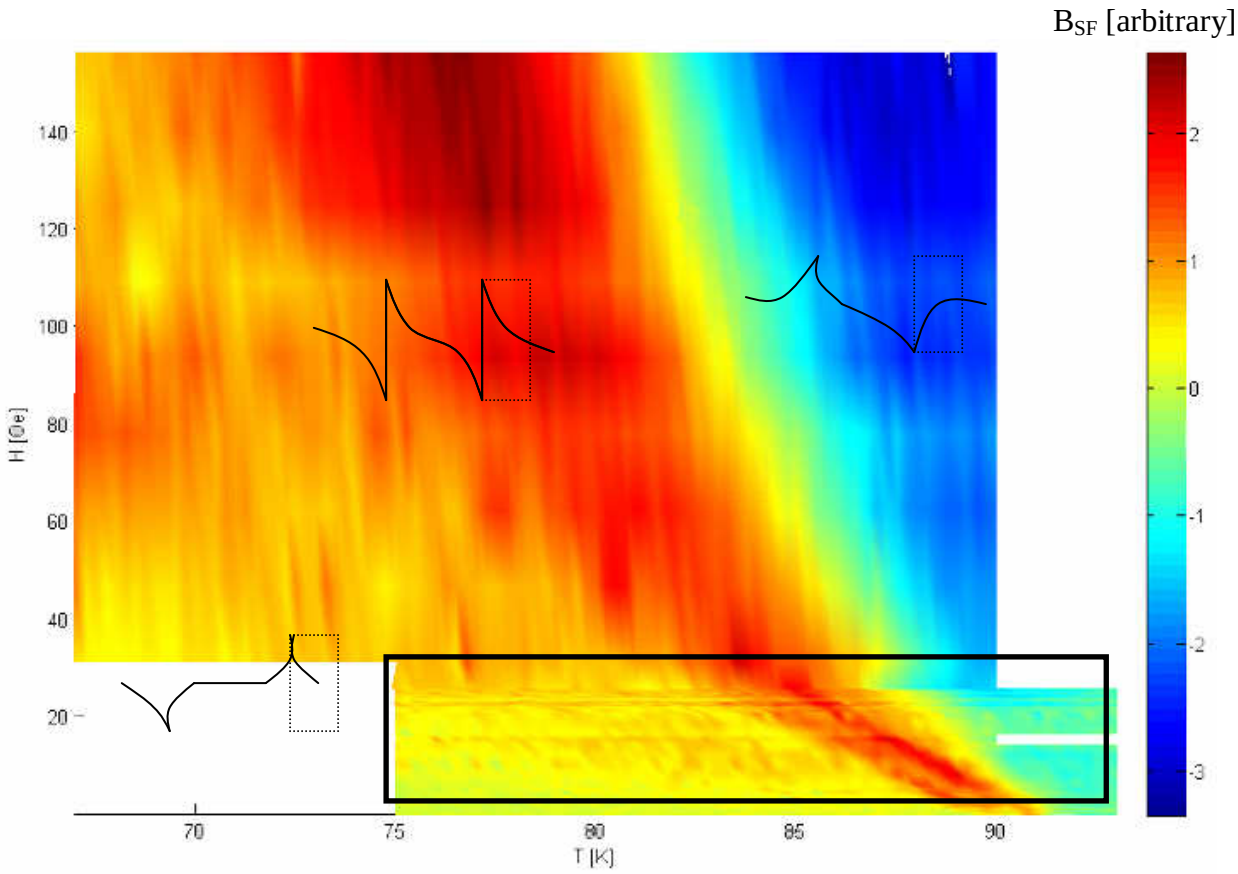

Fig. 4.31 Measurement averaged over the green rectangle in the sample marked in Fig. 4.26 outside the patterned region. The red colored region is regime 2 where current flows at the edges of the patterned region and it is identified as a nanoliquid phase. The blue colored region is regime 3 where a homogeneous current flow in vortex liquid phase occurs. The red strip in the black rectangle region indicates the melting line.

Let us now focus on the area in the phase diagram of Fig. 4.31 inside the black rectangle. A clear red strip can be distinguished. Figure 4.32 (a) shows a zoomed view of the region marked by the black rectangle in Fig. 4.31. Figure 4.32 (b) is field modulation measurement dH_z=1 Oe of a pristine area in the sample near the patterned area. The lines in the two figures clearly coincide, which suggests that the red line in Fig. 4.32 (a) corresponds also to the melting line inside the patterned region. It is visualized by current modulation for the same reason as the results in section 4.1 were visualized, see Fig. 4.9. This result remarkably agrees with the result obtained by S. Goldberg in Ref. 35. She succeeded to visualize melting in the patterned region by shaking method, and it appeared to be located at the same temperatures and fields as the pristine melting line T_m.

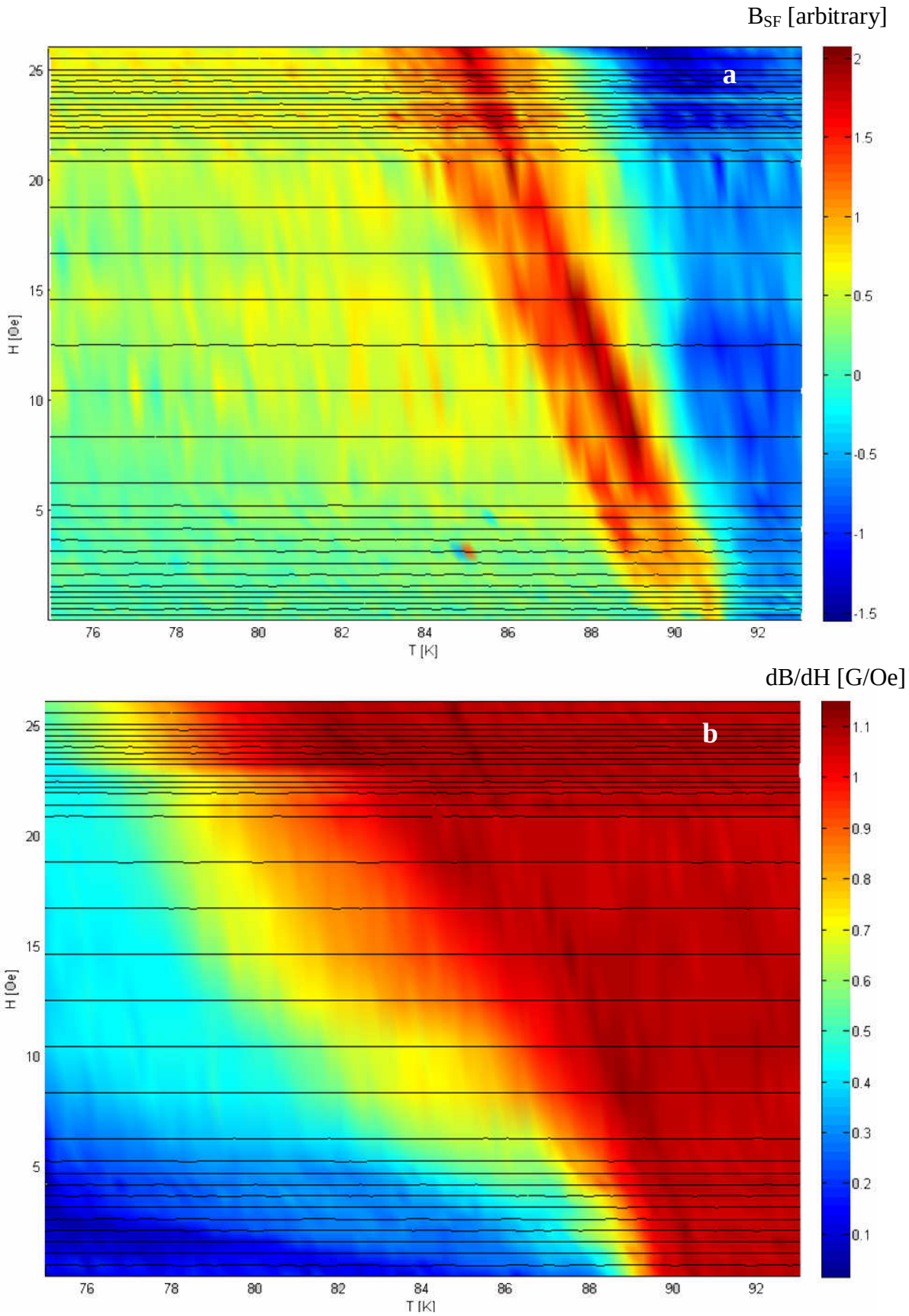

Fig. 4.32 Melting line for low H fields. (a) Current modulation visualization of melting line (red) inside the patterned region. (b) H modulation visualization of melting as dark red line in the pristine region. These two lines clearly coincide confirming the same agreement discusses in Ref. 35. In this Ref., patterned region melting line was detected by shaking rather than by current modulation.

Now we will try to explain why the melting line coincides with the onset of current flow at edges of the patterned region. Multiterminal flux transformer measurements made in our group [73] and Corbino disk geometry measurements [74] on BSCCO revealed that the melting and *c*-axis decoupling transitions occur simultaneously at a sublimation transition of the vortex lattice.

Thus below T_m, surface holes pin the whole 3d stack of coupled pancake vortices. Pinned 3d stacks in the patterned region make the pristine 3d stacks entrance more difficult. However above T_m only surface 2d pancakes are pined by the holes. Holes pin 2d pancakes much weaker than they pin the whole 3d coupled stack of pancakes, and as a result bulk pinning is lowered increasing the relative importance of edge pinning. As a result, above T_m 2d pancake entrance into the patterned region is enhanced and the onset of current edge flow drives the 2d pancake vortices into the patterned region helping pancakes to overcome the edge barrier of the patterned region. The edge barrier raises from the repelling 2d pinned pancakes. Thus, the delocalization line, in Fig. 4.31, is the delocalization of 2d pancakes from surface holes.

Concluding, three regimes of current flow are identified in the patterned region. This indicates three corresponding regimes in vortex arrangement. In the lowest temperature regime, 3d stacks of pancake vortices are pinned in the patterned region (seen by enhanced current flow compared to pristine region flow). In the pristine region vortices are also in a solid phase, and as a result pristine vortex lattice is pinned in the a-b and correlated in the c direction in the pristine region and thus vortex flow is suppressed because of enhanced pristine pinning [75]. In the intermediate temperature regime both the pristine and the patterned regions are liquid. Mobility in the pristine region is enhanced while the bulk pinning is reduced both in the patterned and pristine region as a result of c-axis decoupling of pancakes. Thus edge effects of the patterned region begin to play more important role in this regime, and this results in current edge flow. In the high temperature regime, 2d pancakes delocalize from the surface holes and all vortices are in a liquid phase, giving rise to homogeneous flow which is slightly reduced in the patterned region due to reduced conducting matter. The T-H range of the transition from nanoliquid to homogeneous liquid is close to the one obtained in BSCCO irradiated with columnar defects (see Fig. 4.24).

These results are intriguing. Further flux transformer measurements of BSCCO samples patterned with surface holes are needed in order to confirm that in the liquid phase bulk pancakes penetrate into the patterned region while surface pancakes are pinned by holes. To obtain quantitative values of current, it is possible to perform a current-inversion calculation, as suggested in Refs. 31,76-78. Current inversion analysis to the measurements presented above can provide better understanding to the resolved flow regimes. This will give a more quantitative understanding of the vortex scenarios which were explained in this section.

4.3 Long range order examination with novel Bragg Magneto Optics

The experimental *B*-*T* phase diagram of the mixed state in a clean BSCCO sample is shown schematically in Fig. 4.33. The diagram can be understood in terms of these three different energy scales mentioned previously in this work [79,80]: E_{el} is the elastic energy keeping the vortices near their equilibrium positions in the lattice (see introduction and Figs. 1.4 and 1.5), E_T is the energy of thermal fluctuations (see section 4.2.1 and Figs. 4.23 and 4.32), and E_{pin} is the pinning energy due to material disorder (see section 2.3.2 and Fig. 2.10). The diagram is divided into three main vortex matter phases, each corresponding to a different dominating energy.

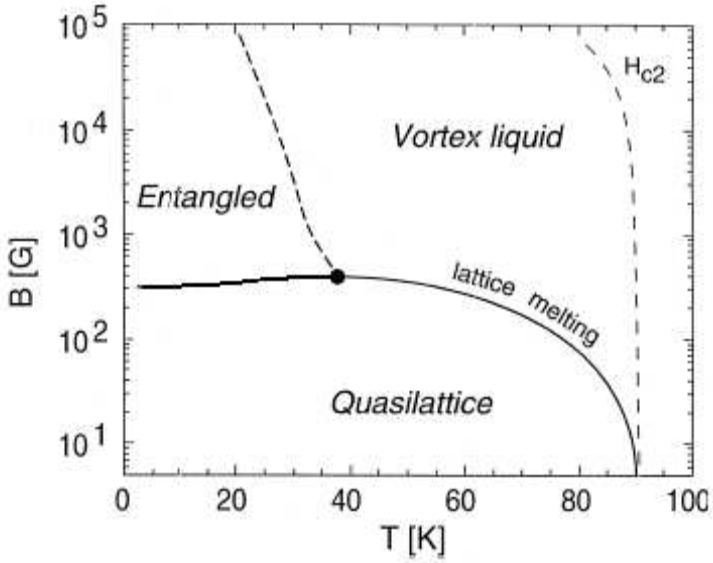

Fig. 4.33 Phase diagram of three phases due to three energies. Remark: more recent phase diagram [81] separates quasilattice into two phases: Low temperature Bragg Glass phase and high temperature lattice phase. Bragg Glass melts into entangled phase under inverse melting process [3].

The lattice melting was observed experimentally and is a first order transition in clean samples [62], as was seen also in this work in Figs. 4.23 and 4.32. Recently, it was shown that the quasilattice to entangled solid transition is also a first-order transition [3]. There has also been evidence of a second-order transition from the entangled phase to the liquid phase, when $E_{pin} = E_T$ [81].

In section 3.2, we introduced the Novel Bragg MO system which aims to measure optical diffraction from vortex matter. From the diffraction pattern, it is possible to deduce the average lattice period, its orientation relative to the sample edges and vortex long range order. This tool could provide an additional way of detecting phase transitions, utilizing changes in the long-range order of the vortex lattice rather than the transport and magnetization measurements that are standard in our lab. For instance, the quasi-ordered phase has no dislocations and the orientational LRO is preserved with power law correlations, resulting in Bragg peaks [82,83] in neutron diffraction experiments. Neutron scattering in BSCCO has indicated that there is structural change in LRO of the VM in the vicinity of the solid-liquid transition [84]. Weak point disorder produces displacements at short length scales, but retains quasi long-range order [85-87]. The correlation function of vortex displacement can scale with distance [88,89] as a constant, power law or exponentially, defining LRO, quasi LRO, and short range order respectively.

While neutron diffraction techniques [84] also measure order of the vortex lattice directly, using visible light is more convenient experimentally, because neutron diffraction requires an accelerator. However neutron diffraction can measure with better resolution, diffracting from vortex lattice with a lattice constant much lower that 0.5 μm which is the limit of visible light. The main advantage of Bragg-MO system is its potential to measure lattice structure instantly, allowing measurements in the presence of transport. This would be a local tool for studying vortex dynamics, as opposed to thermodynamics.

The many interesting questions that may be studied with a direct probe of LRO based on magneto-optics, and the limited experimental results of the existing tools that measure LRO of vortex matter, provide motivation for the new Bragg-MO setup.

In this chapter we will briefly summarize the experimental work using Bragg-MO. Sections 4.3.1 and 4.3.2 deal with the process of signal/noise improvement of the existing Bragg-MO setup, while sections 4.3.3-4.3.5 focus on the physical measurements what were carried out.

4.3.1 Reducing noise

Our goal was to improve the signal-to-noise ratio which compares the level of a desired magnetic signal to the level of background noise originating from scattered light and from mechanical, optical or thermal fluctuations. In the beginning of this research, it was assumed that the different transverse modes of the laser beam cause speckles in the diffracted image and thus reduce S/N. Therefore, removing all the modes except the Gaussian mode was expected to improve the S/N. For this purpose a fiber optic spatial filter was added to the system. However the signal to noise ratio remained the same.

Then the system was tested by removing every optical item and comparing how this item changes the S/N. Evidently, every optical item added some noise which together gave a high noise level. It was realized that the source of the noise is from the fact that laser light is coherent, and thus is sensitive to mechanical movements on a scale comparable to the wavelength of the green light (0.5 μm). All the fringes from the various optical components, produced by the coherence of the light, perform large movements determined by the size and dimensions of each optical component. In Fig. 4.34 a magnified image of zero-order reflected beam is shown. Each ring is a diffraction fringe from different optical component.

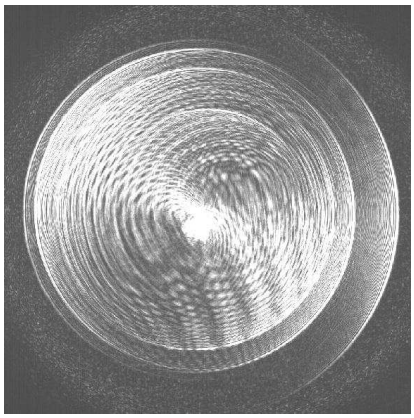

Fig. 4.34: Magnified view at zero order laser diffraction peak

4.3.2 Increasing and testing magnetic signal

We were not able to visualize diffraction from SC samples. The following work was done to improve the strength of the signal. The main challenge in any optical system is to improve the resolution by increasing the S/N.

Obtaining the needed sample-MOI proximity for single vortex resolution is not a simple task. Until now only two groups, one in Oslo [90] and one in Japan [91], succeeded to visualize single vortices in $NbSe_2$ crystals using the MO method.

As was discussed in section 2, the magneto optical signal measured by the MO-Bragg setup is a local rotation in the polarization of the reflected light. Carneiro and Brandt [92] showed that the field from a vortex can be approximated by a magnetic monopole of charge $2\phi_0$ (flux quanta) and positioned at $z_0 = -1.27\lambda$, however calculations [92] show that the field modulation of a periodic vortex lattice decays exponentially with z. Therefore Bragg diffraction will be generated mainly in the lower part of the MOI that is closest to the sample surface and closest possible proximity between the MOI and the sample is required. To obtain this proximity, a crystal with very flat surface is needed so that the crystal-MOI gap will be small. This proximity is examined by monitoring Newton rings while adjusting the pressure between the sample and the MOI, using MOI without a mirror.

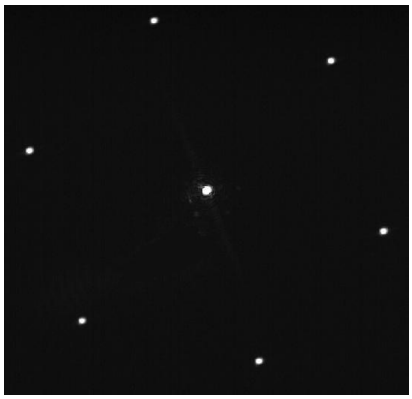

Fig. 4.35 Optical diffraction peaks from surface holes with inter-distance of 1μm. Reducing the distance between holes will increase the distance between the peaks.

The distance between sample surface and MOI is crucial in obtaining strong signal. The physical reason is that the EM field propagator in vacuum obeys the Laplace equation. This equation gives sharp decay, much stronger than optical signal decay. And indeed, all the orders of optical diffraction peaks from periodic surface holes patterned on BSCCO sample were clearly observed, as shown in Fig. 4.35. This result demonstrates that the optical construction of the system achieves the requirement to measure Bragg peaks for strong enough signals. Thus the only challenge in obtaining MO diffraction is to increase the magnetic signal strength.

Different samples were selected and measured, both $NbSe_2$ and BSSCO with different surface properties and quality. Different types of MOI were also tried. Mirrored (evaporated layer of Al on the indicator) and not mirrored MOI were examined. Mirrored MOI has higher distance between the sample and MO layer, but reflects the laser beam and thus makes the signal stronger. Not mirrored

MOI, however, has the advantage of closer proximity to the sample. Indicators with different thickness of MO layer were tested. For the conventional MO setup, we use thick indicators, since the spatial-averaged MO signal does not change much as a function of height at our spatial resolution and any additional thickness gives a larger rotation according to Eq. 4.15. However for the Bragg-MO (or for single vortex imaging), a thicker indicator means adding the averaged signal to the periodic modulation. This could transfer spectral weight into the zero order of the diffraction, or lead to a worse signal/noise ratio in real space since the larger background of constant light could not be cancelled exactly by the exit polarizer. The best signal/noise MOI were chosen. Indicators from different manufacturers where also tested, as seen in Fig. 4.36.

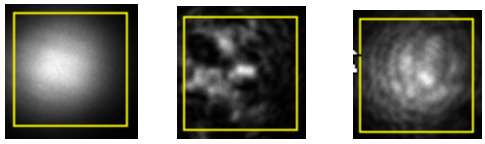

Fig. 4.36 Beam transmission through different indicators. Left: direct beam 100%. Middle: Indicator with 11.7% transmission. Right: Indicator from a different manufacturer with 39.6% transmission but worse quality.

Low transmission of indicator means that it will be heated and will heat the sample. We have faced this problem while trying to cool $NbSe_2$ with liquid He_4 below T_c= 7K. In this case, low laser intensity and maximally transparent indicator were needed to reach the sample superconducting phase.

Theoretical calculations [92,93] and the simulation program of E. Brandt from Max Plank institute were also used to calculate the signal drop from vortices as a function of distance from the sample surface. Figure 4.37 presents a calculation of the signal above a lattice of vortices taking the distance between vortices a=2 μm, so that the field is $B = 5\ G$.

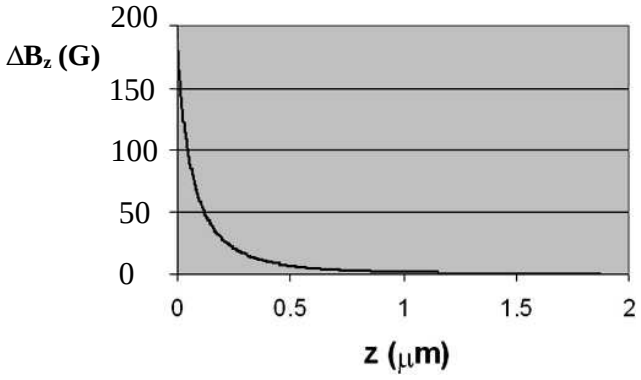

Fig. 4.37 Field modulation intensity from the vortex lattice vs. height above the surface of $NbSe_2$ for inter-vortex distance of a_0=2 μm.

The signal is defined as a difference in B_z between a position R_1 above the center of a vortex and at R_2 halfway between vortices. Hence we define the $\Delta B_z(z) = B_z(R_1,z)-B_z(R_2,z)$ where z is the measured distance from the $NbSe_2$ surface.

A distance of 0.5μm above the sample surface, which is comparable with a vortex lattice constant, will provide only about 7% of the signal. We can see this in a more visual way by the simulation of E. Brandt that makes an iteration procedure of G-L Eq. 1.1 [93], where 3D GL solution of ideal vortex lattices for any induction and symmetry is given. Figure 4.38 presents the magnetic signal from a vortex lattice measured at heights of z=0.1, 0.5 and 1.25 μm above the surface. As can be seen, in Fig. 4.38 (b) the field modulation is 10 G while the average field is 5 G.

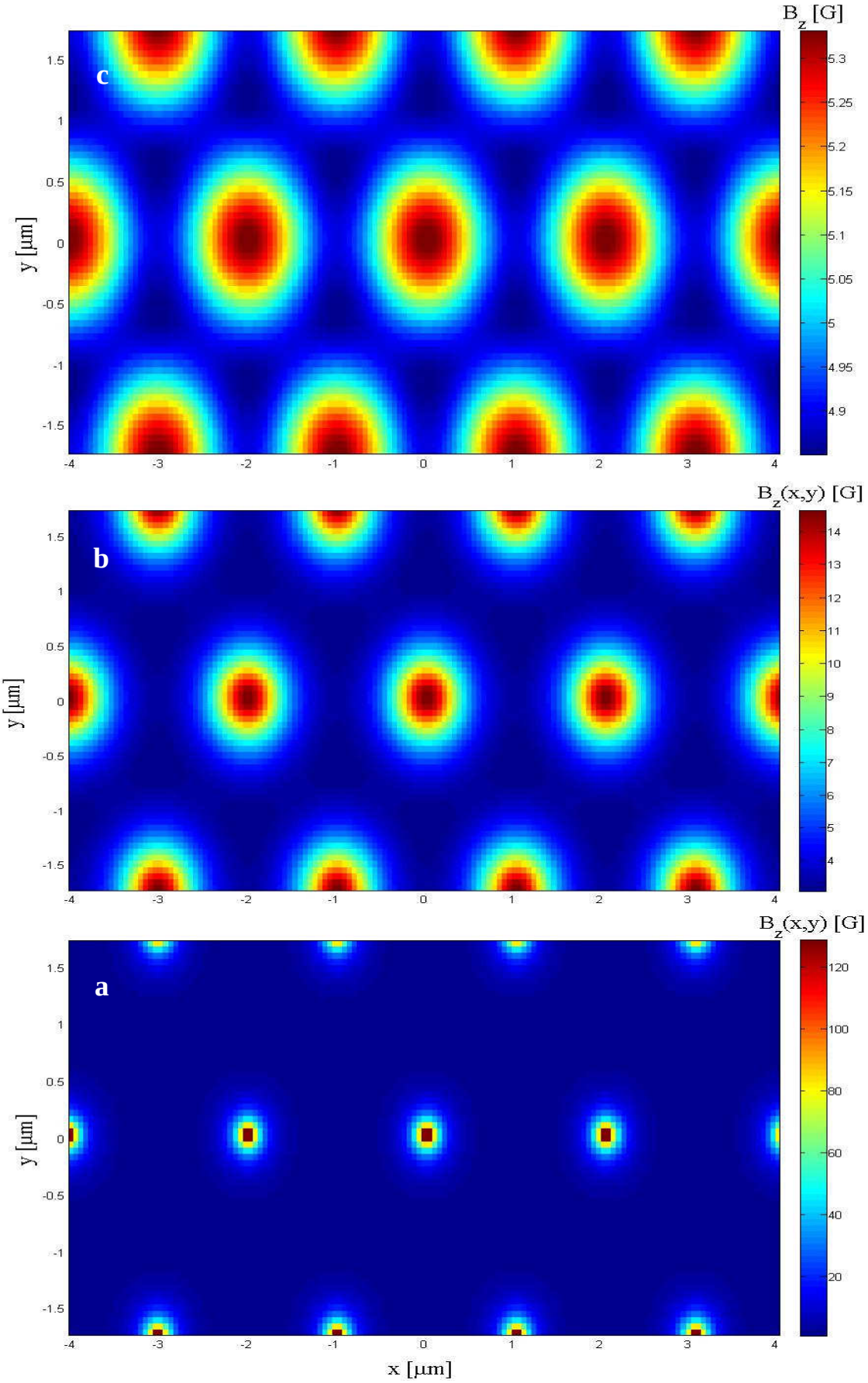

Fig. 4.38 $B_z(x,y)$ above vortex lattice with lattice constant a_0 =2 μm which corresponds to H_z=5 G and sample thickness d=20 μm at a height of (a) z=0.1 μm , (b) z=0.5 μm and (c) z=1.25 μm above the surface.

4.3.3 Flux penetration in $NbSe_2$ and $Bi_2Sr_2CaCu_2O_8$ crystals

The following measurements demonstrate that the zero-order reflection of the Bragg MO can be used to locate the penetration field H_p and H_{irr} of different superconducting samples. Two crystals were measured: BSCCO and $NbSe_2$ with T_c = 92.0 K and 7 K respectively.

Beam intensity measurements which are proportional to magnetic field B on the sample surface were taken. In general the reflected beam intensity is proportional to B^2. However if the measurement is not performed while the polarizations of the two polarizers are crossed, the dependence is approximately linear. We also did differential measurements with field modulation.

In this section the reflected beam intensity was not converted into field values, since the important information here is only the transition temperature between different vortex states. In sections 4.3.4 and 4.3.5 the beam intensity was converted into a field. Figure 4.35 presents differential measurements with field modulation upon increasing and decreasing temperature. The sharp drop in the signal indicates the irreversibility temperature T_{irr}.

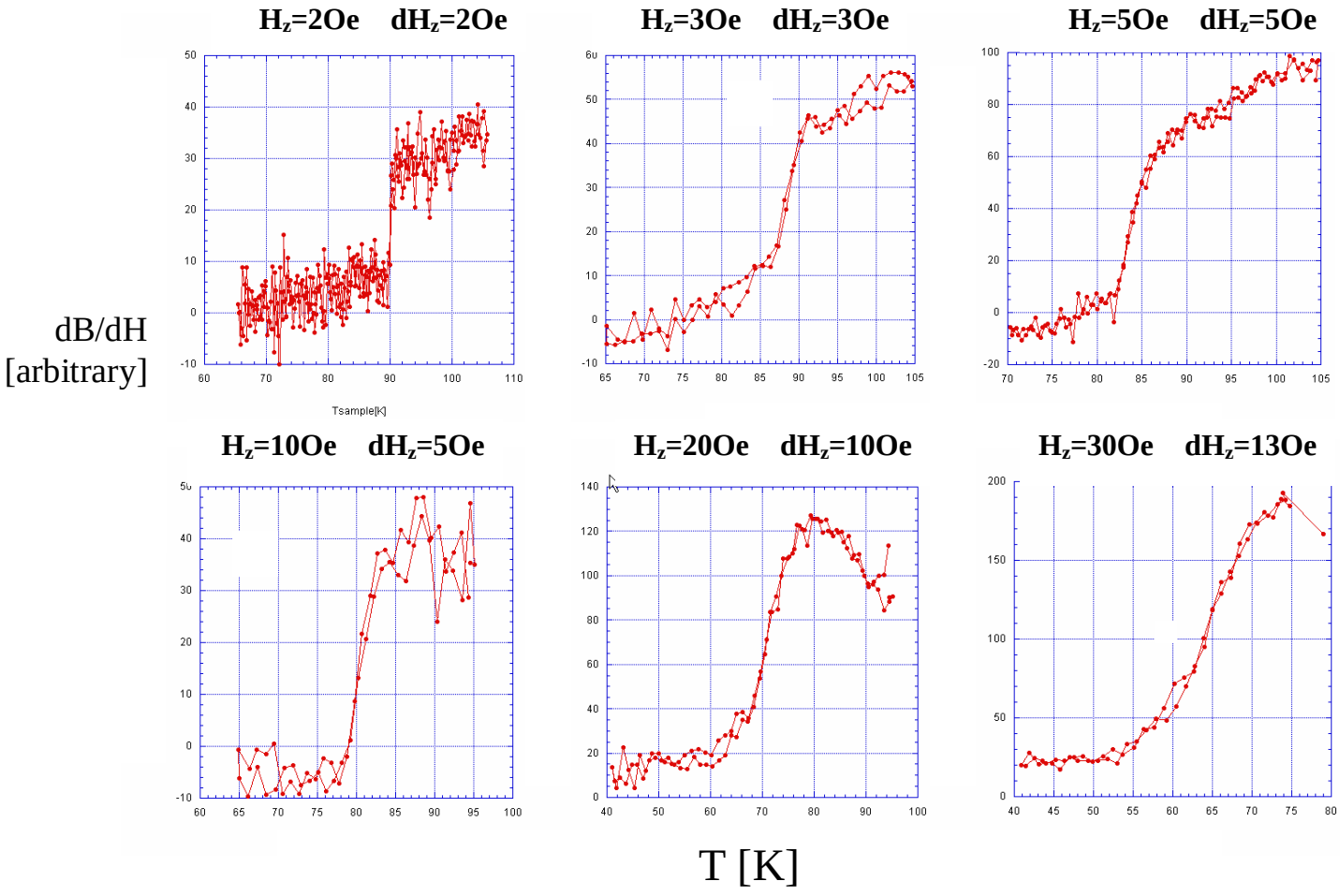

Fig. 4.39: Irreversibility temperature in $Bi_2Sr_2CaCu_2O_8$ samples obtained by field modulation during T scan. The different plots show sharp drop in dB/dH indicating T_{irr} for different values of H_z and dH_z.

Figure 4.40 presents the resulting irreversibility line $H_{irr}(T)$.

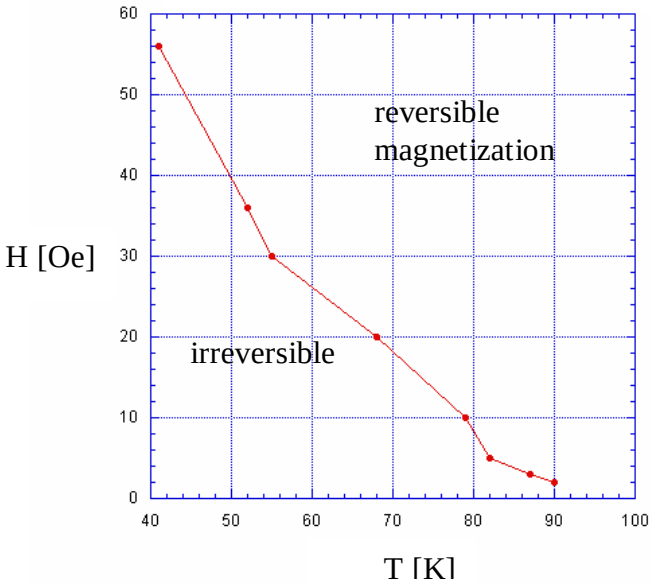

Fig. 4.40: Vortex penetration line for $Bi_2Sr_2CaCu_2O_8$ in the H-T phase diagram

Now let us look at irreversibility in $NbSe_2$ crystals, as shown in Fig. 4.42.

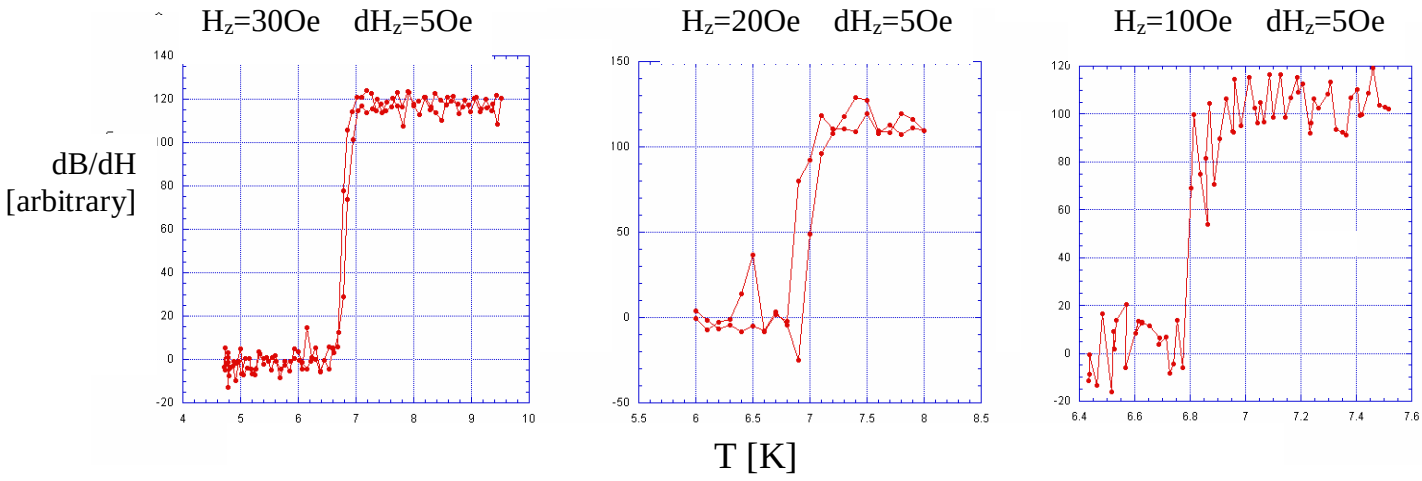

Fig. 4.42: T scans with H modulation in $NbSe_2$ samples showing irreversibility onset.

It is evident from Fig. 4.42 that at low fields in $NbSe_2$ irreversibility occurs roughly at the same temperature for all H.

4.3.4. Hysteresis in $NbSe_2$ and $Bi_2Sr_2CaCu_2O_8$ samples

Using the zero order of the Bragg-MO diffraction pattern, we measured the irreversibility line H_{irr} (T) of SC samples.

In Fig. 4.43, increasing and decreasing H scans on $NbSe_2$ show that the penetration field is H_p=20 Oe and the reversibility onset field is H_{irr}=45 Oe. Similar measurement on BSCCO is presented in Fig. 4.44. In Fig 4.44 (a) H_p=40 Oe and H_{irr}=110 Oe, while in Fig. 4.44 (b) H_p=30 Oe and the hysteresis is present up to 120 Oe.

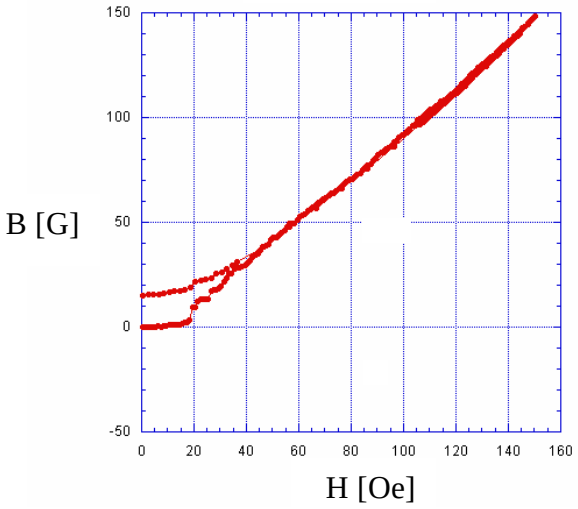

Fig. 4.43: Magnetization loop in $NbSe_2$ performed at T=6.5K.

In Fig. 4.45 dc local magnetization loops were carried out showing B on the left and B-H on the right. The same theoretical behavior shown in Fig. 2.4 can be observed here experimentally in Fig. 4.45 for $NbSe_2$.

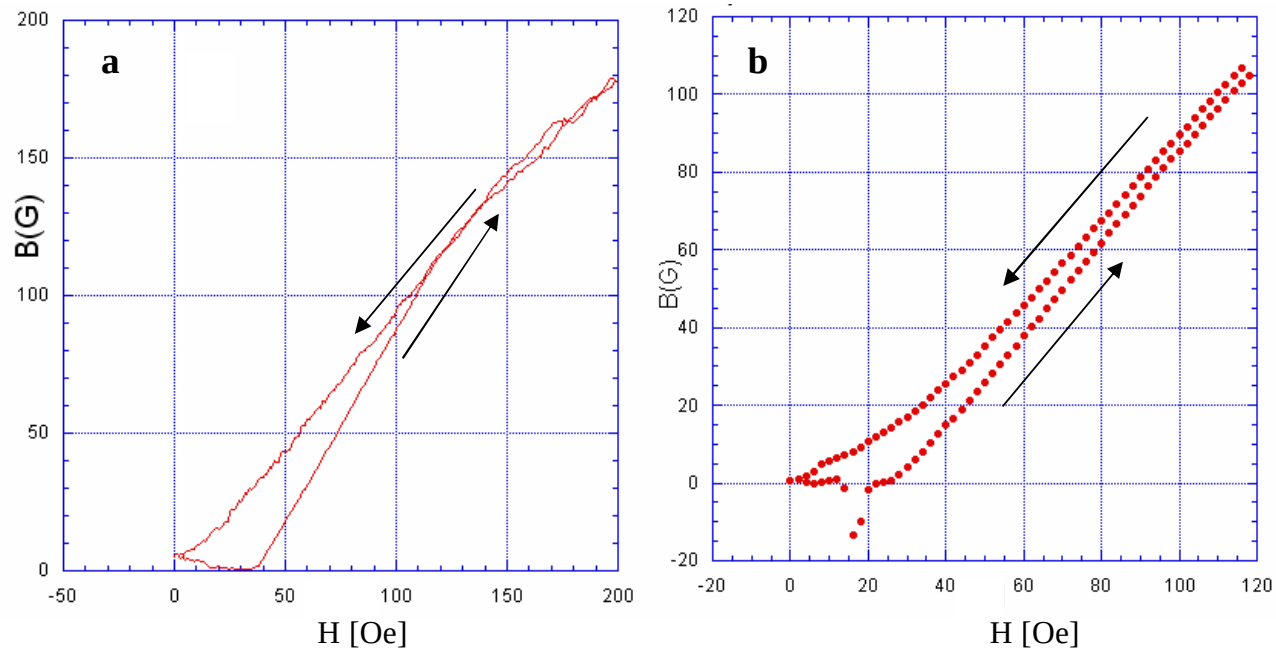

Fig. 4.44: Magnetization loops in $Bi_2Sr_2CaCu_2O_8$ crystals performed at (a) T=52 K (b) T=64 K.

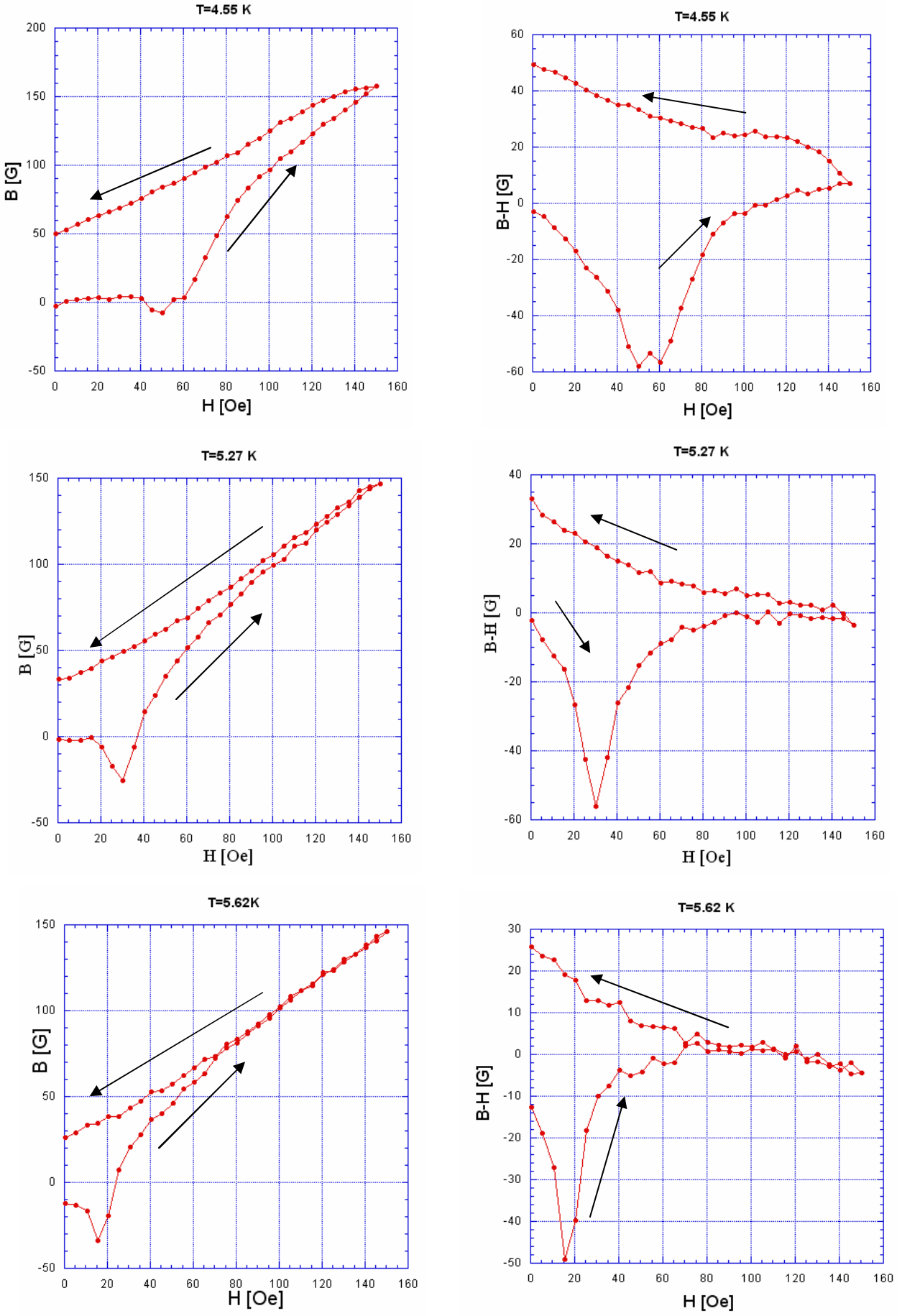

Fig. 4.45: Magnetization loops in $NbSe_2$ crystals performed at various temperatures. The curves on the left show B while curves on the right show B-H.

4.3.5. Verification of Bean model

Using the zero order of the Bragg MO setup, we measured magnetization loops. In Fig. 4.46 the four steps described in the Bean model in section 2.3.2 are measured clearly both in BSCCO and $NbSe_2$ samples. The four different types of curve behavior in Fig. 4.46 are marked by numbers 1-4. As mentioned before, all the measurements in this section are done by laser, with spot diameter about 1/4 of the sample width. Let us assume that the beam reaches the sample near its edge. Thus the measured signal in our measurement should be proportional to $\int_{-W}^{-y} dxB(x)$ where $B(x)$ is given by Fig. 2.11 and y~W/2. When H is raised, B will remain zero until H_p is reached. This corresponds to type 1 curve. Type 2 curve shows vortex gradual penetration into the bulk with a constant slope as seen in Fig. 2.11 (a). When H is swept down, flux begins to exit from the sample edges, not covering yet the whole integrated region covered by the beam. Curve 4 starts when the triangular profile of exiting flux arrives to the point y of the sample where the integration region ends. From this point B(x) is decreased in the whole integrated region, so the decrease of B is much stronger.

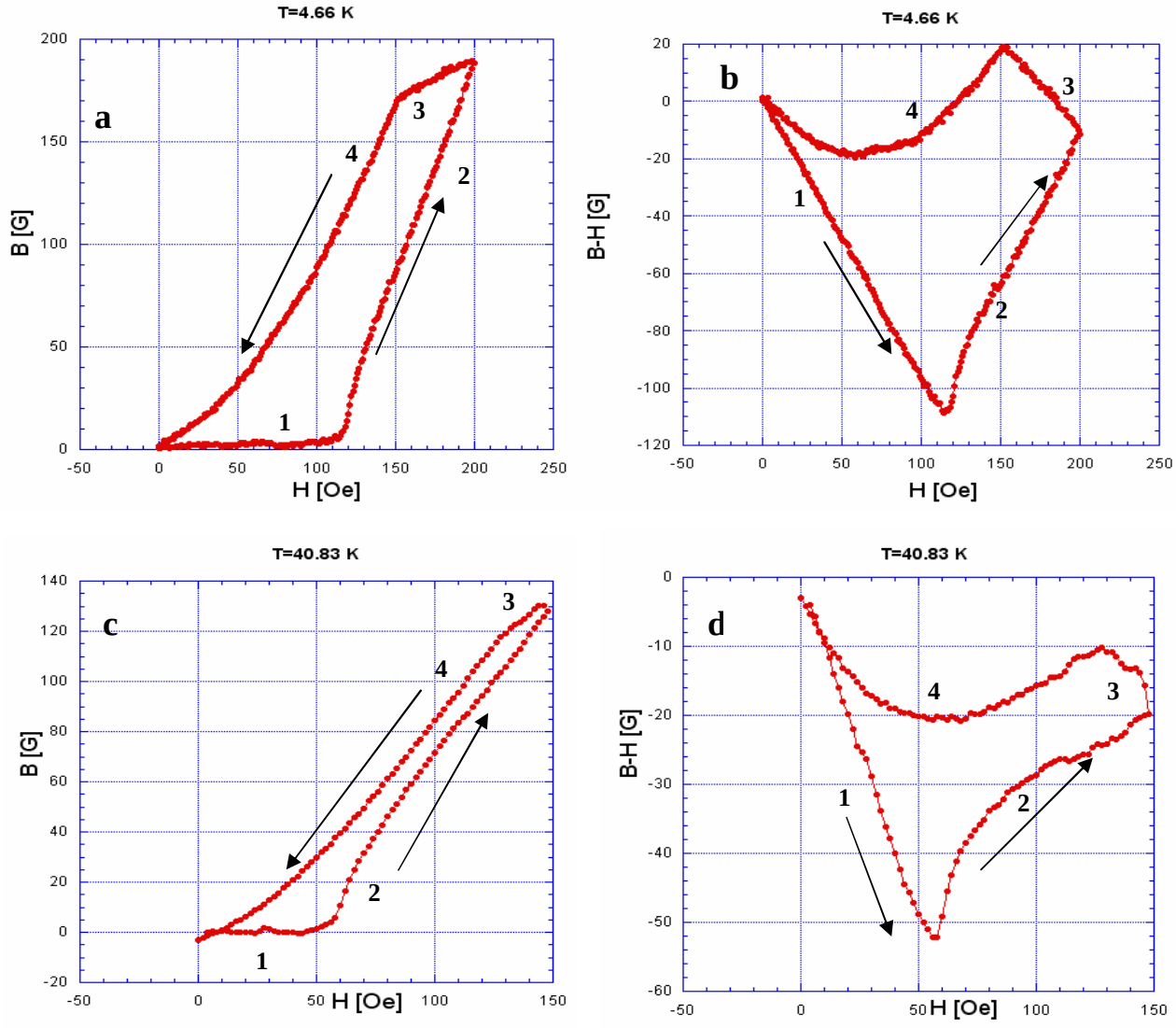

Fig. 4.46: Local magnetization loops showing the 4 steps of Bean model in (a),(b) $NbSe_2$ and (c),(d) $Bi_2Sr_2CaCu_2O_8$.

Summary

This work concentrated on examination of the enhancement and suppression mechanisms of the three main sources for hysteresis: geometrical barrier, B-L surface barrier, and pinning.

The theoretical model of geometrical barrier provided a very good description of the experimental vortex dome in section 4.1.1. From this agreement, H_{c1} of the sample was evaluated. The effect of dc in plane magnetic field on geometrical barrier was presented in DMO measurements using current modulation. DMO current modulation method was found to show more detailed picture than the conventional field modulation used before, and enabled measurements of vortex chains and vortex dome. The effect was shown to be the formation of vortex chains which connect vortex dome with the sample edges and contribute to flux exchange. The vortex chains are formed due to attraction of pancakes to Josephson vortices. Josephson vortices separation both in the in-plane and in the out of plane directions scales with the in-plane field. The in-plane separation was measured and fitted to theory, proving that indeed the Josephson vortices are seen in the measurements.

Two measurements of hysteresis suppression by in-plane field were presented- one is local magnetization hysteresis and the second is hysteresis in dome edge location. In both measurements the hysteresis suppression with H_x occurs in a similar manner, suggesting that vortex dome is the main source for magnetization hysteresis suppression by an in plane field in BSCCO at T=82 K and low H_z (up to 20 Oe). Moreover, within a single H_z scan, the H_z field at which vortex dome irreversibility is closed is the same field of sudden hysteresis suppression in magnetization hysteresis, providing extra evidence of the importance of the vortex dome mechanism in understanding the effect of an in plane field on hysteresis.

A theoretical calculation of comparison between vortex chains and vortex dome energies was performed showing that the attractive interaction between Josephson vortices and pancakes grows with H_x. As the attractive interaction is higher, the macroscopic energetic barrier for flux exit, coming from Meissner currents, is reduced and more vortices can exit. When the energetic barrier becomes microscopic, the hysteresis is suppressed completely due to thermal fluctuations. All the measurements, both local magnetization and vortex dome edges, agree that complete hysteresis suppression occurs at H_x=17 Oe.

A novel phenomenon is presented of phase transition between 2D vortex dome and 1D vortex chains. The equation for this transition is presented confirming that for low H_z inter-vortex elastic interaction is low and the attractive Josephson vortices energy is dominant making all pancakes arrange in 1D stripes along the Josephson vortices.

Studying interaction between vortices and periodic surface holes, we visualized matching effects and pristine melting. In transport measurements, we identified three regimes of current flow in the

region with surface holes. At low temperatures there is increased bulk pinning in the patterned region resulting from pinning of 3d stacks of coupled pancake vortices. At intermediate temperatures we see that the transport current flows at the edges of the patterned region, similar to sample edges current flow [70] that arises from the B-L surface barrier for vortex penetration into the sample. This suggests that the dominant mechanism here is edge pinning rather then bulk pinning, as a sequence of c-axis decoupling of pancakes weakening their pinning strength. The barrier in the edge of the patterned region is probably due to pinned vortices which repel vortices in the pristine region from the patterned region. It was shown that the transition line to this regime of edge flow in the patterned region coincides with both pristine and patterned regions melting lines.

At the highest temperatures we observed reduced bulk flow in the patterned region which is explained by reduced conducting material. The transition to this mode is the delocalization line where vortices unpin from the holes removing the penetration barrier and thus stopping the current flow through the edges. This regime behaves like a normal state with reduced conducting material due to surface holes.

This work also dealt with a novel system, whose aim is to measure magneto-optical diffraction peaks from vortices. The noise in the system was reduced and magnetic signal was improved, although not enough to observe Bragg peaks from superconducting samples. Noise source detection procedure showed that every optical component adds slightly to the noise, and it is multiplied due to coherence of the light to produce diffraction fringes which fluctuate. Thus, dealing with noise in coherent systems proved to be much more difficult than assumed.

We succeeded to measure the penetration and irreversibility field using the zero order peak in the diffraction pattern. We also observed hysteresis in local magnetization loop measurements that can be explained by the Bean critical model.

References

1. G. Bednorz *et al.,* Z. Phis. **B64**, 189 (1986).
2. G. Blatter *et al.,* Rev. Mod. Phys. **66**, 1125 (1994).
3. N. Avraham *et al.,* Nature **411**, 451 (2001).
4. M. Tinkham. “Introduction to Superconductivity” 2ed., McGraw-Hill, 1996.
5. A. Abrikisov, Sov. Phys. JETP **5**, 1174 (1957).
6. K. Harada *et al.,* Nature **360**, 51 (1992).
7. A. Crisan, S. Bending and T. Tamegai, Supercond. Technol. **21**, 015017 (2008).
8. A. Koshelev, Phys. Rev. B **68**, 094520 (2003).
9. J. Clem, Phys. Rev. B **43**, 7837 (1991).

10. L. Bulaevskii, Phys. Rev. B **46**, 366 (1992).
11. L. Burlachkov V. Geshkenbein, A. Koshelev, A. Larkin and V. Vinokur, Phys. Rev. B **50**, 16770 (1994).
12. A. E. Koshelev, Phys. Rev. Lett. **83**, 187 (1999).
13. T. Tamegai *et al.,* Supercond. Sci. Technol. **17,** s88 (2004).
14. D. Shaltiel *et al.,* Phys. Rev. B **77**, 214522 (2008).
15. M. Yasugaki *et al.,* Phys Rev. B **67**, 104504 (2003).
16. C. Bolle *et al.,* Phys. Rev. Lett. **66**, 112 (1991).
17. T. Tamegai, H. Chiku and M. Yokunaga., Physica C **445-448**, 201 (2006).
18. T. Tamegai *et al.,* Physica C **392-396,** 311 (2003).
19. T. Tamegai *et al.,* Physica C **468**, 531 (2008).
20. T. Matsuda *et al.,* Science **294,** 2136 (2001).
21. V. Vlasko-Vlasov, A. Koshelev, U. Welp, G. Crabtree and K. Kadowaki, Phys. Rev. B **66**, 014523 (2002).
22. B. Khaykovich *et al.,* Phys. Rev. B **56**, R517 (1997).
23. C. Bean and J. Livingston, Phys. Rev. Lett. **12**, 14 (1964).
24. M. Konczykowski, Phys. Rev. B **43**, 13707 (1991).
25. E. Zeldov *et al.,* Phys. Rev. Lett. **73,** 1428 (1994).
26. N. Morozov, E. Zeldov, D. Majer and B. Khaykovich, Phys. Rev. Lett **76,** 138 (1996).
27. N. Morozov, E. Zeldov, M. Konczykowski and R. Doyle, Physica C **291,** 113 (1997).
28. M. Benkraouda and J. Clem, Phys. Rev. B **53**, 5715 (1996).
29. M. Benkraouda and J. Clem, Phys. Rev. B **58**, 15103 (1998).
30. Th. Schuster, M. Indenbom, H. Kuhn, E. Brandt and M. Konczykowski, Phys. Rev. Lett. **73**, 1424 (1994).
31. E. Brandt, Phys. Rev. B **46**, 8628 (1992).
32. G. Mkrtchyan *et al.,* JETP **34**, 195 (1972).
33. C. Bean, Rev. Mod. Phys. **36**, 31 (1964).
34. A. Soibel *et al.,* Nature **406**, 282 (2000).
35. S. Goldberg *et al.,* Phys. Rev. B, to be published (2009).
36. S. Kasahara, Y. Tokunaga, N. Kameda, M. Tokunaga and T. Tamegai, Phys. Rev. B **71**, 224505 (2005).
37. M. Connolly, S. Bending, A. Grigorenko, T. Tamegai, Phys. Rev. B **72**, 224504 (2005).
38. O. Auslaender *et al.,* Nature Physics **5**, 35 (2009).
39. A. Grigorenko *et al.,* Nature (London) **414**, 728 (2001).

40. M. Tokunaga, T. Tamegai, Y. Fasano and F. de la Cruz, Phys. Rev. B **67**, 134501 (2003).
41. M. Yasugaki *et al*, Phys. Rev. B **65**, 212502 (2002).
42. T. Tamegai *et al.,* Physica C **460-462,** 791 (2007).
43. T. Tamegai, H. Chiku and M. Tokunaga, Physica C **463-465,** 245 (2007).
44. T. Tamegai, M. Matsui and M. Tokunaga, Physica C **412-414,** 391 (2004).
45. T. Tamegai *et al.,* Physica C **445-448,** 201 (2006).
46. T. Tamegai et *al.,* Physica C **392-396,** 311 (2003).
47. T. Tamegai *et al.,* Physica C **468,** 531 (2008).
48. T. Tamegai, H. Chiku, H.Aoki and M. Yokunag*a*, Physica C **437-438,** 314 (2006).
49. S. Bending *et al.,* Physica C **412-414**, 372 (2004).
50. U. Welp *et al.,* Nature (London) **376**, 44 (1995).
51. D. Larbalestier, A. Gurevich, M. Feldman and A. Polyanskii, Nature (London) **414**, 368 (2001).
52. D. Majer, E. Zeldov and M. Konczykowski, Phys. Rev. Lett. **75**, 1166 (1995).
53. T. Tamegai *et al.,* Physica C **412-414,** 391 (2004).
54. A. Larkin *et al.,* Zh. Eksp. Teor. Fiz. **61**, 1221 (1971).
55. R. Huebner *et al.,* J.Low Temp. Phys **6**, 275 (1972).
56. S. Banerjee *et al.,* Phys. Rev. Lett. **93**, 097002 (2004).
57. N. Avraham *et al.,* Phys. Rev. B **77**, 214525 (2008).
58. V. Moshchalkov *et al.,* Rev B **54**, 7385 (1996).
59. M. Baert, V. Metlushko, R. Jonckheere, V. Moshchalkov and Y. Bruynseraede, Phys. Rev. Lett. **74**, 3269 (1995).
60. D. R. Nelson. Phys. Rev. Lett. **60**, 1973 (1988).
61. A. Schilling *et al.,* Nature (London) **382**, 791 (1996).
62. E. Zeldov *et al.,* Nature **375**, 373 (1995).
63. I. Khaln and B. Ya. Shapiro. Physica C **207**, 359 (1995).
64. L. Radzihovsky. Phys. Rev. Lett. **391-396**, 4923 (1995).
65. L. Radzihovsky. Phys. Rev. Lett. **74**, 4923 (1995).
66. A. Lopatin and V. Vinokur, Phys. Rev. Lett. **92**, 067008 (2004).
67. S. Banerjee *et al.,* Phys. Rev. Lett. **90**, 087004 (2003).
68. J. Kierfeld and V. Vinokur, Phys. Rev. Lett. **94**, 077005 (2005).
69. A. Lopatin and V. Vinokur, Phys. Rev. Lett. **92**, 067008 (2004).
70. D. Fuchs *et al.,* Nature **391**, 373 (1998).
71. D. Fuchs *et al.,* Phys. Rev. Lett. **80**, 4971 (1998).

72. A. Soibel, PhD thesis 2001 “Visualization of vortex-lattice melting transition and transport current flow in BSCCO with differential magneto-optical technique”.
73. D. Fuchs *et al.*, Phys. Rev. B **55**, R6156 (1997).
74. Y. Wang *et al.*, Phys. Rev. B **71**, 132507 (2005).
75. S. Rycroft *et al.*, Phys. Rev. B **60,** R757 (1999).
76. T. Johansen *et al.*, Phys. Rev. B **54**, 16264 (1996).
77. R. J. Wijngaarden, H. Spoelder, R. Surdeanu and R. Griessen, Phys. Rev. B **54**, 6742 (1996).
78. R. Wijngaarden, K. Heeck, H. Spoelder, R. Surdeanu and R. Griessen, Physica C (Amsterdam) **295**, 177 (1998).
79. V. Vinokur *et al.*, Physica C **295**, 209 (1998).
80. J. Kierfeld and V. M. Vinokur, Phys. Rev. B **71**, 029901 (2005).
81. H. Beidenkopf *et al.*, Phys. Rev. Lett. **95,** 257004 (2005).
82. U. Yaron *et al.*, Nature **376**, 753 (1995).
83. T. Klein *et al.*, Nature **404**, 413 (2001).
84. R. Cubitt *et al.*, Nature (London) **365**, 407 (1993).
85. T. Natterman, Phys. Rev. Lett. **64**, 2454 (1990).
86. T. Giamarchi and P. Le Doussal, Phys. Rev. Lett. **72**, 1530 (1994).
87. T. Giamarchi and P. Le Doussal, Phys. Rev. B **52**, 1242 (1995).
88. P. Le Doussal and T. Giamarchi, Phys. Rev. B **57**, 11356 (1998).
89. L. Balents, C. Marchetti and L. Radzihovsky, Phys. Rev. B **57**, 7705 (1998).
90. P. Goa, H. Hauglin, A. Olsen, M. Baziljevich and T. Johansen, Rev. Sci. Instrum. **50**, 141 (2003).
91. M. Terao, Y. Tokunaga, M. Tokunaga and T. Tamegai, Physica C **426–431**, 94 (2005).
92. G. Carneiro and E. H. Brandt, Phys. Rev. B **61**, 6370 (2001).
93. E. Brandt, Phys. Rev. Lett. **78**, 2208 (1997).